UNIVERSITY OF SOUTHAMPTON

FACULTY OF ENGINEERING AND THE ENVIRONMENT

Aerostat for Electric Power Generation

By

Stefano Redi

Thesis for the degree of Doctor of Philosophy

July 2011

UNIVERSITY OF SOUTHAMPTON

Faculty of Engineering and the Environment

Doctor of Philosophy

Aerostat for Electric Power Generation

By Stefano Redi

ABSTRACT

The exploitation of renewable energy sources is currently at the top of the agenda of many governments that are required to face the problem of the rising energy demand. In particular photovoltaics is considered one of the most promising technologies to meet the energy needs in the long term. However the effective exploitation of this source has always been hindered in many northern countries (like the UK) due to the weather conditions which are detrimental for the efficiency of photovoltaic generators.

As a possible solution to this problem, this research presents the preliminary concept evaluation of an innovative power generator based on photovoltaic and lighter than air technologies (Aerostat for Electric Power Generation – AEPG). The generator consists of a helium filled platform tethered to the ground that would be used to locate a photovoltaic array at high altitude, ideally above the cloud coverage, in order to reduce the negative effect of the atmosphere and optimize the power production. The power produced at high altitude would then be transmitted to the ground via the mooring tether.

First of all, the potential of this technology is evaluated in terms of the solar energy that can be collected at high altitude. The results obtained demonstrate that a generator located at an altitude between 6 km and 12 km could collect between 3.3 and 4.9 times the solar radiation that would fall on a ground based photovoltaic array. Furthermore the environmental conditions in which the system is due to operate are evaluated, employing standard atmospheric models and experimental wind speed datasets.

An overview of the main parameters involved in the design is then provided and general considerations are discussed in order to narrow the range of values these different parameters can take. A simplified mathematical model is introduced to assess the performance of the system in steady state conditions and a set of design parameters is chosen to define a baseline configuration for the concept design. Moreover, a transient 3D analysis of the whole system is performed in order to check if the dynamic behaviour can constitute a show stopper.

Finally the concept design of the AEPG is addressed and the most critical technical issues are identified. The location of the different subsystems is briefly discussed and a possible solution for the system layout is proposed. The study is completed with an initial sizing of the main components (structural in particular) in order to evaluate the different mass contributions and provide a preliminary assessment of the technical feasibility of the AEPG.

A Mia Nonna e Mia Zia

TABLE OF CONTENTS

DECLARATION OF AUTHORSHIP

I, Stefano Redi

declare that the thesis entitled

Aerostat for Electric Power Generation

and the work presented in the thesis are both my own, and have been generated by me as the result of my own original research. I confirm that:

- this work was done wholly or mainly while in candidature for a research degree at this University;
- where any part of this thesis has previously been submitted for a degree or any other qualification at this University or any other institution, this has been clearly stated;
- where I have consulted the published work of others, this is always clearly attributed;
- where I have quoted from the work of others, the source is always given. With the exception of such quotations, this thesis is entirely my own work;
- I have acknowledged all main sources of help;
- where the thesis is based on work done by myself jointly with others, I have made clear exactly what was done by others and what I have contributed myself;
- parts of this work have been published as:

Journal Papers

Redi S., Aglietti G.S., Tatnall A.R., Markvart T., 2011. Dynamic Response to Turbulence of Tethered Lighter than Air Platforms. AIAA Journal of Aircraft. 48(2), 540-552.

Redi S., Aglietti G.S., Tatnall A.R., Markvart T., 2010. An Evaluation of a High Altitude Solar Radiation Platform. ASME Journal of Solar Engineering. 132(1), 1-8.

Aglietti G.S., Redi S., Tatnall A.R., Markvart T., 2009. Harnessing High Altitude Solar Power. IEEE Transactions on Energy Conversion. 24, 442-451.

Aglietti G.S., Redi S., Tatnall A.R., Markvart T., 2008. High Altitude Electrical Power Generation. WSEAS Transactions on Environment and Development. 4, 1067-1077.

Conference papers

Redi S., Aglietti G.S., Tatnall A.R., Markvart T., 2010. Preliminary design of lighter-than-air solar collectors. Proceedings of the 8th International Airship Convention, Bedford, United Kingdom, 29 Sep-3 Oct 2010.

Redi S., Aglietti G.S., Tatnall A.R., Markvart T., 2009. Configuration Study of High Altitude Solar Collectors. Proceedings of the IEEE Electrical Power and Energy Conference, Montreal, Canada, 22-23 Oct 2009.

Redi S., Aglietti G.S., Tatnall A.R., Markvart T., 2009. Collection of Solar Energy at High Altitude. Proceedings of the 24th European Photovoltaic Solar Energy Conference and Exhibition, Hamburg, Germany, 20-25 Sep 2009.

Aglietti, G.S., Redi, S., Tatnall, A.R. and Markvart, T., 2008. Exploitation of High Altitude Solar Energy. Proceedings of the 2nd WSEAS/IASME International Conference on Renewable Energy Sources (RES '08), Corfu, Greece, 26-28 Oct 2008.

Book chapters

Aglietti, G.S., Redi, S., Tatnall, A.R., Markvart, T. and S.J.I. Walker, 2010. Aerostat for Solar Power Generation. In R.D. Radescu (Ed.), Solar Energy (pp. 399-413). Published by Intech.

Signed: 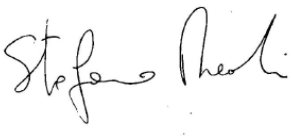

Date: 23/02/2012

ACKNOWLEDGEMENTS

I would like to express my gratitude to all the people who have been supporting me during this journey.

First of all I would like to thank my supervisor Professor Guglielmo Aglietti for his precious time and help. His enthusiasm and dedication to work have set an example to follow during these years and in my future life. Moreover I would like to thank Dr. Adrien Tatnall for his advice and Professor Thomas Markvart for introducing me to photovoltaics.

I am also grateful to my fellow graduate students in the Astro group who have shared this experience with me and to all my friends, the new ones I've made here in Southampton as well as the ones in Italy who have always sent me their support.

Finally I would like to thank my family and Elisa for their constant love during these years, despite the distance separating us.

1 INTRODUCTION

1.1 Social and Economic Background

Electricity demand and supply is one of the crucial issues that our society is facing at the moment. At the same time environmental concerns are also becoming more and more important and they are strongly influencing policy makers' decisions related to energy generation and consumption. In most of the developed countries like EU countries and US as well as in some of the fastest growing economies like China and India, green energy is at the top of the government agenda. In particular renewable energy sources are playing a fundamental role as they seem to represent the only suitable solution in the long term. Focusing on European data, the total year electricity generation was around 3,362 TWh in 2007, 15.6% of which came from renewable energy sources (Figure 1) [1] and the renewable share of new power installations (Figure 2) was 62% in 2009 [2] (37% wind, 21% photovoltaic systems, 2.1% biomass, 1.4% hydro, 0.4% concentrated solar power). Furthermore, although official data have not been published yet, the target for renewable in 2010 was 21% [1] of the total electricity generation.

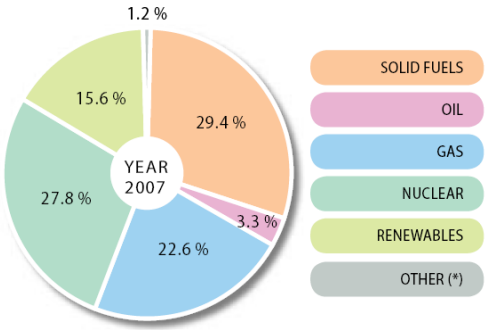

Figure 1 : Energy Sources (2007) [1]

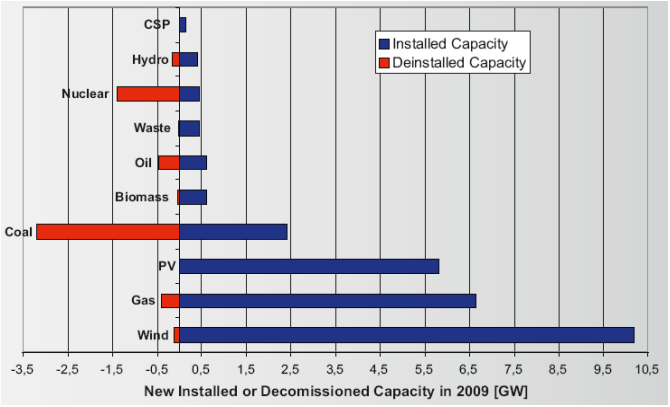

Figure 2 : New Installed or Decommissioned Capacity in 2009 [2]

This positive trend demonstrates that these sources, which include hydro, wind, biomass, geothermal and solar have a strong potential for meeting future energy needs, despite several problems related to the intermittency of these power sources, which has always constituted a key obstacle for their large scale use. At present the highest contributions come from hydro, wind and biomass while solar and geothermal still represent a smaller component of the total energy budget. However considering the fact that the energy provided by the Sun to the Earth in one hour is roughly equal to the world energy consumption of one year [3], it is easy to see why this source is considered extremely attractive and promising. Moreover solar energy usually requires relatively simple and low cost infrastructures to be harvested, if compared to other renewable sources like hydro and wind. In particular solar photovoltaic can be installed basically everywhere, from open fields to commercial and residential roofs. Present technologies can already provide acceptable efficiencies for a period of at least 25 years, which can offer a reliable solution, independent from electricity interruption from grid and from variations in electricity prices. These reasons explain the growth of this sector in the last few years and the effort of academia, research institutes and industry around the world to develop new materials and technologies.

New investments in solar power were about 33.5 billion US dollars in 2008 (just after wind) [4] while for what concerns the recent market growth, the PV status report 2010 compiled by the Joint Research Centre of the European commission [5] states that the global solar cells production increased more than 30 fold from 2000 to 2009, with an annular growth between 40% and 80%. From 2008 and 2009 the production increased of about 56% reaching a value of around 11.5 GW (Figure 3) with estimate of 36 GW for the end of 2010 [5]-[7].

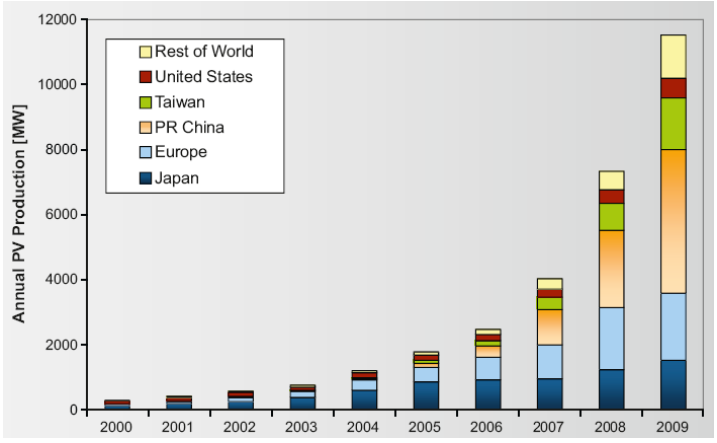

Figure 3 : Annual PV Production [5]

At present the European Union is ranked first in the list of cumulative installed capacity with 16 GW, representing about the 70% of the total world generation capacity [5]. It must be noted, though, that the diffusion of this renewable source greatly varies from country to country (Figure 4). Germany is still leading with a cumulative installed power of about 9.8 GW in 2009. This incredible result is mainly due to the German energy policy and the strong support programme of the government for the photovoltaic technology which enhanced the development of an industry sector that is now leader in the world.

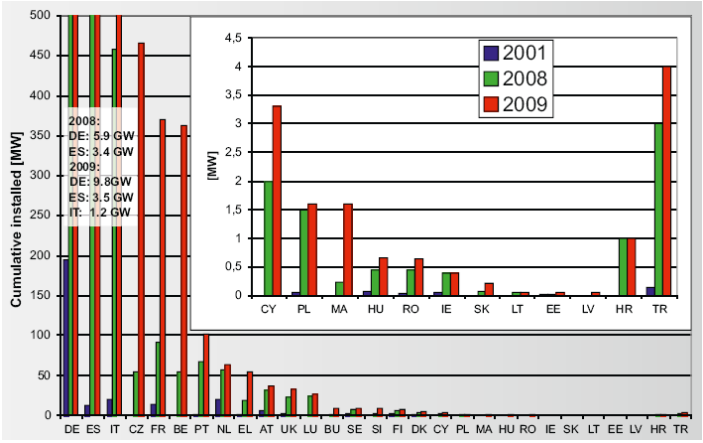

Figure 4 : Cumulative Installed PV Power [5]

1.2 Problems Related to Solar Resource Availability

Even though Germany is still ranked first in the list of European countries for solar power installations, the two most promising countries in Europe for the present and future exploitation of solar power are considered Spain and Italy which in 2009 had a cumulative installed power of 3.5 GW and 1.2 GW respectively [5]. The reason is quite intuitive and it is related to the climate conditions of these countries that make this renewable resource easily available for ground based photovoltaic system.

In fact local atmospheric conditions constitute an important issue when considering the possible implementation of a photovoltaic power system. Cloud coverage in particular can significantly reduce the amount of solar radiation reaching the ground surface, limiting the power output that the solar cells can provide. Therefore the diffusion of this kind of technology has always been hindered in countries at northern latitudes, like for example the UK, where the occurrence of cloudy sky conditions is more frequent than in other locations like southern Europe and northern Africa. As an example for the location of Aberdeen the daily solar irradiation (annual mean) on a horizontal surface is around 2.4 kWh/m^2, while for Almeria in the South of Spain the same figure can be as

high as 4.6 kWh/m^2 [8] (Figure 5). It is not difficult to understand why projects like Masdar [9], the fully sustainable city are being planned in the United Arab Emirates, and the energy will be provided mainly by harvesting the power of the sun.

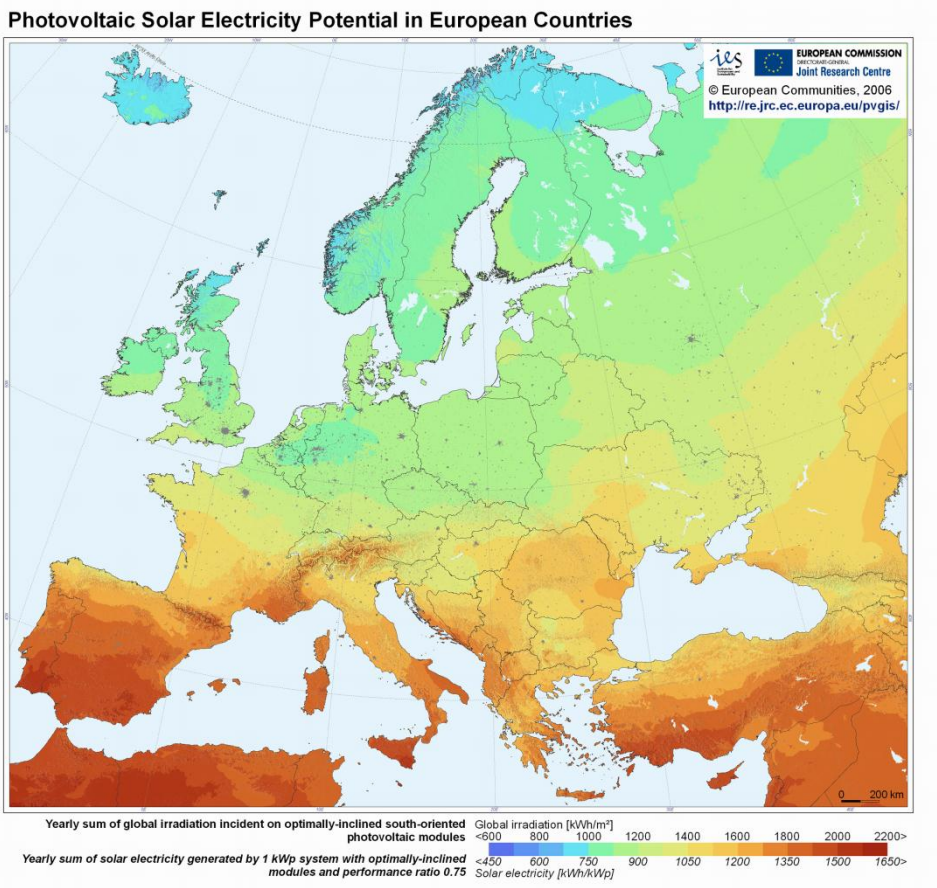

Figure 5 : Solar Irradiation Maps [8]

1.3 Proposed Solutions

Different ideas have been considered to overcome the problems related to the availability of the solar resource and to provide a solution for the global energy needs. The two projects that have aroused most interest in the past few decades have two opposite approaches to harvest the solar power where this is more widely available. The first approach has been proposed by the Desertec Foundation [10], based on the idea that the solar radiation can be collected mainly on the desertic area of northern Africa, converted into electrical power using concentrated solar power technology and then transmitted through a system of high voltage direct current (HVDC) lines to the different regions of Europe, Africa and the Middle East. However, even for these locations, the main part of the solar radiation attenuation is due to the presence of an

aerosols layer concentrated in the first few kilometres above the ground which considerably affects the solar intensity.

The second solution introduced by Glaser [11] in the 1970s consists of a very large photovoltaic array orbiting around the Earth that would be able to collect a constant value of solar radiation 24 hours a day without any attenuation due to the presence of the earth atmosphere. The power generated in orbit by this Solar Power Satellite (SPS), would then be transmitted to dedicated ground stations (rectennas) using electromagnetic waves and converted back into electricity. This solution has been reconsidered more recently [12,13], and studies are still ongoing in US, Europe [14,15] and Japan [16]. Moreover the American companies PowerSat [17], Solaren [18] and Space Energy [19] founded in the last few years are focusing their activity on the development of a demonstrator which would constitute an important milestone in the advancement of this technology.

Both solutions (Desertec and SPS) are currently being developed, and the different teams involved seem very confident of achieving significant successes in the short-medium term. However both solutions presented also involve significant economical and political issues that have always been a limit for the development and implementation of these concepts. On one hand the Desertec project raises concerns about possible threats to the reliability of the system due to the presence of countries which can be politically unstable. On the other hand the SPS solution also gives rise to safety concerns related to the transmission of the power to the ground which are difficult to evaluate and address.

1.4 Objectives and Contribution of this Work

The present study investigates the possibility of implementing an alternative system to Deserted and SPS which would specifically address the issues related to the cloud coverage in order to provide a suitable solution for the optimization of the power output of a photovoltaic array regardless the weather conditions. This innovative concept consists of a lighter than air (LTA) platform tethered to the ground which would be used as a support for the photovoltaic cells at high altitude, ideally above the cloud layer. Aglietti and al. have already introduced the concept in [20] and [21] identifying the main features of the system which would be constituted by a helium filled balloon partially covered with photovoltaic cells that collect the solar radiation available at

operational altitude and convert it into electricity (Aerostat for Electric Power Generation – AEPG). Figure 6 shows a representation of the AEPG concept.
The electrical power produced above the clouds is then transmitted to the ground via the mooring tether which is also designed to withstand the environmental conditions (mainly wind speed and gusts).
In order to optimise the production of electric power, the angle of incidence between the PV cells surface and the solar beam needs to be minimised. This is achieved by mounting the solar cells on an external stepped structure attached to the balloon envelope. This structure allows all the cells to be pointing towards the same direction. Moreover the system needs to be able to track the sun position. The pointing of the PV array is performed using a gimballed system constituted by a set of electric motors, which can provide rotations about two different axes (elevation and azimuth). In particular the motors that provide the elevation rotation are located along the equator while the motor responsible for the azimuth rotation is located at the confluence point of the two harness cables. The lower part of the tether is stabilised using an aerodynamic profile which would align itself with the wind direction. An alternative method for the azimuth rotation would employ a fan located on the back of the balloon to be operated in low wind conditions.

Figure 6 : Aerostat for Electric Power Generation

The AEPG solution can constitute a compromise between the traditional ground based PV plants and the concept proposed by Glaser, since the reduced amount of clouds and more in general of air mass above the collector can provide a significant advantage in terms of solar energy collected. On the other hand the costs for the development of the concept can be orders of magnitude lower, and the safety and regulatory issues involved are expected more straightforward to address since they are common to other similar

systems currently in operation. Moreover the possibility of generating power close to where that power is needed, has always been presented as one of the main advantages of solar photovoltaic and the AEPG reduces the use of complex infrastructures as in the case of Desertec or SPS.

The work described in this thesis has the primary objective of performing a preliminary assessment of the technical feasibility of the AEPG in order to identify possible showstoppers that could deny the viability of the concept. More specifically the contribution of this work to the current state of the art has been focused on the following activities:

- Development of a model for the determination of the solar radiation that can be collected by the platform as a function of the operational altitude. Determination of the potential advantage of the AEPG in terms of collected energy compared to a ground based photovoltaic system [22].
- Preliminary considerations about the main parameters involved in the design and first sizing of the system [23]-[25].
- Development of a steady state model for the determination of the final system configuration when subjected to a mean wind profile above the ground. Skimming of possible technical solutions based on the result obtained [26]-[28].
- Development of a dynamic model for the determination of the system behaviour when subjected to realistic operational conditions i.e. in the presence of atmospheric turbulence [29].
- Concept design of the system, identification and sizing of the main subsystems [22]-[29].

1.5 Thesis Layout

Due to the multidisciplinary nature of this work, each chapter of the thesis is introduced with some considerations about the state of the art of the topic discussed therein, rather than including a single literature review at the very beginning, as is more common practice in PhD theses.

The overall structure of the thesis is organised in 9 chapters which are here briefly outlined. Following on from this introduction, chapter 2 is focused on the development of a simplified model for the determination of the solar radiation that can be expected at different altitudes above the ground. The results are employed to determine the potential

advantage, in terms of solar radiation collected, that the AEPG could provide if located at a defined height. Chapter 3 evaluates the atmospheric environment in which the system is due to operate. The main characteristics included in the analysis are derived from the standard atmosphere (temperature, density and pressure), from experimental data (mean wind speed) and theoretical models (gusts and turbulence). After the introduction of the state of the art of lighter than air systems presented in chapter 4, some preliminary considerations about the most important parameters involved in the design of the AEPG are presented in chapter 5. These parameters include the disposable lift as well as the characteristics of the main subsystems, i.e. the photovoltaic generator and the power transmission components. The final aim of this preliminary analysis is to assess the ranges in which these parameters can vary. Chapter 6 presents a steady state model of the tethered aerostat which is employed to evaluate the final position of the system in equilibrium conditions. The results obtained for a set of specific configurations are used to define a baseline for the dynamic analysis performed in chapter 7, which evaluates the behaviour of the system when subjected to unsteady atmospheric conditions (gusts and turbulence). Moreover the baseline is considered as the starting point for the concept design addressed in chapter 8. The concept design of the AEPG includes the preliminary sizing of the structural components and the main subsystems involved in the design, together with additional considerations about the mass breakdown and the balance of the system.
Finally conclusions are inferred in chapter 9, also highlighting possible areas of further work.

2 HIGH ALTITUDE SOLAR IRRADIATION

As a first step in the study of the technical feasibility of a high altitude platform which is supposed to exploit the solar energy as its primary source, it is important to include the evaluation of the sun radiation that can be harvested by the power subsystem [30]-[34]. Similarly in the case of the study of the technical feasibility of a high altitude solar collector, the research requires a preliminary assessment of the potential of this technology. This assessment is carried out by evaluating the possible advantage in terms of solar radiation collected that this kind of system could bring compared to the traditional ground based photovoltaic systems (PV) [22]. The advantage mainly derives from the reduced attenuation of the solar radiation as it travels through the atmosphere, especially if clouds are present above the location considered. In addition to that the effect of the cloud layer below the flying collector which reflects the incoming solar radiation might give a significant contribution to the total energy budget.

First of all a sun beam travelling through clear atmosphere is considered using an existent model to calculate the daily irradiation at different altitudes in clear sky conditions. The results obtained are then integrated with experimental data describing clouds distributions versus altitude, and finally the contribution of the diffused radiation is also included to give a realistic evaluation of the total actual irradiation at a specific altitude. Furthermore particular considerations are inferred about the role that the reflected radiation might have when the flying collector is located above a cloud layer. The results are obtained for a specific location in the UK, where the experimental data have been acquired for altitudes up to 12 km. The general conclusions, however, involving the potential of high altitude solar collectors, can be extended to other countries in Europe with similar climates.

The value of the solar power reaching the top of the atmosphere is influenced by the Earth-Sun distance which varies during the year, due to the Earth orbit's elliptical shape. When the mean value of the distance is considered, the power value at the top of the atmosphere is called solar constant which is equal to [35]:

$$C_S = 1366.1 \pm 0.58 \ W/m^2 \tag{2.1}$$

Considering the values of daily solar irradiation (annual mean) presented at page 6, the energy that can be collected in Aberdeen is equal to a 1.75 hours exposure to the solar constant, while the same figure for Almeria would be 3.37 hours.

Solar power is distributed over a wide spectrum as presented in Figure 7 which is comparable with the one obtained from a black body at 5778 K, assumed as the effective temperature of the sun [36]. It is estimated that 99% of the solar power is comprised in the wavelength interval between 280 nm and 4960 nm, while the maximum of the monochromatic irradiance can be found at 480 nm [37]. UV radiation, i.e. below 400 nm counts as the 8.73% of the total solar power, while visible light (between 400 nm and 700 nm) and infrared (above 700 nm) represent the 38.15% and 53.12% of the spectrum respectively.

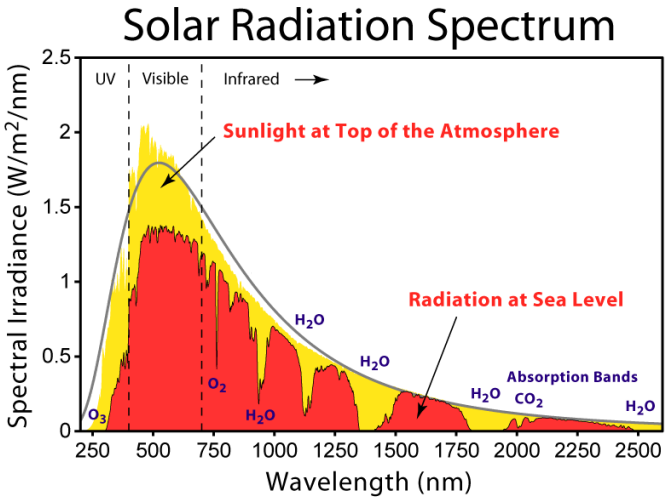

Figure 7 : Solar Spectrum (available at [38])

As the solar radiation beam travels through the atmosphere, it is influenced by two main processes. The first process is called *scattering* and it consists of a deflection of the radiation wave components which interfere with different particles in the atmosphere. This deflection can involve either atmospheric gas molecules or larger particles in the atmosphere such as aerosols, water, dust or pollution. In the first case the phenomenon is referred to as Rayleigh scattering which is responsible for the blue colour of the sky while the deflection caused by larger particles is defined as Mie scattering.

Solar radiation is also affected by another process defined as molecular *absorption*, in which the energy of the photons is converted into thermal energy. Molecular absorption usually depends on the atmospheric gas compositions which have different effect as different wavelengths are considered. For example the ozone layer in the stratosphere absorbs almost completely the UV radiation with wavelengths below 290 nm while water vapour absorbs wavelengths components above 2500 nm.

As a result of the two processes presented, the total radiation falling on a surface can be divided into two main components: direct (or beam) and diffuse. The contribution of the

latter becomes significant as lower atmospheric layers are considered and it can therefore be quite high on the ground, especially under a cloudy sky. Most importantly, the processes mentioned above result in a decrease of the solar radiation intensity as it travels from the top of the atmosphere to the ground. The total attenuation is called extinction [39] and, in the case of the Earth's atmosphere, is mostly due to scattering. The extent of radiation scattering and absorption strongly depends on the path length of the sun beam from space to ground and on the atmospheric characteristics encountered. It is, therefore, extremely important to define the path length as a function of the time of the day and the atmospheric properties at various altitudes, in order to obtain an estimate of the radiation that takes into account the influence of the actual atmospheric composition (including the possible presence of clouds). The characteristics of the clear atmosphere at different heights have been investigated in depth by other authors, and existing publications can constitute a good starting point for clear atmosphere calculations [40]-[42]. Moreover several broadband models have been developed to evaluate the radiation falling on a surface in clear sky conditions [43,44], and in particular different spectral models have been embedded in software for clear sky irradiance calculations such as SMARTS [45], becoming de facto widely used tools in the PV industry. These models are powerful and sufficiently accurate when a clear sky is considered, the condition in which the output of a ground based PV system reaches its maximum. For the present purpose, these models can be effectively used when performing calculations in clear sky conditions. However the final results need to take into account the presence of clouds and their effect on solar radiation.

Recent investigations consider the cloud effect on clear sky models [46-48] and they can provide useful information but only in the case of ground based PV systems. Some exceptions, in which the vertical distribution of the cloud is considered, can be found in literature [49,50] but unfortunately the studies are not detailed enough for the purpose of this work. Finally some existing models, such as MODTRAN [51] and libRadtran [52] can include the effect of weather conditions if some information about the cloud structure is provided as input. However these sophisticated models are oriented more towards atmospheric physics studies rather than engineering applications.

Since the aim is a first assessment of the improvement obtained by locating a solar collector at high altitude, the analysis must take into account the presence of the clouds, and at the same time, it must satisfy the simplicity that a preliminary engineering study requires. Similar methods have been proposed [31,33] to estimate the energy that could

be used to power the various subsystems of a flying vehicle. Even though the results presented can't be directly used to estimate the potential advantage of the AEPG, these methods can be adapted to the particular application considered in this study.
In this context, the following analysis estimates the solar radiation that can reach a surface as a function of its altitude, using cloud properties profiles that have been obtained through recent measurements acquired by radar/lidar systems [53] at a station located in the South of the UK. The use of these measurements [54] provides the extinction parameter profile, which relates the attenuation of the solar radiation to its path through the atmosphere.

2.1 Background Theory

The general case of a beam of light travelling through the Earth's atmosphere is considered. In order to define the loss of intensity (*atmospheric extinction*) that the beam experiences as it goes through a gas volume of length Δz, the *Lambert-Beers' attenuation law* [39] is used:

$$I = I_0 \exp(-\alpha \cdot \Delta z) \tag{2.2}$$

having defined the extinction parameter α [m^{-1}] of the gas volume and the intensity (*irradiance*) I_0 [W/m^2] of the beam entering the volume.

Dividing the path length from the top of atmosphere to the ground in segments of constant extinction α_i and length Δz_i, Eq (2.2) can be rewritten to estimate the intensity of the beam that reaches the ground as:

$$I = I_{TOP} \exp\left(\sum (-\alpha_i \cdot \Delta z_i) \right) \tag{2.3}$$

The sum considers all the layers of the atmosphere (each with different extinction parameters α_i) crossed by the beam. In reality the value of the extinction parameter can depend on the different wavelengths composing the beam of light. Therefore the attenuation will be different for the various wavelengths, as they interfere with different components of the atmosphere. However this effect is not taken into account for the moment, since the study presented in this chapter is preliminary, and this degree of detail goes beyond the purposes of the work. Moreover, since the sum in Eq. (2.3) should take into account all the intervals in which α_i is significant, the maximum height above the ground generally considered for practical purpose is 50 km [40-42],

beyond which the extinction parameter becomes effectively negligible, and the intensity of the radiation (I_{TOP}) is assumed equal to the solar constant given by Eq. 2.1.

To evaluate the path length in the case of the Earth atmosphere, the *relative air mass* has to be included, which defines the path length relative to that at the zenith [55,56] (Figure 8).

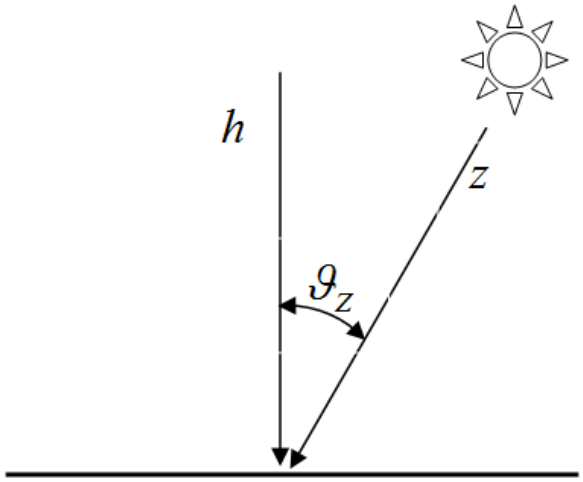

Figure 8 : Relative airmass as a function of the solar Zenith Angle

The relative air mass, $AM_{REL}(\vartheta_Z)$ for small solar Zenith angles ϑ_Z , can be approximated with the formula [56]:

$$AM_{REL}(\vartheta_Z) = \frac{1}{\cos(\vartheta_Z)}, \tag{2.4}$$

while for larger values of ϑ_Z , the relation developed in [57] has to be applied:

$$AM_{REL}(\vartheta_Z) = \frac{1.002432\cos(\vartheta_Z)^2 + 0.148386\cos(\vartheta_Z) + 0.0096467}{\cos(\vartheta_Z)^3 + 0.149864\cos(\vartheta_Z)^2 + 0.0102963\cos(\vartheta_Z) + 0.000303978} \tag{2.5}$$

The solar zenith angle can be computed, from the time (day of the year and hour of the day) and the location (latitude and longitude) as described in [58].

Starting from the path evaluated along the vertical Δh, the real path length Δz can be calculated as:

$$\Delta z = AM_{REL}(\vartheta_Z) \cdot \Delta h . \tag{2.6}$$

The intensity depends on the solar zenith angle considered, and Eq.2.3 can be rewritten as:

$$I(\vartheta_Z) = I_{TOP} \exp\left(- AM_{REL}(\vartheta_Z) \cdot \sum(\alpha_i \cdot \Delta h_i) \right) \tag{2.7}$$

The equation can be simplified considering the integrated extinction α^{INT} :

$$\alpha^{INT} = \sum(\alpha_i \cdot \Delta h_i), \tag{2.8}$$

that corresponds to the extinction due to the entire air mass present along the vertical path. Eq 2.7 therefore becomes:

$$I(\vartheta_Z) = I_{TOP} \exp\left(-AM_{REL}(\vartheta_Z) \cdot \alpha^{INT}\right) \tag{2.9}$$

2.2 Irradiance in Clear Atmosphere

The data concerning the clouds distribution used in this study, cover altitudes up to 12km. It is quite rare to find clouds above an altitude of 12 km (although there are some exceptions their impact on the yearly irradiation is minimal), and therefore the atmosphere above that height is considered clear [59]. The first step is therefore to estimate the irradiance in clear sky as a function of the altitude (and in particular at 12 km), and then include the effects of the clouds below that height.

At present, different radiative models are available which, given a set of input parameters, can provide an estimate of the solar irradiance that can be expected for a specified location on Earth. In particular some of these models have been embedded in software which can constitute an extremely useful tool for researchers and PV designers to assess the availability of solar radiation for a particular site. For the present analysis the model SMARTS [45], hosted by the National Renewable Energy Laboratory, is chosen to evaluate the irradiance at 12 km in clear sky conditions.

Since the experimental data used in this study are acquired by the Chilbolton Observatory (51.1445 N, 1.4370 W), in the South of the UK, this location is given as input to the model. Furthermore other significant input parameters chosen include the Shettle and Fenn Aerosols Model [60] for a rural environment, and the value for the Aerosol Optical Depth (AOD referred to a wavelength of 500 nm) set at 0.084 [61] at ground level. The AOD quantifies the degree to which aerosols prevent the transmission of light by absorption or scattering of light. It must be noticed that the value of AOD chosen, would apply only to reference spectra used for comparison of different technologies. In real conditions this ground value can be highly variable for the location of Chilbolton Observatory, ranging from 0.05 to 0.4 depending on climatology [62]. As far as the precipitable water (PW) value is concerned, this is derived from the standard atmosphere embedded in the software and set to a mean value of about 1.5 cm on the ground. The total precipitable water is the amount of water that can be obtained from

the surface to the "top" of the atmosphere if all of the water and water vapor were condensed to a liquid phase.

The altitude above the ground also has a significant effect on the variation of both AOD and PW, since these two components are generally concentrated in the lower layers of the atmosphere. This effect is taken into account in the aerosol model and in the reference atmosphere included in SMARTS as higher layers of the atmosphere are considered for calculations.

The calculations are performed for each month of the year considering a sun tracking surface and they include, for the moment, only the beam (direct) contribution of the solar radiation. As an example, the results obtained for the month of March, at 12km, 6 km and on the ground, in clear sky conditions relative to the location of Chilbolton Observatory are presented in Figure 9. The irradiance profiles obtained for the different months are used in the following section as a starting point for the calculations in actual atmosphere, performed with the use of experimental data.

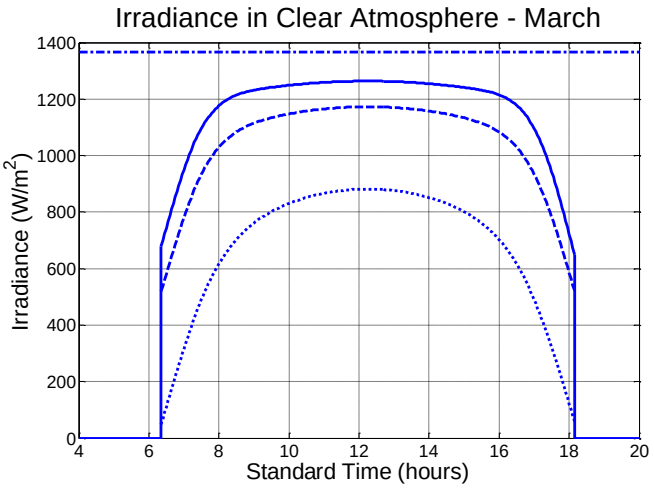

Figure 9 : Irradiance in Clear Atmosphere calculated from SMARTS (12 km solid line, 6 km dashed line, ground dotted line, solar constant dash-dotted line), location 51.1 N, 1.4 W, March.

2.3 Irradiance in Actual Atmosphere

Using the irradiance in a clear atmosphere as obtained in the previous section, the irradiance at different altitudes in realistic atmosphere conditions including clouds is evaluated. Clouds are defined in terms of the cloud base height so low clouds occur below 2000m, middle clouds are between 2000 and 6000m and high clouds are above 6000m. The data used for the calculations are relative to a specific location in the UK for a particular period of observations and considerations about the obtained results should take into account this limitation.

2.3.1 Beam (Direct) Irradiance Evaluation

The extinction coefficient at different altitudes is estimated in actual atmosphere conditions. The dataset used is provided by Cloudnet [53], which acquires Radar/Lidar measurements at different locations in Europe, to estimate cloud properties. Analogous measurements can be provided by the Atmospheric Radiation Measurement (ARM) Program [63], which analyses the atmospheric properties above several sites, mainly in the US, in order to support the studies related to the global climate change. The data are free to use for non-commercial research purposes. In particular the dataset used, contains the extinction parameters calculated from the measurements acquired at Chilbolton Observatory (51.1445 N, 1.4370 W) [54] in the height range between 0 and 12 km. The observations were performed almost every day of the year (from April 2003 to September 2004), 24 hours a day. Figure 10 shows, as an example, the measurements acquired in one day.

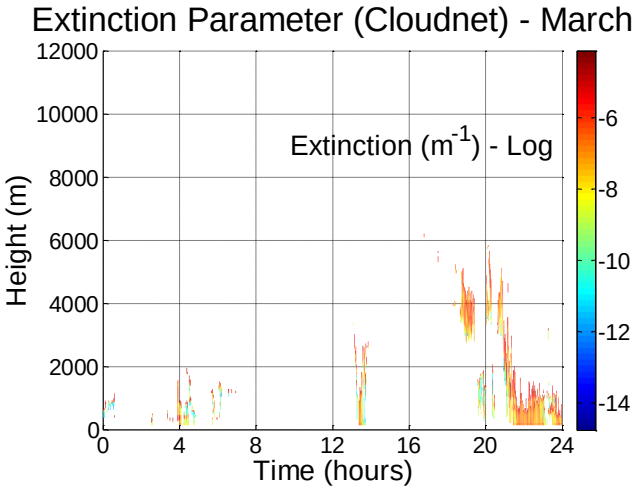

Figure 10 : Extinction Parameter (log) samples covering one day data - Chilbolton Observatory

The Cloudnet dataset is integrated with a vertical profile of extinction parameters for clear sky conditions. These values can be found in [42], where the vertical profile of the extinction parameters is defined, due to Rayleigh and aerosols attenuation for the different wavelengths (270-4000 nm) in the solar spectrum, in the height range between 0 and 50 km. However for this preliminary calculation, only the extinction parameters related to the spectrum of the visible light (360-830 nm) are taken into account. This choice is due to the fact that UV radiation is mainly attenuated by atmospheric layers in the stratosphere above 12 km [64] (where SMARTS is used for calculations) and that in addition the atmospheric attenuation becomes less important at longer wavelengths. For example the extinction coefficient at 6 km decreases from $8.04 \cdot 10^{-3}$ km^{-1} at 600 nm to

$3.54 \cdot 10^{-3}$ km^{-1} at 900 nm and $1.93 \cdot 10^{-4}$ km^{-1} at 2170 nm. This assumption is therefore expected to be conservative for later calculations. The values found in the dataset are averaged for each layer of the atmosphere, leading to the determination of the extinction profile in clear atmosphere conditions (α_i^{Clear}).

It must be noticed, as a caveat, that the conditions considered in [42] are ideal and they would not be applicable to real cases in general for more accurate calculations. In particular the choice of the aerosols optical depth (AOD = 0.27 at ground level), represents quite turbid and hazy atmospheric conditions, which is less representative of the ideal clear sky conditions considered when performing the calculations with SMARTS above 12 km. However this dataset still constitutes an extremely useful source for the preliminary assessment involved in this study, since it provides a simple way of integrating these data with the ones provided by Cloudnet. Nevertheless, due to the preliminary nature of the analysis, these assumptions are expected to have a limited effect on the final conclusions inferred. Starting from the observations data provided by the Cloudnet project (for the whole period April 2003-September 2004) integrated with the parameters for ideal clear sky, it is possible to evaluate the daily mean extinction values at different altitudes (0-12 km), for the days available. The daily mean extinction array obtained from the calculation for the month of March is presented in Figure 11.

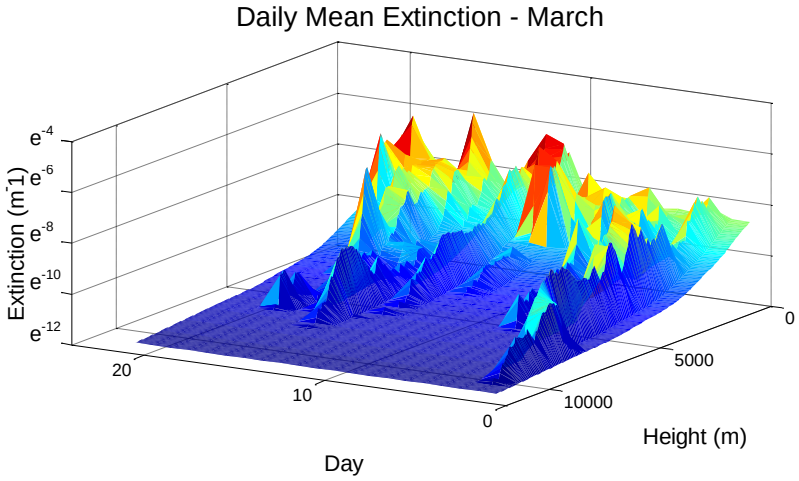

Figure 11 : Daily Mean Extinction (log) for the month of March - Chilbolton Observatory

The monthly mean extinction profile is then obtained for each month and the results for the month of March are presented in Figure 12, which shows that most of the extinction occurs in general below an altitude of about 5 km. From 12 km to 5 km, the extinction parameter goes from $1.0 \cdot e^{-12}$ to $1.0 \cdot e^{-11}$ while for lower altitudes it reaches values of $1.0 \cdot e^{-8}$. This gives an indication of a possible altitude, at which the solar collector should be located, in order to obtain a significant gain in terms of solar radiation that

reaches its surface, and at the same time reducing the disadvantages and the risks that a tethered flying platform at higher altitude can involve.

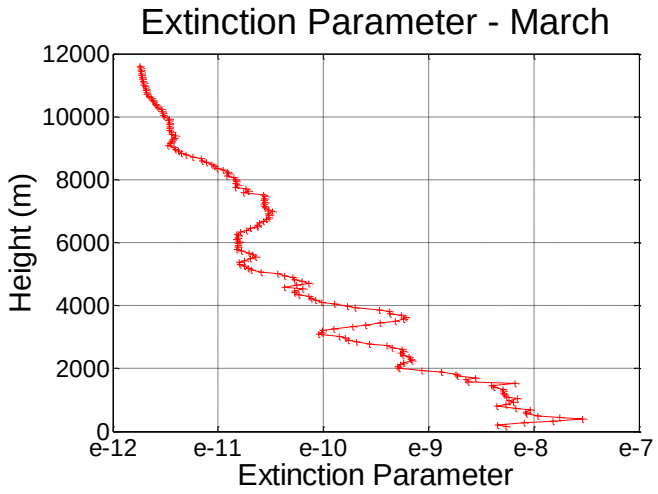

Figure 12 : Extinction Parameter in actual atmosphere conditions - Chilbolton Observatory

The estimate of the irradiance at different altitudes in realistic atmosphere conditions is determined by applying Eq.2.7 to the mean extinction profile, obtained from the Cloudnet project, for each month. The calculation starts from 12 km, assumes clear sky conditions above, and evaluates the irradiance at that height as described in the previous section. Below 12 km, the irradiance at altitude h_j along the vertical can be determined as:

$$I(h_j, \vartheta_Z) = I_{12Km} \exp\left(AM_{REL}(\vartheta_Z) \cdot \sum_{i=1}^{j} \left(-\alpha_i^{Actual} \cdot \Delta h_i \right) \right) \qquad (2.10)$$

where I_{12Km} is the irradiance at 12km, and the sum goes from 12km to the altitude h_j. In Figure 13 the results for the month of March at 12 km, 6 km and on the ground are presented.

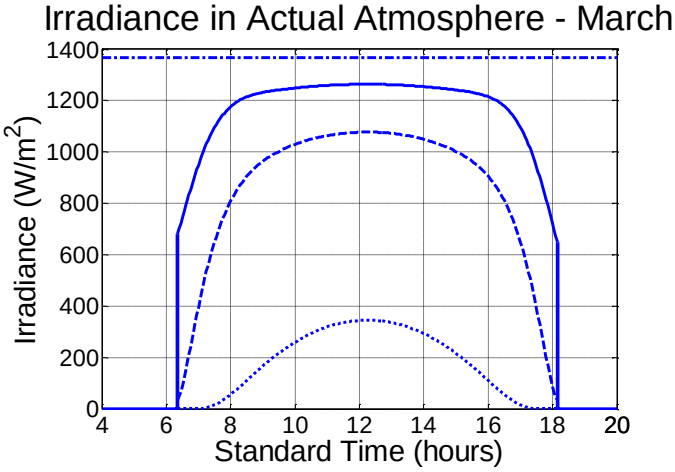

Figure 13 : Irradiance in actual atmosphere at 12 km (solid line), 6 km (dashed line) and on the ground (dotted line), solar constant (dash-dotted line) - Chilbolton Observatory, March

The final step in the procedure for the estimation of the gain that a high altitude solar generator can produce, in terms of solar radiation collected, is the integration of the irradiance (which is the instantaneous power falling on the surface) to get the irradiation value, which defines the energy that reaches the platform in a certain amount of time. The comparison between this value and the one obtained for a ground based system is then used to quantify the potential gain that this kind of solution can bring compared to a ground based solar collector.

The integration of the beam irradiance during the day (from sunrise to sunset), leads to the determination of the total beam energy (*beam irradiation* E_B) that can fall on a surface located at different altitudes above the sea level, and sun pointing:

$$E_B(h) = \int_{SR}^{SS} I_B(h)dt \tag{2.11}$$

where SS and SR are the time of Sunset and Sunrise. Considering an altitude of 6 km (Figure 14), the results obtained show that a beam irradiation of about 3600 kWh/m^2 can reach that layer in one year.

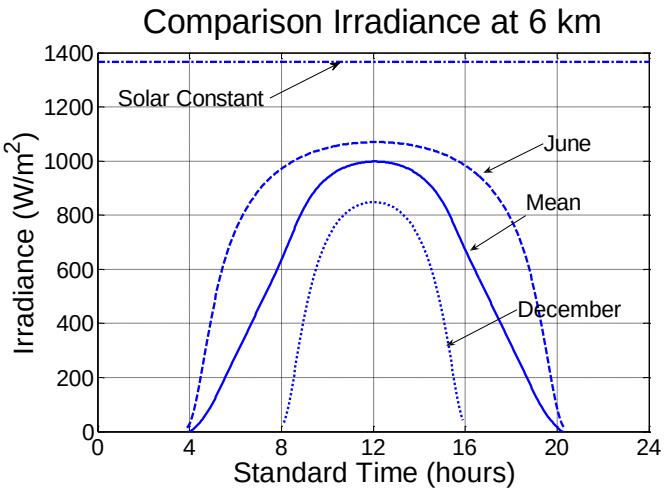

Figure 14 : Comparison between irradiance at 6km for different monthly means - Chilbolton Observatory

A comparison between the values of beam irradiation that can fall on a surface at higher altitude (9 km and 12 km) can be useful to evaluate the possible advantage that could be achieved, locating a solar energy collector at these altitudes (Table 1).

Altitude	Year Beam Irradiation	Year Beam Irradiation (clear sky)
6 km	3600 kWh/m^2	4530 kWh/m^2
9 km	4710 kWh/m^2	4800 kWh/m^2
12 km	5310 kWh/m^2	5310 kWh/m^2

Table 1 : Mean Daily Irradiation at 6km for each month - Chilbolton Observatory

2.3.2 Global Radiation Evaluation

The calculations presented in the previous sections concern the estimate of the attenuation that light experiences as it travels through the atmosphere, in order to determine the potential advantage of a flying platform for PV cells. The analysis, so far, has been limited to the study of the direct beam component of the light, which can be evaluated through the use of *Lambert-Beers' attenuation law*, and using extinction parameters in clear and actual sky conditions. The diffuse component of the irradiance, however, can provide a significant portion of the energy that reaches a surface, especially when considering a ground based panel, under an overcast sky. As an example, for the location of Chilbolton (51.1445 N, 1.4370 W), the value of the ratio between diffuse and global radiation [8] that reaches the ground can vary for different months as shown in Figure 15.

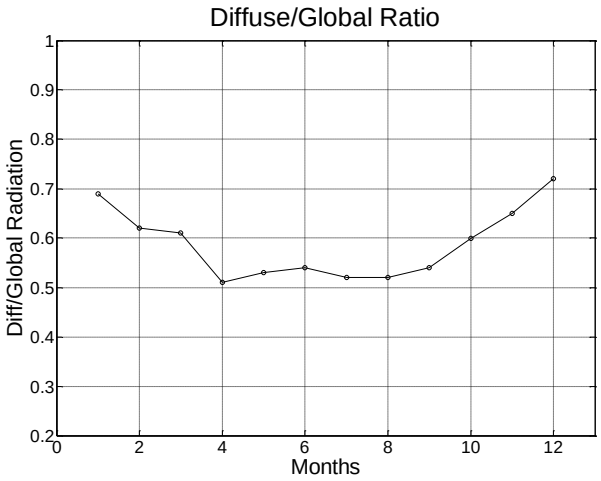

Figure 15 : Ratio between Diffuse and Global Radiation for Chilbolton

As the altitude of the surface considered is increased above the ground level, the diffuse component of the radiation reaching that surface will reduce. An estimate of the ratio between diffuse and global radiation at different altitudes can be determined, for clear atmosphere conditions, using SMARTS [45].

Considering a sun pointing surface located at an altitude of 12 km and 6 km above the ground, the yearly mean value for the ratio between diffuse and global irradiation range from about 5% (12 km) to 6% (6 km). It must be noticed that the estimate is conservative, since it considers ideal atmospheric conditions in complete absence of clouds. The values can become significantly higher with the presence of clouds above the height at which the surface is placed. Based on the figures above, it is possible to include the diffuse component in the results presented in Table 1, and the total solar

energy that can fall on a high altitude collector can be determined. Considering a value of 6% for the ratio between diffuse and global radiation at 6 km, a final value of about 3830 kWh/m^2 is obtained at that altitude.

Considering the extreme solution of the Solar Power Satellite (SPS) concept explored by Glaser et al. [11,12], it is possible to have a more complete view of the range of gains that it might be possible to achieve through the use of a flying platform. The SPS consists of an extraterrestrial sun tracking surface that could collect an average irradiance of I_{TOP}=1367 W/m^2, 24 hours a day, every day of the year. The total irradiation reaching this kind of surface would be about 12000 kWh/m^2. Table 2 provides an overview of the different possibilities presented.

Altitude	Year Global Irradiation
Ground Based (Chilbolton)	1150 kWh/m^2
6 km	3830 kWh/m^2
9 km	4985 kWh/m^2
12 km	5590 kWh/m^2
Solar Power Satellite	12000 kWh/m^2

Table 2 : Comparison between the year global irradiation (including diffuse) values at different altitudes for Chilbolton Observatory

The values estimated can be used for a first assessment of the potential advantage derived from the employment of a PV generator located at high altitude when compared to the total irradiation falling on a typical ground based collector. In general, ground based PV systems are facing towards the equator and tilted at a fixed angle close to the latitude of the location. In this case the value of year global irradiation derived by PVGIS (Photovoltaic Geographical Information System) [8] for Chilbolton is about 1150 kWh/m^2 for surface located on the ground, facing South and tilted at an angle of about 51°.

2.3.3 Reflected Radiation

As mentioned in the previous sections, the result of the interaction between the atmosphere and the radiation travelling through it, is the decomposition of total energy falling on a collector into two main contributions, i.e. direct and diffuse. These two components depend on the characteristics of the atmosphere located above the collecting surface. However, in the case of a tilted collector, the characteristics of the surface located below are equally important as they can contribute to the total energy budget, reflecting a significant amount of radiation, which is defined as albedo.

The albedo radiation factor can have different values, ranging from 0.05 of dark and wet soil, to 0.9 for a layer of thick clouds as presented in Table 3. Even for a satellite in Low Earth Orbit, this figure can reach a value of 0.1 [65].

Surface	Details	Albedo
Soil	Dark and Wet	0.05 – 0.40
	Light and Dry	
Sand		0.15 - 0.45
Grass	Long	0.16 – 0.26
	Short	
Agricultural Crops		0.18 – 0.25
Tundra		0.18 – 0.25
Forest	Deciduous	0.15 – 0.20
	Coniferous	0.05 – 0.15
Water	Small Zenith Angle	0.03 – 0.10
	Large Zenith Angle	0.10 – 1.00
Snow	Old	0.40 – 0.95
	Fresh	
Ice	Sea	0.30 – 0.45
	Glacier	0.20 – 0.40
Clouds	Thick	0.60 – 0.90
	Thin	0.30 – 0.50

Table 3 : Reflection Factor (Albedo) [66],[67]

As a consequence this contribution might not be negligible, in particular in the case of the high altitude collector located above the clouds. However it is still difficult at this stage of the research to provide a reasonable figure for the reflected radiation contribution as its value strongly depends on the orientation of the collector respect to the reflecting surface. It must be also considered that the collector would be pointing at the sun and only part of its surface would be exposed to the albedo radiation. Having considered this, as a first conservative estimate the albedo component of the irradiation is not included in this calculation in order to avoid possible overestimate of this contribution. Nevertheless further activities will need to include the accurate determination of this component in order to get an accurate estimate of the potential of this technology.

2.3.4 Discussion

The results presented can be used to assess the potential advantage of using a platform located at high altitude, to collect the solar radiation. This advantage derives mainly from the reduced attenuation of the atmosphere and the lack of clouds at high altitude. For the location described here, it is estimated that there is a gain in irradiation of between 3.3 and 4.9 for a collector located between an altitude of 6km and 12km, compared to a typical ground based PV system. The assumptions that have been made during the calculations imply some limitations to the possible applications of the figures

obtained. First of all the data are for a specific location in the UK and the generalisation of the results requires a certain degree of approximation, which can be accepted only in the context of a preliminary study. In addition, the acquisition of the experimental data covers a defined period of time and possible limitations due to variability of cloudiness in different years might affect the results presented.

However, it has to be noticed that the mid latitude of the location considered here is relatively well placed (relative to other locations in the UK) to collect solar energy on the ground, and the above mentioned irradiation gains are expected to become higher for installations in the central and northern regions of the UK.

Placing a PV system at high altitude would therefore allow considerably more energy to be collected than on the ground. Also it is interesting to notice that a collector placed at an altitude of 12km could collect around 45% of what could be collected by the same PV system in a geostationary position (i.e. Solar Power Satellite solution), where the effect of the eclipse period can be considered negligible. Figure 16 summarises the results obtained for altitudes up to 50 km, introducing the cloud effect below 12 km.

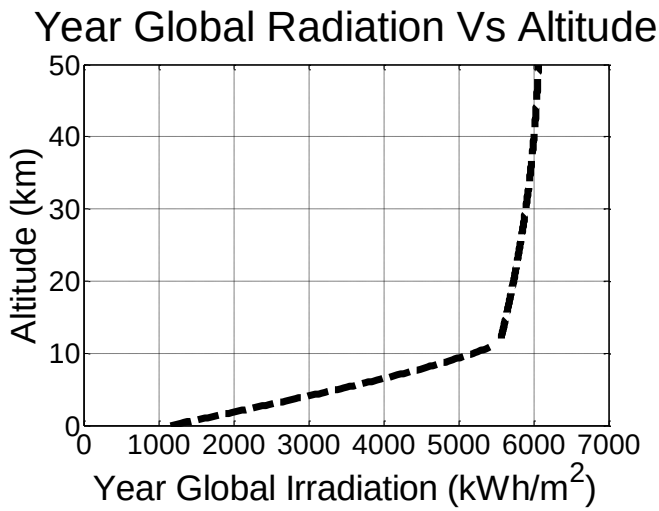

Figure 16 : Year global irradiation values at different altitudes for Chilbolton Observatory

In the following phases of the project, the choice of an operating altitude for the platform will be crucial. This choice has to be based on different considerations. First of all the cloud coverage at different altitudes and the irradiation reaching the various layers of the atmosphere must be taken into account in order to achieve a significant advantage compare to a ground based collector. Secondly there are technical issues to be considered which become more important at higher target altitudes. Finally there are also concerns involving safety and regulatory issues that would limit the maximum operational height. The selected height needs therefore to be a trade off between the

improved advantage that can be obtained at higher layers in the atmosphere in terms of solar radiation collected, and the increased technical and non technical (regulatory, economical…) challenges that the development of the flying platform involves. Technical issues in particular are strongly related to the environmental conditions that the system encounters during its operational life. These conditions are considered and assessed in the next section in order to evaluate their impact on the determination of the maximum altitude that can be achieved.

3 ATMOSPHERIC CONDITIONS

After the definition of the total irradiation falling on the high altitude platform, this section completes the evaluation of the environment in which the system is due to operate by focusing on the preliminary determination of the atmospheric characteristics for different layers above the ground. The main characteristics considered are:

- Atmospheric Temperature Profile
- Atmospheric Pressure Profile
- Atmospheric Density Profile
- Wind Speed Profile

These parameters are important as they have a strong influence on the performance of a lighter than air vehicle. The main feature affected by variations in these parameters is buoyancy whose maximum value represents a limit for the total weight of the system. Moreover the largest load applied to the system is due to the aerodynamic drag force acting on the platform which depends on the geometric shape of the generator, air density and on the absolute value of the wind speed. It is therefore necessary to determine the mean wind speed profile at different heights above the ground as well as to quantify possible unsteady atmospheric conditions in order to evaluate the aerodynamic loads applied to the system.

The atmospheric characteristics mentioned above will be assessed and a target value for the operational altitude will be evaluated.

3.1 Standard atmosphere

The calculations presented in this study are based on atmospheric characteristics derived from the U.S. Standard Atmosphere [68] which can be employed to define the temperature, pressure and density profiles up to an altitude of about 80 km above the ground. This model is widely accepted in the aerospace sector to identify the operational conditions of flying vehicles and it is therefore considered suitable for the present purpose. The current analysis is limited to a maximum altitude of 15 km which seems reasonable, based on the previous considerations inferred about the solar radiation in section 2. The U.S. Standard Atmosphere model assumes the following conditions at sea level ($H = 0$):

$$Temp_{Air}^{SL} = Temp_{Air}(0) = 288.15K \tag{3.1}$$

$$p_{Air}^{SL} = p_{Air}(0) = 101{,}325 Pa \tag{3.2}$$

$$\rho_{Air}^{SL} = \rho_{Air}(0) = 1.225 kg/m^3 \tag{3.3}$$

For altitudes H (expressed in km) between 0 km and 11 km, atmospheric temperature [K] and pressure [Pa] are determined as:

$$Temp_{Air}(H) = Temp_{Air}^{SL} - 6.5 \cdot H \tag{3.4}$$

$$p_{Air}(H) = p_{Air}^{SL} \cdot \left(\frac{288.15}{Temp_{Air}} \right)^{-5.255877} \tag{3.5}$$

while for altitudes between 11 km and 20 km, the equations used are:

$$Temp_{Air}(H) = 216.65 \tag{3.6}$$

$$p_{Air}(H) = 22{,}632 \cdot \exp\left(-0.1577 \cdot (H - 11)\right) \tag{3.7}$$

The atmospheric density [kg/m^3] profile is calculated assuming air as a perfect gas:

$$\rho_{Air} = \frac{p_{Air}}{R_{Air} \cdot Temp_{Air}} \tag{3.8}$$

with the gas constant [J/(kg K)] for air being:

$$R_{Air} = 287.053 \tag{3.9}$$

Another important parameter to be defined when dealing with aerodynamic forces is the viscosity of air μ_{Air} [(N s)/m^2], which can be calculated with the Sutherland's law [69] as a function of the temperature:

$$\mu_{Air} = \frac{\beta \cdot (Temp_{Air})^{\frac{3}{2}}}{Temp_{Air} + S} \tag{3.10}$$

Where the constants β and S are equal to:

$$\beta = 1.458e-6 \ kg/(s \cdot m \cdot \sqrt{K}) \tag{3.11}$$

$$S = 110.4 \ K. \tag{3.12}$$

Figure 17 and Figure 18 present the results obtained, which will be used in the calculations performed in the following sections.

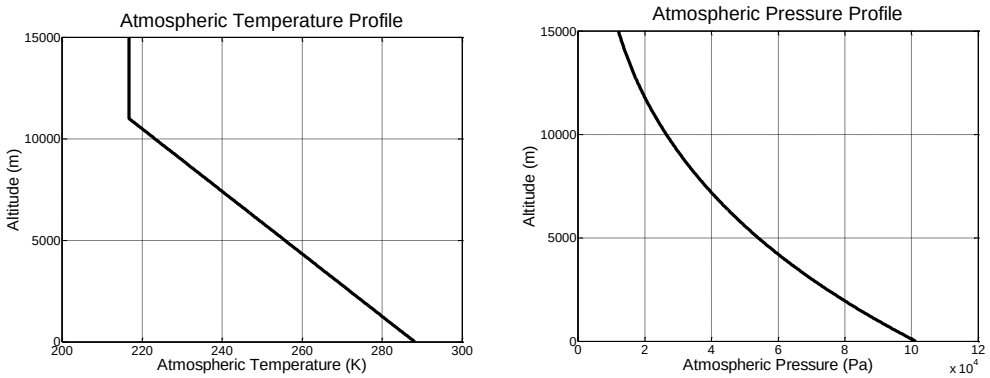

Figure 17 : Atmospheric Temperature and Pressure Profiles

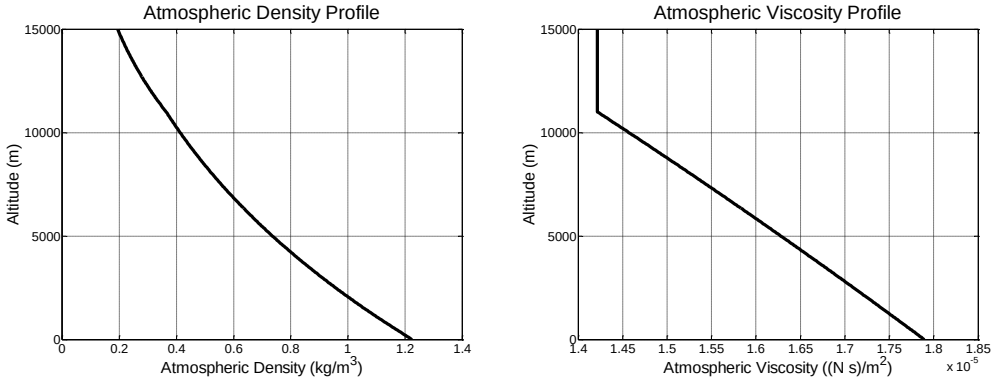

Figure 18 : Atmospheric Density and Viscosity Profiles

3.2 Mean Wind Speed Profile

The wind speed calculations are based on a statistical model, which is applied to an experimental dataset acquired for different atmospheric layers above the ground. The wind speed data used in the model calculations were provided by the Natural Research Council (NERC), from the Mesosphere-Stratosphere-Troposphere (MST) radar station located at Capel Dewi (52.42˚N, 4.01˚W), near Aberystwyth in west Wales, UK [70]. This station acquires the vertical and horizontal speed of the wind every day continuously at interval of about 3 minutes in time, covering the approximate altitude range 2-20 km with a resolution of 300 m. The resulting database is an array of data which describes the wind speed variation in the time period and in the altitude range considered. For each altitude in this range, the horizontal wind speed measurements relative to the period January-December 2007 are elaborated to obtain the mean wind speed that can be expected. The statistical distribution used to model the dataset is the Weibull probability density function $Pdf\left(V_{Wind}\right)$, which is widely employed in the wind energy industry to assess the potential location of the generators [71]:

$$Pdf\left(V_{Wind}\right)=\frac{k}{c}\left(\frac{V_{Wind}}{c}\right)^{k-1}\exp\left[-\left(\frac{V_{Wind}}{c}\right)^{k}\right] \tag{3.13}$$

where c is the Weibull scale parameter and k is the Weibull shape parameter. In order to preliminarily check whether the wind data can be modelled with this kind of distribution, a graphical method based on the cumulative distribution function $Cdf\left(V_{Wind}\right)$ can be applied. This function can be written as:

$$Cdf\left(V_{Wind}\right)=1-\exp\left[-\left(\frac{V_{Wind}}{c}\right)^{k}\right] \tag{3.14}$$

and it can be rearranged to obtain the following expression:

$$\ln\left\{-\ln\left[1-Cdf\left(V_{Wind}\right)\right]\right\}=k\ln V_{Wind}-k\ln c \tag{3.15}$$

which represents a line of slope k and intercept $-k\ln c$.

By plotting the values of $\ln\left\{-\ln\left[1-Cdf\left(V_{Wind}\right)\right]\right\}$ obtained for the wind speed dataset (Weibull probability plot) it is possible to assess if the results can be effectively approximated with a straight line and as a consequence if they could come from a Weibull distribution. As an example the results obtained for the horizontal speed at an altitude of 6 km is presented in Figure 19. The plot confirms the hypothesis that the wind speed experimental data can be effectively modelled with the Weibull distribution. Moreover the interpolating line can be used to determine the values of c and k.

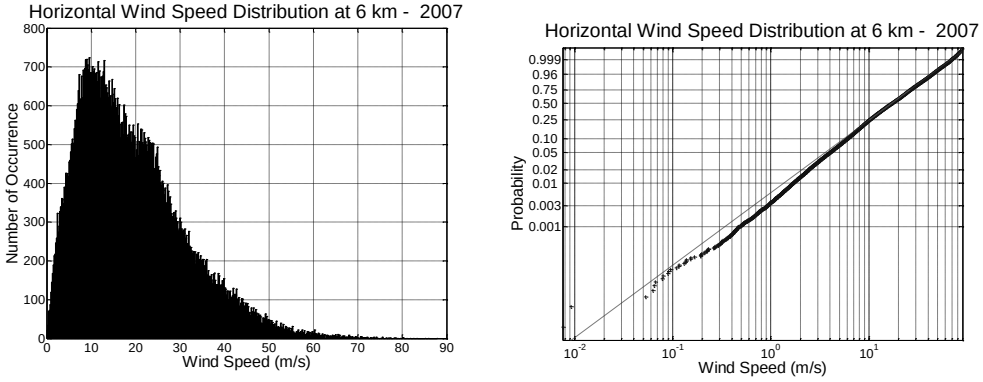

Figure 19 : Wind Speed Weibull Distribution (6 km altitude)

Having determined these values, the mean and variance for each altitude can be calculated as:

$$\overline{V_{Wind}}=c\cdot\Gamma\left(1+\frac{1}{k}\right) \tag{3.16}$$

$$\sigma_{Wind}^{2}=c^{2}\left[\Gamma\left(1+\frac{2}{k}\right)-\Gamma^{2}\left(1+\frac{1}{k}\right)\right] \tag{3.17}$$

where Γ is the gamma function [72], which allow to determine the mean and max (3 sigma value) wind speed for a particular height. The results obtained for each altitude up to 15 km are combined (fitting the data to cover the 0-2 km range) in order to obtain the mean and max wind profile shown in Figure 20. In later calculations both these profiles will be employed to estimate the aerodynamic loads applied to the system in operational conditions.

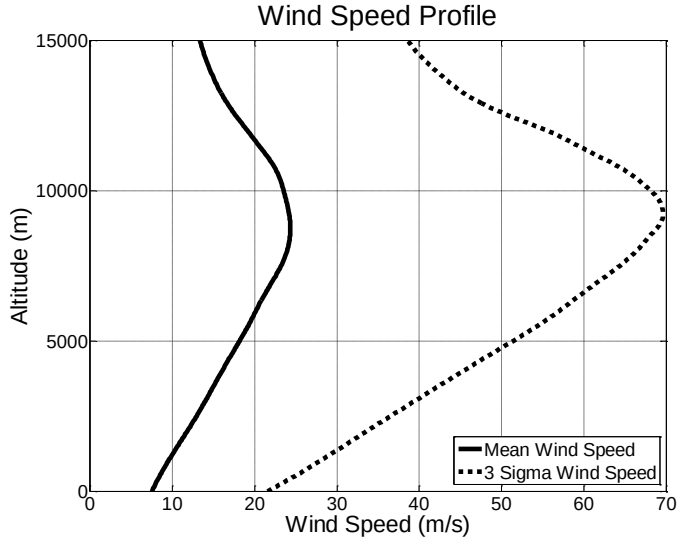

Figure 20 : Wind Speed Profile

Having determined the atmospheric density and wind speed [m/s] profiles, it is possible to evaluate the mean value of the dynamic pressure [Pa] at different altitudes as:

$$q = \frac{1}{2}\rho_{Air} V_{Wind}^2 \tag{3.18}$$

The results obtained for this parameter, which is directly proportional to the aerodynamic loads, are presented in Figure 21.

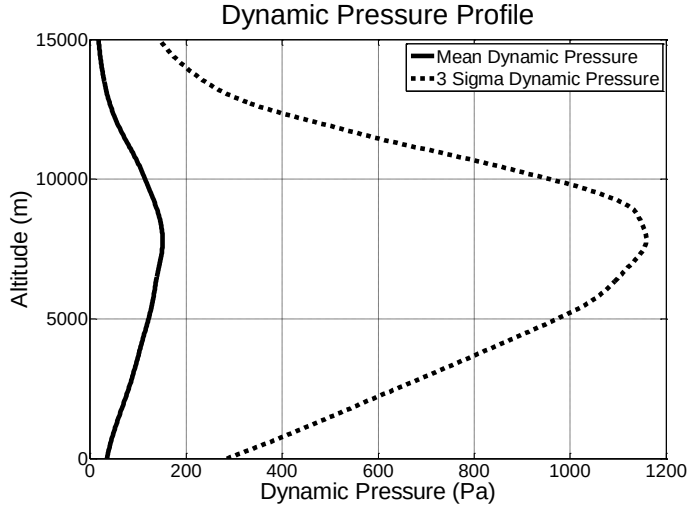

Figure 21 : Dynamic Pressure Profile

It is important to notice that the altitude relative to the maximum dynamic pressure is not the same altitude at which the maximum wind speed occurs due to the decreasing profile of the atmospheric density. The peak in the mean wind speed (24.3 m/s) is found at an altitude of about 8700 m where the jet stream is located. On the other hand the peak in the dynamic pressure (1150.9 Pa) occurs at an altitude of about 7800 m. Therefore at this height the aerodynamic loads on the system are expected to be more severe.

3.3 Atmospheric Turbulence

Although the mean wind speed determined in section 3.2 represents the very first phase in the evaluation of the aerodynamic forces on the system, it is important to include in the calculations the possible effect of unsteady atmospheric conditions. These unsteady conditions are defined in sections 3.3.1 and 3.3.2 in terms of single gusts and continuous atmospheric turbulence.

3.3.1 Single Gust

A gust is defined in the Glossary of meteorology [73] as "a sudden brief increase in the speed of the wind. It is more of a transient character than a squall and is followed by a lull of slackening in the wind speed". The most widely used profile to represent a single discrete gust is the (1-cosine) shape [74] defined as:

$$V_{Gust} = \frac{V_{Max}}{2}\left(1-\cos\frac{\pi \cdot x}{H}\right) \tag{3.19}$$

in which V_{Max} is the peak gust velocity [m/s], x is the penetration distance [m] ($0 \le x \le 2H$) and H is the discrete gust gradient length [m].

According to the Airship Design Criteria [74], the maximum gust gradient length that has to be explored is about 250 m. Moreover, for what concerns the maximum gust velocity V_{Max}, the criteria suggest a value comprised between 7.5 m/s and 10.5 m/s depending on the flying speed of the vehicle. In the particular case of the tethered aerostat, the flying speed can't be univocally defined (even though it can be assumed to be equal to the relative wind speed). As a conservative assumption the maximum gust velocity is set to 10.5 m/s.

3.3.2 Continuous Atmospheric Turbulence

The continuous atmospheric turbulence is assumed to be a stochastic process which can be represented in terms of statistical properties like turbulence intensity, scale length and spectra. The method used for the simulations is based on the Von Karman model which provides the following power spectral density representations as a function of the wave number Ω [rad/m], for the gust velocity in the three directions [75]:

$$\Phi_u(\Omega) = \left(\frac{\sigma_u}{\overline{V_{Wind}}} \right)^2 \overline{V_{Wind}}^2 \frac{L_u}{\pi} \cdot \frac{1}{\left[1 + (1.339 L_u \Omega)^2\right]^{\frac{5}{6}}}$$

(3.20)

for the longitudinal direction,

$$\Phi_v(\Omega) = \left(\frac{\sigma_v}{\overline{V_{Wind}}} \right)^2 \overline{V_{Wind}}^2 \frac{L_v}{2\pi} \cdot \frac{1 + \frac{8}{3}(1.339 L_v \Omega)^2}{\left[1 + (1.339 L_v \Omega)^2\right]^{\frac{11}{16}}} \tag{3.21}$$

for the lateral direction and

$$\Phi_w(\Omega) = \left(\frac{\sigma_w}{\overline{V_{Wind}}} \right)^2 \overline{V_{Wind}}^2 \frac{L_w}{2\pi} \cdot \frac{1 + \frac{8}{3}(1.339 L_w \Omega)^2}{\left[1 + (1.339 L_w \Omega)^2\right]^{\frac{11}{16}}} \tag{3.22}$$

for the vertical. The variables L_u, L_v and L_w represent the continuous turbulence scale length which for altitudes above 2000 ft ($\cong 600m$) can be set to 2500 ft ($\cong 760m$) while the terms σ_u, σ_v and σ_w represent the turbulence intensities in the three directions. The term $\overline{V_{Wind}}$ represents the mean wind speed at a specific altitude as determined in section 3.2.

Considering a frozen field approximation for the temporal and spatial gust correlations, the three components can be generated as described in [76]-[78]. The method considers the following relations for the turbulence intensities in the three directions:

$$\begin{aligned} &\frac{\sigma_u}{\overline{V_{Wind}}} = 0.1 \\ &\frac{\sigma_v}{\sigma_u} = 1 \\ &\frac{\sigma_w}{\sigma_u} = 1 \end{aligned} \tag{3.23}$$

Moreover the method divides the wave number range of the spectrum Φ into a defined number of intervals (depending on the maximum frequency that needs to be

represented) and randomly chooses a wave number for each interval to compute the value of the power spectral density.

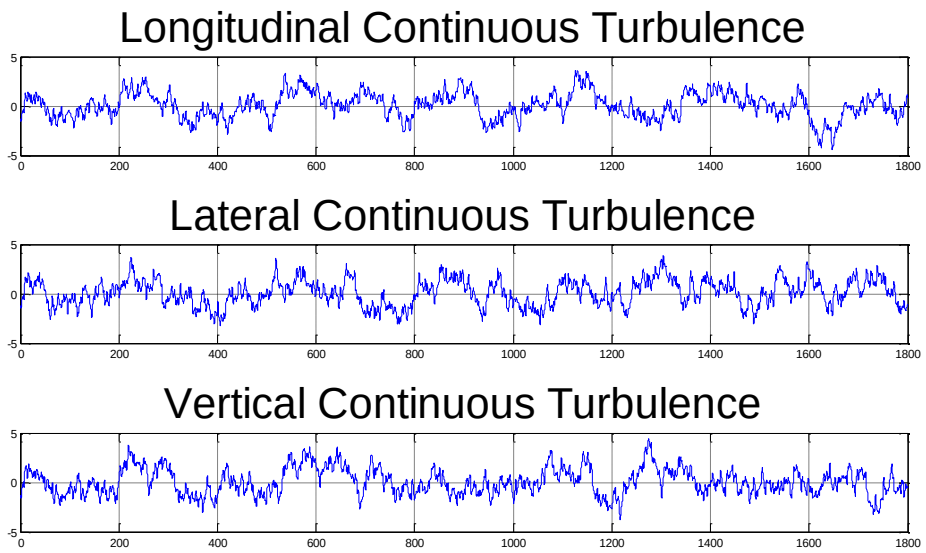

Figure 22 : Continuous Turbulence ([m/s]) Generated with Von Karman Method

The contributions for different wave numbers are then combined to obtain the time representation of the atmospheric turbulence. A 30 minutes simulated turbulence (using mean wind speed value at 6000 m altitude) obtained with this method along the three directions is presented as an example in Figure 22.

3.4 Discussion

After the calculations about the solar radiation reaching different atmospheric layers, some considerations were inferred about the opportunity of locating the AEPG at a particular altitude in order to obtain a significant advantage in terms of energy collected. Analogous considerations about an operational altitude for the AEPG can be inferred looking at the values of the wind speed obtained at different heights. An accurate figure for the aerodynamic loads can't be obtained yet, as it depends on the geometry of the vehicle and not only on the fluid characteristics. However the results obtained for the mean wind speed and (more importantly) the dynamic pressure values would suggest that in the region around 7800 m of altitude a peak in the aerodynamic drag would occur. On the other hand the figures evaluated for the single gust and continuous turbulence don't seem at the moment to constitute an issue for the corresponding aerodynamic loads, as they represent a small fraction of the mean wind speed profile

determined in section 3.2. Nevertheless they can constitute an issue when the dynamic behaviour of the system is addressed.

Moreover as mentioned earlier, there are also non technical concerns that could limit the value of this parameter. In particular regulatory issues regarding air traffic need to be taken into account even in this early phase of the study. The UK civil aviation authority (CAA) divides the airspace into 6 classes, from A to G. These classes are essentially defined in terms of flight rules and restrictions applied to the air traffic. The classes and relative applicable rules are summarised in Figure 23. Class G is the least restrictive and it comprises most of the airspace up to 6000 m (FL 195).

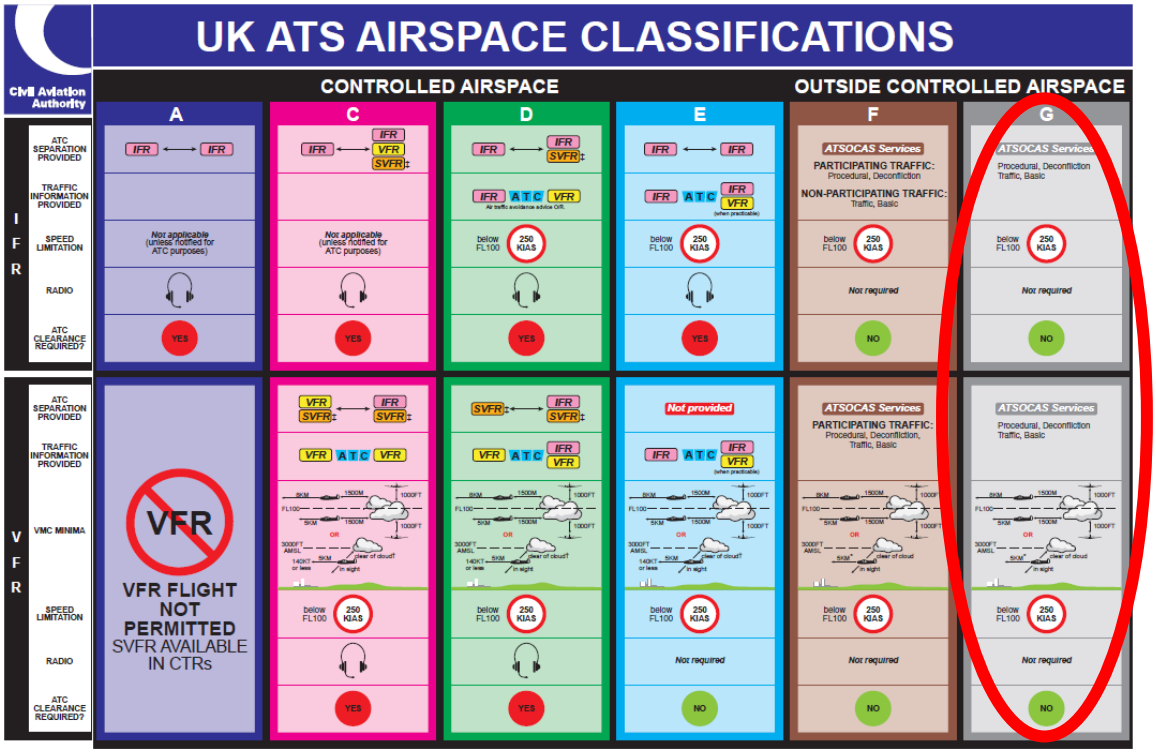

Figure 23 : Civil Aviation Authority Airspace Classification – Class G is highlighted [79]

Therefore, at this stage of the study, it is considered reasonable to set a value for the operational altitude of 6000 m. This height would guarantee a significant advantage in terms of energy collected. At the same time it would avoid technical problems related to the jet stream wind speed at higher altitudes and it would minimise non technical issues related to air traffic regulations. Higher altitudes will be considered in the following phases of the project, if the technical feasibility of the system at this preliminary height is proved.

4 LIGHTER THAN AIR: STATE OF THE ART

The system presented in this report is mainly based on LTA and PV technologies. Therefore the overview provided in this section is mainly focused on this kind of vehicles with attention to the peculiar characteristics of tethered aerostats and the analysis of their capabilities. Moreover a part of the overview is dedicated to systems in which photovoltaic and LTA technologies are integrated. Finally a brief introduction of some flying power generators is included that can be used as a comparison to the system proposed in the study.

4.1 Historical Remarks

Although the LTA technology can be dated back in the 18th century with Montgolfier Brothers' hot balloon (1783), the actual development of this technology occurred during the 19th century with pioneers like the French Henri Giffard, who invented the powered airship in 1852 and Charles Renard who, with the collaboration of Arthur Krebs, built the first airship that could return to its starting point (1884). However the most important period for the success of this type of vehicle is represented by the first decade of the 20th century, mainly due to the achievements in Germany (Friedrichshafen) of the Zeppelins, which was mainly employed for people transportation before the 1st World War. As an example the Zeppelin LZ13 "Hansa" (Figure 24) had a length of 148 m and a diameter of 14 m. It could reach a maximum speed of 78 km/h with a payload mass of 6,300 kg and an autonomy of 1,100 km.

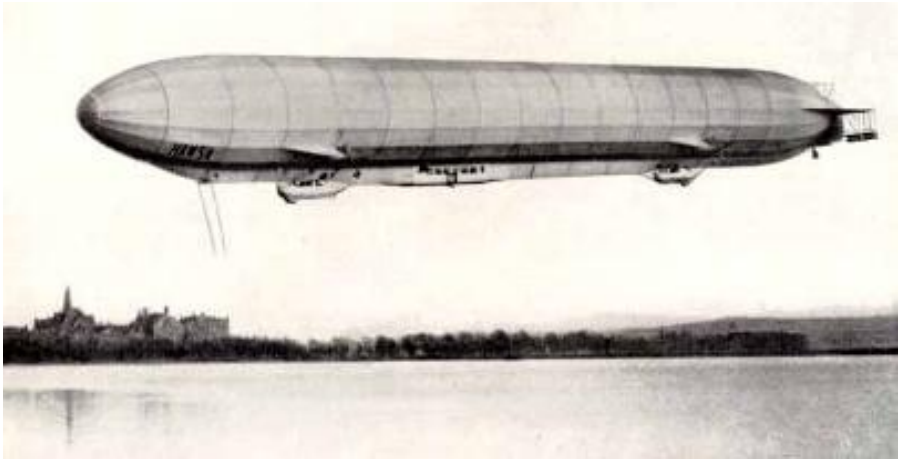

Figure 24 : Zeppelin LZ 13 "Hansa"

During the 1st World War, the main countries involved in the conflict like Germany, Great Britain, France and Italy began employing airships to support military operations

(long distance troops transportation, reconnaissance and bombing) thanks to significant achievements concerning the length of the vehicles (up to 210 m), the speed (130 km/h) maximum altitude (8000 m) and payload mass (50 T).

The progress in this field culminated in the years 20s and 30s both in Europe and in the US. Following the "Airship Imperial Scheme" in 1924 the British Empire developed the famous R100 and R101 while in the US the Navy adopted four large airships, Shenandoah, Akron, Macon and Los Angeles (built by Zeppelin), between the 1923 and 1935 plus other innovative ones like the Metalclad ZMC-2 (in 1929) which operated for about 10 years. Nevertheless the largest and most successful airships were built and operated by the Germans between 1925 and 1937. For example the rigid LZ 127 Graf Zeppelin, operating between 1928 and 1937, was 236.5 m long (total volume of 105,000 m^3) with a useful lift of 60,000 kg, while the Hindenburg was 245 m long and could reach a maximum speed of 135 km/h. These giant vehicles were capable of transporting people and post around the world, mainly to North and South America.

Other important successes of the post war period include the first Atlantic Ocean crossing by the British R34 in 1919 and the two North Pole expeditions by Nobile and Amundsen on board of two Italian semi rigid airships (Norge and Italia) in 1926 and 1928. Unfortunately the accident that occurred to the Hindenburg (245 m long) at Lakehurst (New Jersey – US) in 1937 arrested the further development of the airships, in particular the rigid ones [80, 81]. Non rigid blimps were still employed during the Second World War by the US Army for different applications like patrolling and search and rescue, and some developments continue after the war with the construction of the Goodyear ZP2N-1 in 1957 and the ZPG-3W in 1958, the largest non rigid airship ever built (123 m).

However, thanks to modern technological achievements, airships have recently attracted a renewed interest for different purposes like heavy lift transportation, communication [82], military and surveillance [83] applications. Important contracts have recently been awarded like the $517 million one signed between the US Army and the Northrop Grumman which is going to develop 3 Long Endurance Multi-Intelligence Vehicle (LEMV) in collaboration with Hybrid Air Vehicles Ltd in Cardington, UK. This airship is based on hybrid technology, providing part of the lift with the lighter than air gas contained in the envelope and part with its aerodynamic shape, and it will be capable of flying at about 6 km continuously for 21 days. The same technology is applied by this

company to provide heavy lift capabilities, which is another niche in which airships could be particularly suitable.

4.2 Tethered Aerostats

Another LTA application which is gaining renewed attention is constituted by tethered aerostats. These are non rigid envelopes (blimps) usually filled with helium that, during the 2nd World War, were employed mainly as barrage balloons to defend an area from air attacks at low altitudes. Nowadays tethered aerostats are available in the market from companies like TCOM [84] and Lockheed Martin [85] (US) and RosaeroSystems [86] (Russia). These companies produce different systems usually for military surveillance purposes, as they can constitute a stable and enduring platform for different types of payloads. The mooring tether is used not only to keep the blimp in its position but also to provide the power from the ground to the onboard subsystems, as well as to transmit the data acquired to the ground station. Some of these tethered aerostats equipped with radar are currently employed along the southern U.S. border, Gulf of Mexico and Florida as they are capable of providing a surveillance range of more than 350 km. Other similar systems are in operation both in Iraq and Afghanistan to guarantee protection to land troops and assets against attacks. Table 4 provides an overview of the aerostats currently manufactured by the most important companies operating in this sector.

Name	Len [m]	Vol [m^3]	Alt [m]	PayLoad [kg]
Lockheed Martin 420K	64	12,000	4,600	1,000
Lockheed Martin 74K	35	2,100	1,500	500
TCOM 15M	15	290	300	90
TCOM 32M	32	1,800	900	225
TCOM 71M	71	16,700	4,600	2,300
ROSAERO AU-27	19	450	700	80
ROSAERO GEPARD	27.9	1,200	700-1,500	150-300
ROSAERO PUMA	60.7	11,809	2,000-5,000	< 2,250
ROSAERO JAGUAR	55.2	8,900	1,000-4,000	< 1,700

Table 4 : Capabilities of different tethered aerostats available in the market

It can be noticed that the operating altitude range goes from 300 m to 5,000 m since the weight of the tether increases linearly with height and it usually limits the maximum altitude that can be reached by the balloon. Nevertheless several studies have been carried out to assess the feasibility of tethered balloon systems to be located at altitudes up to 20 km in order, for example, to provide space to ground optical communication as

presented in [87-88]. Moreover these systems are currently being considered for the development of high altitude astronomical platforms [89].

4.3 Photovoltaic Technology applied to LTA

The possibility of applying the PV technology to a lighter than air vehicle has been explored in the past by Khoury who was to first to have the intuition that the solar radiation could constitute a "renewable, free, non polluting and non inflammable fuel" for propulsion as well as to power the different airship subsystems [30] [31]. The feasibility study presented in [31] introduces the concept of a 80 m long "Sunship" with solar cells directly deposited on the envelope material and equipped with electric brushless motors to drive the propellers. Moreover the research focuses its attention on the solar radiation availability, the performance of the system (in terms of maximum speed that could be achieved) and it provides an overview of the main components of the airship as well as some cost analysis. The suggested applications range from surveillance to tourism in those areas like North Africa and Arabian Peninsula where the good weather conditions allow enough power to reach low altitude atmospheric layers.

More recently Knaupp and Schafer [32], have focused their attention on the possible application of photovoltaic cells to the external envelope of an airship, conducting experimental (static and dynamic) mechanical tests on crystalline silicon foil modules on curved and flexible surfaces. Based on the promising results obtained, the feasibility study presented by Knaupp and Mundschau in [33] [34] was carried out, concerning the potential of installing combined photovoltaic-hydrogen energy systems for powering stratospheric platforms.

Moreover, as a result of these studies, one of the most successful projects in Europe related to the integration of PV and LTA technologies is the development of the unmanned demonstration vehicle LOTTE [90] at the Institute for Static and Dynamic of Aerospace Structures at the University of Stuttgart. This vehicle has a maximum diameter of 4 m and a total length of 16 m and it can reach an operating altitude of 1,000 m at a speed of 45 km/h, powered by a silicon solar array attached to the external envelope with Velcro (Figure 25a). With a similar size (22 m long) the Nephelios [91], currently being developed by a team at the Institut National des Sciences Appliquées de Lyon (INSA), will attempt to cross the English Channel powered only by a 2.4 kW photovoltaic array (Figure 25b).

Figure 25 : Airship LOTTE [90] and Nephelios [91]

Since the attenuation of solar radiation is significantly reduced as higher altitudes are considered, the PV technology is the best candidate to provide the necessary power to the different subsystems of high altitude airships (HAA) that need to operate continuously for long periods. As an example, Lockheed Martin [85] has been recently developing a HAA which will be able to fly at around 20 km of altitude for 30 days missions in order to provide surveillance and military services. The system will employ an all electric power system combining thin film PV arrays with high efficiency energy storage media. The endurance is mainly limited by the loss of lifting gas, due to the permeability of the envelope fabric.

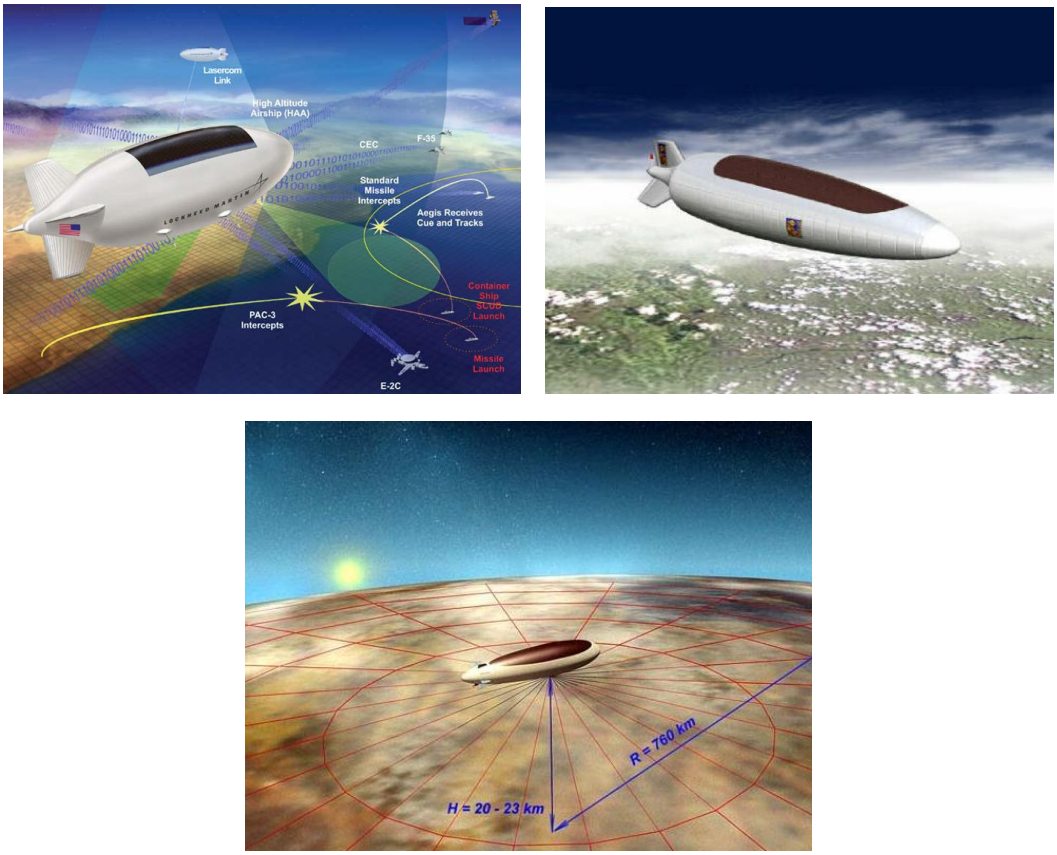

Figure 26 : High Altitude Airships (Lockheed Martin – Lindstrand Tech. – Rosaero Systems)

In Europe, the European Space Agency (ESA) has commissioned the concept design of a High Altitude Long Endurance (HALE) aerostatic craft to Lindstrand Technologies [92], with the purpose of assessing the role that these systems could have in the field of Earth observation and environmental monitoring. The pressurized structure will allow the vehicle to fly at altitudes of about 20 km powering the payload with a combined PV/Fuel cells system. Similar capabilities can be provided by Berkut Airships (Rosaero Systems) [86] with lengths ranging from 150 m to 250 m, able of carrying payloads up to 1,200 kg. The mentioned airships are presented in Figure 26.

4.4 LTA for Power Generation

Some systems that employ LTA technology for power generation have already been considered and some information is available in literature. Although the specific purpose or the design solution might be different from the ones of the system presented in this report, the analysis of the characteristics and capabilities of these concepts is of particular interest in the further development of this study.

The Sun Hope System (Figure 27) proposed by Gurfil and Cory [93] is based on a platform filled with helium and containing embedded PV cells. The system is specifically designed for locations in which the land resources are scarce, since it can constitute an efficient, portable and land independent energy source. The envelope has a paraboloidic shape with a transparent upper surface which allows the light beam to be reflected by the mirror on the lower part and concentrated on a high efficiency PV cell located at the focus point. The balloon is attached to the ground using a dual insulated cable that has the double function of transmitting the power to the ground and carrying the helium to the balloon. The use of a paraboloidic mirror has the advantage of focusing the light beams on the high efficiency solar cell, increasing the insolation to electricity conversion efficiency.

A similar way of reducing the environmental impact of the PV systems by using inflatable balloons has been proposed by Cool Earth Solar [94]. The system shown in Figure 28 consists of an inflated mirror concentrator which focuses the sunlight onto photovoltaic cells therefore increasing the output of these devices. The mirror is constituted by a thin metallized plastic film which reduces the total weight of the system while the envelope is inflated with air providing structural integrity against high wind speed. The inflated membranes can be supported by a frame made of wood poles and

steel cables which guarantees minimal footprint and limited disruption to the natural environment.

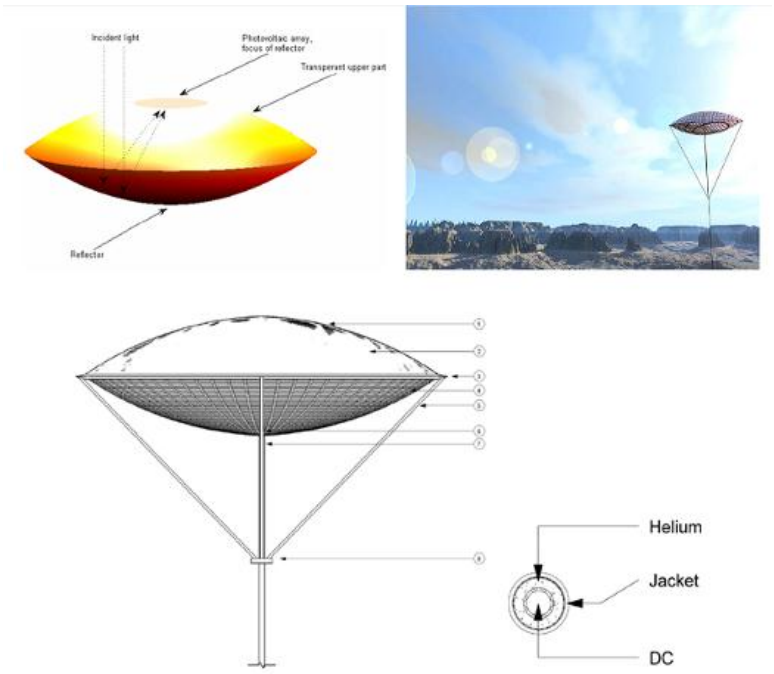

Figure 27 : SunHope System [93]

Figure 28 : Cool Earth Solar [94]

An innovative application of tethered aerostats for electrical power generation has been proposed by Leinnonen [95] to provide support infrastructure for disaster relief and remote communities. Solarial (Figure 29) is a small unmanned hydrogen filled airship (20 m long), which would be able to generate 125 kWh per day of renewable energy thanks to the PV array and to a reversible drive propeller/wind turbine. The generated power is then delivered to the ground via the mooring tether. The aerostat can be

autonomously powered by the PV array constituted by CIGS cells that can be integrally manufactured with the airship's envelope, and a fuel cell system. The altitude control is provided by two dilatation panels located on the bottom of the airship, providing buffer volume for the hydrogen, which is free to expand as altitude, temperature and pressure change. The material used for the tether is aramid-fiber to provide the necessary strength and aluminium as conductor.

Figure 29 : Solarial [95]

Finally it is worth mentioning in this review some concepts that are currently being developed to harness the wind power at high altitudes. Even though these studies don't involve the exploitation of the solar radiation to produce electrical power, they can have some common technical and non technical issues with the system presented in this thesis. The exploitation of wind power at high altitude has recently attracted strong interest by both industry and academia. Several concepts have been proposed, which involve the use of different technologies, such as a ladder mill equipped with aerodynamic profiles [96], a series of kites [97] or a flying rotorcraft [98]. Most of these concepts have been translated into prototypes like Kitegen [99] and Sky WindPower's flying electrical generator [100]. As an example Selsam's Superturbine [101] is essentially constituted by a low-cost turbine equipped with multiple, synchronous, small rotors and with a joint that enables it to tilt. In one of its versions it includes a blimp that, providing lift, it improves the performance of the system (Figure 30). The prototype produced by Selsam, generates 6 kW of power with a wind speed of 50 km/h. A particular application of lighter than air technology in this field is the Magenn Power Air Rotor System [102], which consists of an helium filled turbine (about 5,600 m^3) that

rotates thanks to the winds at an altitude around 300 m, providing a power of about 100 kW. The rotation also causes the Magnus effect that provides additional lift and stability. A similar system (Altaeros [103]) is currently being developed at MIT (Figure 31).

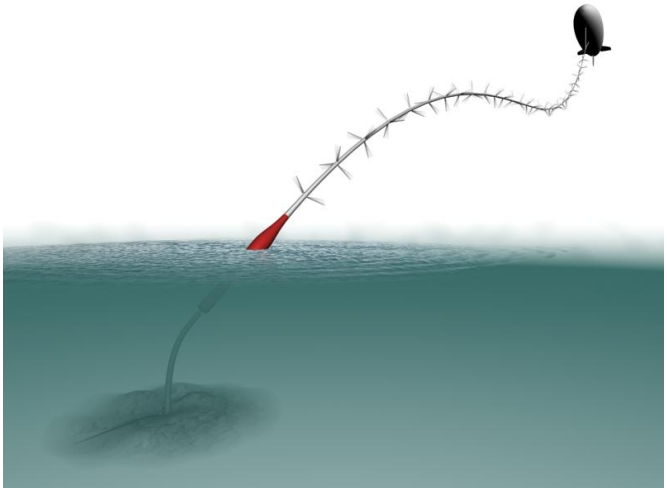

Figure 30 : Selsam's Superturbine [101]

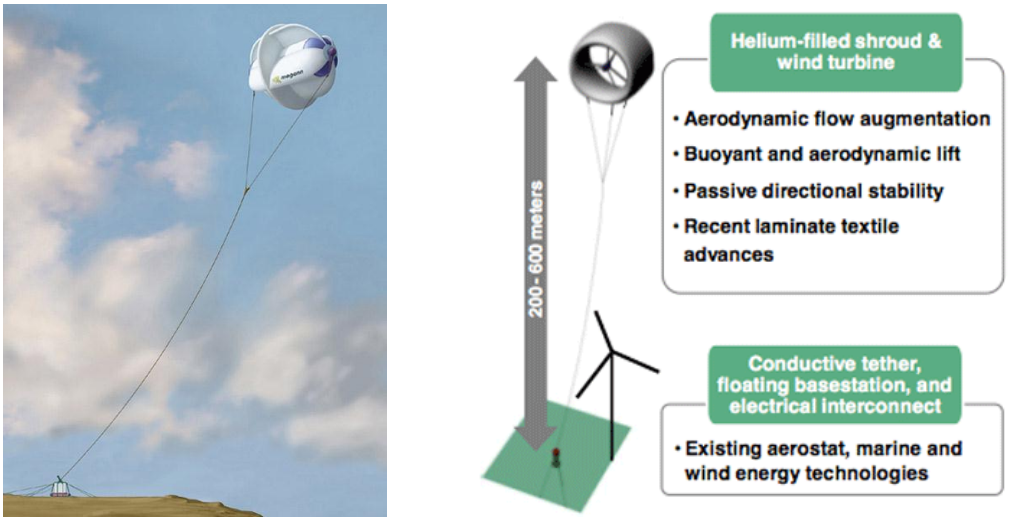

Figure 31 : Magenn [102] and Altaeros [103]

5 PRELIMINARY CONSIDERATIONS

As a LTA high altitude solar collector, the AEPG has to be capable of performing a series of operations in order to deliver to the ground the maximum amount of electric power. The fundamental operations the system has to perform are:

- Ascend to operational altitude
- Maintain the position at operational altitude
- Collect the maximum amount of solar radiation
- Convert solar radiation into electrical power
- Deliver the maximum amount of electrical power to the ground
- Descend to the ground in case this is necessary

In addition to these, operations related to possible safety concerns and system maintenance must also be taken into account.

During the pre operational phase the lighter than air platform has to ascend in order to reach the target height, allowing the lifting gas to expand until the envelope is fully inflated, and providing enough space to locate the different subsystems. The lift generated by the gas needs therefore to overcome the weight of the entire system, which also has to withstand the loads due to the wind speed profile encountered during the ascent. The operational phase includes, first of all, the collection of the solar radiation which is performed by maintaining the position of the platform, reducing to a minimum the horizontal displacements due to the presence of the wind (constant and gusts). Moreover the platform needs to support the solar cells which are responsible for the conversion of the solar radiation collected into electric power. These devices need to be properly oriented in order to minimize the angle of incidence between solar radiation and solar cells surface. The amount of solar energy that can be converted depends on the efficiency of the cells and the amount of the external surface covered. After its generation, the maximum amount of power has to be transmitted to the ground via the mooring tether. Its design needs therefore to reduce effectively the power losses through the use of a low resistivity conductor and the choice of a suitable voltage for transmission.

In the case of severe weather conditions, emergency, or for maintenance purposes the system needs to be able to descend to the ground. During the descent air has to be forced into the envelope to pressurize the lifting gas and the tether needs to be stored at

the ground station. Finally it must be taken into account that the system has to be designed in order to allow the maintenance operations to be performed. In particular these operations are related to possible leak of helium, degradation of envelope and solar cells and the maintenance of the power distribution and control components. On the base of these requirements some preliminary considerations are inferred about the main characteristics of the system.

5.1 AEPG Schematic Representation

In its simplest representation, the AEPG is modelled in this initial phase as a spherical balloon filled with helium tethered to the ground and partially covered by an array of photovoltaic cells (Figure 32).

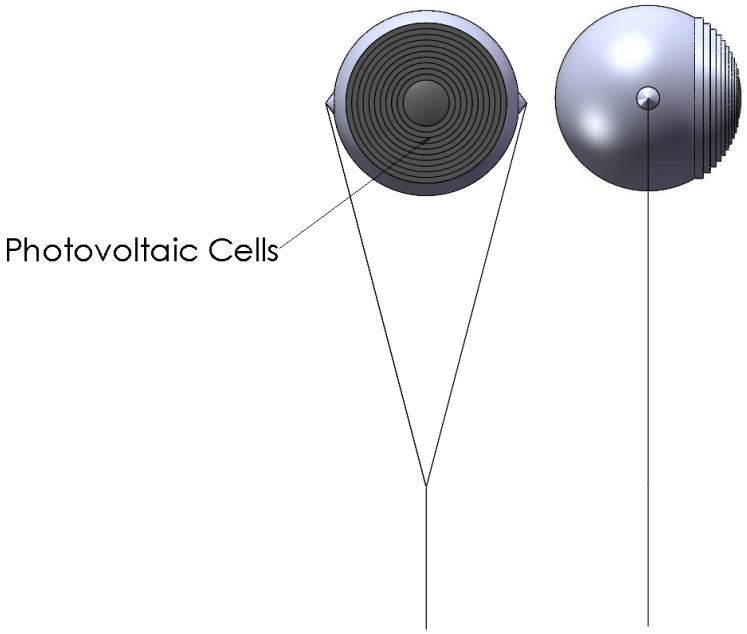

Figure 32 : AEPG Schematic Representation

The PV cells could be attached directly to the spherical envelope of the balloon. However, the maximum power is obtained by pointing the solar cells towards the direction of the sun, since the output of these devices varies with the cosine of the angle between the solar beam and the normal to the cell surface. For this reason it is important to have all the cells attached to parallel surfaces which can be directed towards the same direction at the same time. A way of doing this is by creating a series of steps on the external surface of the balloon in order to compensate for the curvature of the balloon and have all the cells pointing in the same direction. Another important issue related to the pointing requirements concerns the shape of the envelope. In order to effectively reduce the weathervane effect that a streamlined shape would imply, the shape selected

for the external envelope is spherical. As a drawback in this configuration, the drag force on the structure can increase significantly if compared to the typical streamlined shape, which is the most widely used shape for airships, with some exceptions [103-107] (Figure 33). Furthermore the increased aerodynamic drag can be taken into account during the structural design of the system as considered in [108].

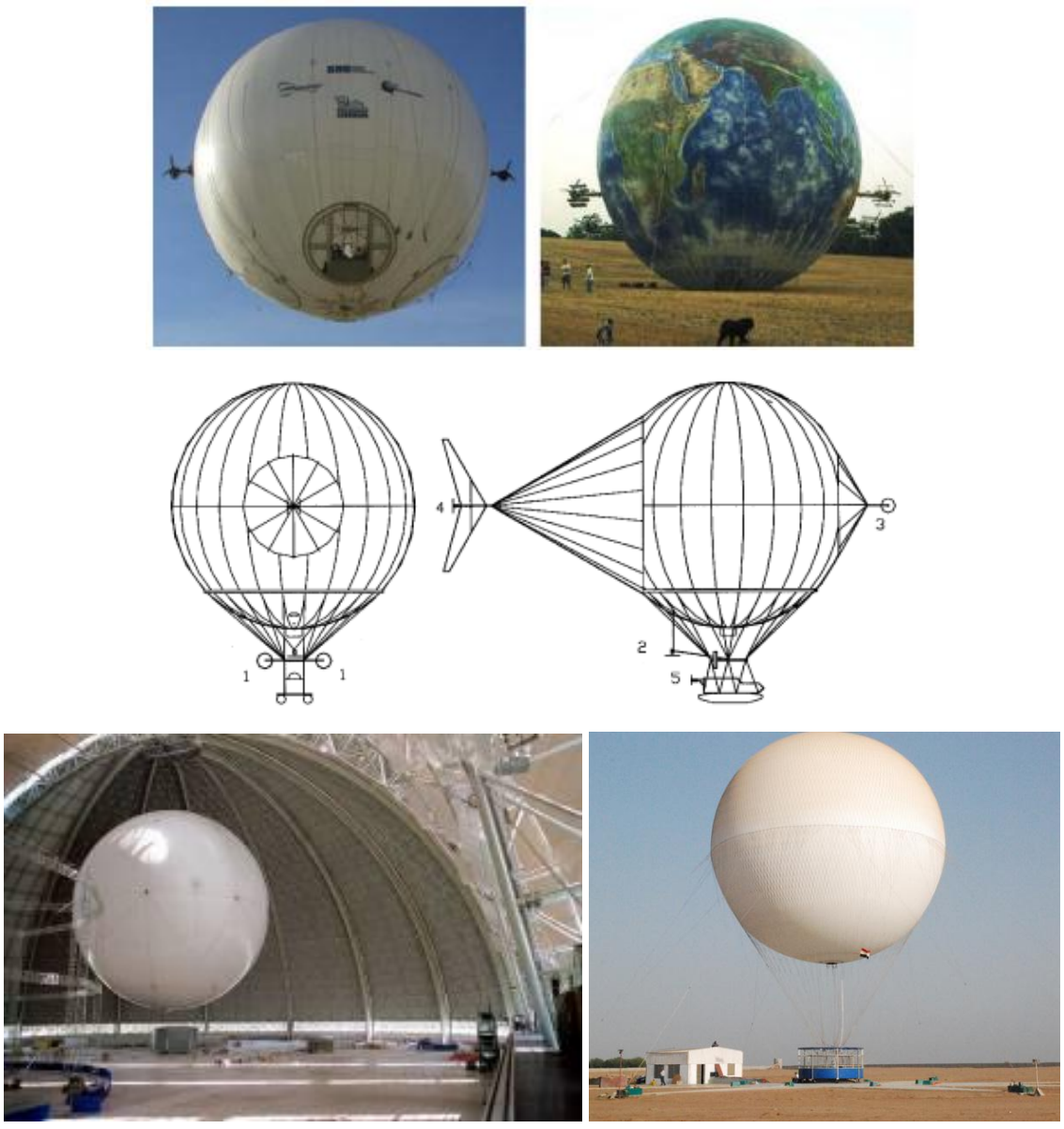

Figure 33 : Spherical shaped airships [103-107]

The final purpose of this chapter is to identify a set of possible configurations to be used as a baseline for the assessment of the technical feasibility of the AEPG. The initial step in this procedure is to define the ranges in which the main parameters describing the system can vary, on the base of several considerations about the main components and determine a set of potentially feasible configurations. These parameters include the disposable lift as a function of the size of the balloon and the operational altitude

chosen, the characteristics of the PV system and those of the power transmission components. The other subsystems which will be considered more in detail in the concept design phase are not specifically included in these preliminary considerations.

5.2 Disposable Lift

The first parameter that needs to be considered in the design is the disposable lift, which is necessary to overcome the weight of the different subsystems (including the cable), the payload and to tension the tether. Its value is mainly determined by the balloon diameter, the envelope material density and the pressure height, defined as the altitude at which the envelope is fully inflated [109].

The density of the atmosphere ρ_{Air} can be determined as discussed in section 3.1, starting from the pressure profile and treating air as a perfect gas. Assuming that the mean internal pressure and temperature are the same as the external atmospheric pressure and temperature (no overheating), and considering the lifting gas as a perfect gas it is possible to determine ρ_{Gas} [kg/m^3] as:

$$\rho_{Gas} = \frac{p_{Air}}{R_{Gas} \cdot Temp_{Air}}. \tag{5.1}$$

In the case of Helium the gas constant [J/(kg K)] is:

$$R_{Helium} = 2078 \ J/kg \cdot K. \tag{5.2}$$

Considering the balloon fully inflated at operational altitude the buoyancy [N] and weight of the lifting gas [N] can be determined as:

$$B = Vol_B \cdot \rho_{Air} \cdot g \tag{5.3}$$

$$W_{Gas} = Vol_B \cdot \rho_{Gas} \cdot g \tag{5.4}$$

where g is the acceleration of gravity (9.81 m/s^2) and the volume of the spherical balloon [m^3] can be calculated from the diameter ϕ_B [m] as:

$$Vol_B = \frac{4}{3}\pi\left(\frac{\phi_B}{2}\right)^3 \tag{5.5}$$

The difference between the buoyancy and the weight of the lifting gas is defined as gross lift [109]:

$$L_G = B - W_{Gas} = Vol_B \cdot (\rho_{Air} - \rho_{Gas}) \cdot g \tag{5.6}$$

The envelope weight W_{Env} [N] depends on the external surface of the balloon and on the density of the material chosen for construction δ_{Env} [kg/m^2]:

$$W_{Env} = 1.33 \cdot \delta_{Env} \cdot Surf_B \cdot g \tag{5.7}$$

where the surface [m^2] is defined as:

$$Surf_B = 4\pi\left(\frac{\phi_B}{2}\right)^2 \tag{5.8}$$

and the factor 1.33 [20] is applied to take into account for the presence of various reinforcements and attachments.

The lift available for the different subsystems and payload (disposable lift) is defined as [109]:

$$L_D = L_G - W_{Env}. \tag{5.9}$$

As far as the balloon size is concerned, modern materials and technologies would allow the construction of very large balloons. However the main limit for the size of the airships is still the facility (the shed or hangar) in which the system is manufactured. At the moment the largest shed in the world has a length of 360 m, a width of 210 m and a height of 107 m. Located 60 km south of Berlin it was designed to accommodate the planned Cargolifter CL 160, but is now being used for other purposes. Having considered this, the maximum balloon diameter assumed for this analysis is 100 m, which seems a reasonable upper limit since it has been chosen in other studies such as the one presented in [87]. On the other hand the envelope material density (δ_{Env}) usually depends on the size of the airship [109]. As a preliminary figure this parameter can be set to 0.5 kg/m^2, which is the value relative to the commonly used 402 fabric provided by Lindstrand Technologies [110]. It must be pointed out that more advanced materials, like the ones employed in the design of HALE [92], can have densities as low as 0.295 kg/m^2 (See Appendix B for specific characteristics of materials).

Considering a range of pressure heights between 6 km and 12 km the disposable lift can be determined as a function of the balloon diameter. With a diameter of 100 m a maximum disposable lift between 1.17 MN and 2.7 MN can be obtained (i.e. between 120 Tons and 275 Tons, Figure 34). These results, together with the estimate of the weight of the different system components, are the starting point in the evaluation of the range of diameters suitable for the design.

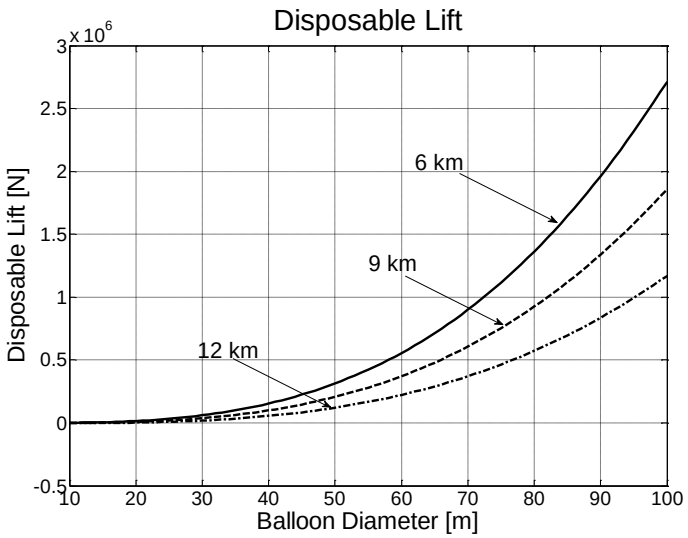

Figure 34 : Disposable Lift for different values of the balloon diameter and pressure height

5.3 PV Array Characteristics

A comprehensive description of the state of the art in PV technology can be found in [111]. Appendix A summarizes the main information included in [111], presenting an introduction about the basic principles of a PV cells. The following sections provide an overview of the main types employed in current applications.

5.3.1 PV Cells Types

Research in the field of PVs is very active and diversified, involving different materials and technologies [112]. The present analysis will focus on solar cells types which could be potentially employed for the design of the AEPG, introducing their main characteristics. In particular possible values for efficiency and specific power [W/kg] are preliminarily assessed in order to provide reasonable figures to be used for the exploratory calculations.

Crystalline Silicon Solar Cells

Crystalline silicon solar cells are the most widely employed in terrestrial applications. The highest efficiency obtained with this material at the cell level is approaching the theoretical limit of 25% in the case of monocrystalline and 20% in the case of multicrystalline [112]. It must be pointed out that these figures have been obtained in research laboratories. The actual efficiency values of silicon solar cell available in the market can be significantly lower as presented in Table 5 and Table 6 for different manufacturers.

Manufacturer	Efficiency [%]
Sandia Laboratory	25.00
QCells	17.40
Bosch	18.43
JaSolar	18.00

Table 5 : Monocrystalline Silicon Cells Efficiency Available in the Market

Manufacturer	Efficiency [%]
NREL Laboratory	20.40
QCells	17.00
Bosch	16.19
JaSolar	17.00

Table 6 : Multicrystalline Silicon Cells Efficiency Available in the Market

Thin Films Solar Cells

Thin film technology is becoming very attractive especially for its potential in lighter than air applications, since the materials can be deposited on lightweight flexible substrates and they can be more resistant to radiation than crystalline silicon. However the efficiency obtained from these devices is generally low as shown in Table 7 for the three most widely employed materials, i.e. amorphous silicon, Cadmium Telluride and Copper Indium (Gallium) Selenide.

Material	Efficiency [%]
A-Silicon	10.1
CdTe	16.7
CIGS	19.4

Table 7 : Thin Films Efficiency obtained at NREL Laboratory

As in the case of silicon cells the efficiencies available in the market for thin films are lower than the ones in Table 7. Moreover silicon cells are typically produced starting from a single ingot that is sliced to obtain very thin slices (wafers), which constitute the base for the manufacturing of a single cell. On the other hand thin films materials are deposited on the substrate to obtain directly the solar module rather than the single cell as in the case of the crystalline silicon. Data available in the market are therefore relative to the manufactured module. Some examples of the efficiencies commercially available are presented in Table 8.

Material	Efficiency [%]
Sharp (A-Silicon)	8.00
Calyxo (CdTe)	9.00
SoloPower (CIGS)	11.00

Table 8 : Thin Films Efficiency for Modules Available in the Market

Multijunction Solar Cells

A particular category of solar cells is constituted by the multijunction devices, which employ layers of different materials in order to optimize the conversion of the solar radiation into electrical power, each layer being capable of converting a specific part of the solar spectrum. The efficiencies that can be obtained in research laboratories are therefore very high, reaching values of 32% in the case of GaInP/GaAs/Ge [112]. This type of solar cells is mainly used for space applications, as they are very expensive and the devices available in the market can reach efficiencies comparable with the laboratory ones (Table 9).

Material	Efficiency [%]
NREL Laboratory	32.00
Emcore	28.5
Spectrolab	29.9

Table 9 : GaInP/GaAs/Ge Solar Cells Efficiency

Specific Power Comparison

A particular figure that needs to be considered during the AEPG design is the mass that the different types of solar cells can have. At the cell level, multijunction devices have a larger mass, as they are constituted by multiple layers, while thin films can be generally much lighter. Mass usually constitutes a parameter of primary importance only when dealing with space applications, while it becomes less relevant in the design of terrestrial systems. Therefore commercially available data which refer to the manufactured module to be employed in ground based systems are not expected to be significant for this study, as they are not optimized in terms of reduced mass. On the other hand useful information about this figure that can be found in literature mainly concerns space systems, where the mass is one of the main design drivers to be taken into consideration and it is quantified with the specific power parameter [W/kg]. The figures provided are generally relative to the solar module, including the contribution of the solar panel substrate which can be very different for different PV technologies. Similar substrates might be included in the design of the solar array of the AEPG depending on the technical solution chosen. Therefore the information found in literature can be useful to determine the preliminary values to be used in the present exploratory calculations even though a revision of these figures is needed in the following phases of the research.

The study presented in [113] considers the comparison between different technologies, i.e. crystalline silicon, thin films and mulitjunction cells for the design of an array for space applications. The array design includes a rigid substrate, in the case of silicon and multijunction cells, constituted by a sandwich panel with honeycomb core (aluminium) between two fibre reinforced composite sheets. On the other hand, in the case of thin film technology the array considered includes a flexible lightweight composite substrate. Moreover the state of the art analysis provided in [13] compares the different technologies in order to assess their potential for space solar power applications. Specific figures obtained from these analysis are between 70 W/kg and 100 W/kg for multijunction and silicon cells arrays, while projected values for thin film PV arrays (CIGS) are expected to reach 600 W/kg. Other studies are exploring the possibility of depositing CIGS on stainless steel, titanium and polyimide in order to obtain a specific power of up to 1500 W/kg [114]. This stresses the potential of this technology to effectively reduce the array mass although data available are generally relative to ongoing research projects or they refer to future projected values. The efficiency and specific power figures assumed in the present study are summarised in Table 10.

Cell Type	Efficiency [%]	Specific Power [W/kg]
Thin Films	10	500
Crystalline Silicon	20	100
MultiJunction	30	70

Table 10 : Efficiency and Specific Power assumed in the Present Study

5.3.2 PV Array Sizing

The first payload component to be assessed is the PV array, whose size and weight is related to the characteristics of the balloon as well as to the performance of the solar cells chosen. First of all the value of the power installed depends on the amount of envelope surface available and on the efficiency of the solar cells.

The AEPG concept has been previously introduced in its simplest representation and the layout of the PV array presented. The cells are assumed to cover a part of the external envelope, all pointing in the same direction. It is important to set a value for the amount of surface that will be covered by the PV cells in order to define the peak power that can be installed. A reasonable value can be set to the 75% of the projected surface of the balloon, which corresponds to an angle of 60˚ between the external edge of the array and the horizontal (Figure 35, the curvature of the spherical cap is assumed not to affect the power production of the solar cells).

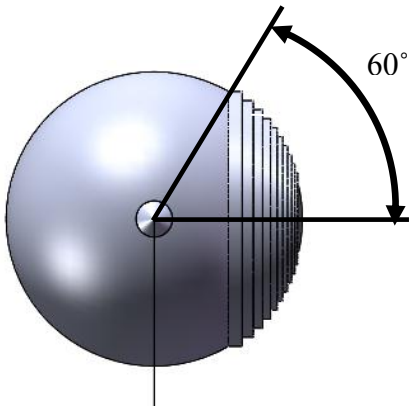

Figure 35 : Angle of the PV array cladding

Under these assumptions, Figure 36 shows the peak power that can be installed considering different types of solar cells (thin films at 10% efficiency, silicon at 20% efficiency and multijunctions at 30% efficiency), varying the diameter of the balloon. The peak power is estimated under the following standard conditions:

- Irradiance at 100 mW/cm^2
- Standard reference AM1.5 spectrum
- Temperature 25˚C

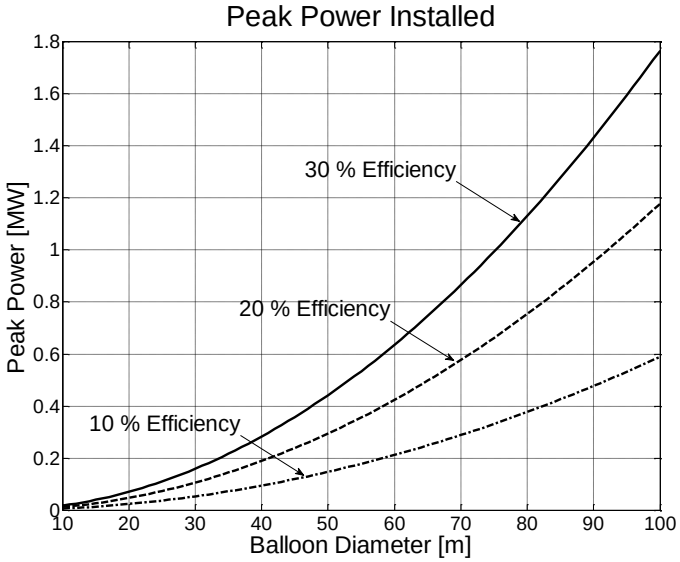

Figure 36 : Peak Power installed for different diameters and solar cells efficiencies

Starting from Figure 36, the balloon diameter can be determined, depending on the peak power value and on the efficiency of the solar cells (i.e. the solar cell type). The values obtained for peak power values of 100 kWp, 500 kWp, 1 MWp and 1.5 MWp are summarised in Table 11.

Peak Power [MWp]	Thin Films	Crystalline Silicon	Multijunction
0.1	41 m	29 m	24 m
0.5	92 m	65 m	53 m
1	130 m	92 m	75 m
1.5	160 m	113 m	92 m

Table 11 : Balloon diameter for different values of peak power

It can be noticed that, on the base of the assumptions described above (maximum balloon diameter of 100 m), some solar cells types can be excluded for higher values of the power installed (highlighted in red in Table 11).

For the same peak power values, the mass of the PV array can be calculated starting from the specific power determined in section 5.3.1 for different PV technologies. For this preliminary study, specific power values are set to 70 W/kg and 100 W/kg for silicon and multijunction cells while a slightly more conservative estimate of 500 W/kg is assumed for thin films, due to the fact that the data presented concern more research projects rather than devices available in the market. In addition to the solar cells mass, the contribution of the various collector grid components (cables,…) must be evaluated. This contribution is estimated as 30% of the total mass of the solar cells [31] and it is included in the evaluation of the PV system weight.

Having determined the balloon diameter necessary to install a defined level of peak power and setting the operational altitude to 6000 m, the disposable lift can be evaluated as described in section 5.2. The weight of the PV system is then compared to the corresponding value of disposable lift and the results obtained are presented in Table 12. These figures can provide a first idea of the most suitable technology to be employed for different values of the peak power installed.

Peak Power [MWp]	Thin Films	Crystalline Silicon	Multijunction
0.1	1.5 %	23.6 %	63.8 %
0.5	0.6 %	8.9 %	24.1 %
1		6.1 %	16.3 %
1.5			13 %

Table 12 : PV array weight as percentage of the disposable lift

5.4 Power Transmission Components

The following sections introduce the components responsible for the transmission of the power to the ground. These include not only the conductor component of the mooring tether, but also some additional devices introduced to reduce possible losses and maximize the amount of power delivered.

5.4.1 Conductor Tether

The peak power installed is strongly related to the size of the spherical balloon as described in the previous section. Furthermore this figure also has a significant influence on the characteristics of the conductor tether, in particular on the section area

required to limit the transmission losses, which is used to determine its total weight value for a given length. This section introduces some simplified calculations to size the conductor tether, given the amount of power to transmit and setting a limit for the ohmic losses. Technical issues concerning the possibility and convenience of employing DC or AC (single phase or three phases) current and voltage are not taken into account for the moment as the detailed design of the transmission line is beyond the scope of this preliminary study. Nevertheless it is important to point out in this early phase of the study that the power transmission is a crucial issue for the feasibility of the system.

The power P_{PV} generated at high altitude that needs to be transmitted to the ground can be expressed as:

$$P_{PV} = V_{TR} \cdot I_{TR} \tag{5.10}$$

Where V_{TR} and I_{TR} are the transmission voltage [V] and current [A]. The ohmic losses (P_{LOSS}) along the tether are related to the resistance (R_{Cond} [Ω]) and the intensity of the electrical current as:

$$P_{LOSS} = R_{Cond} I_{TR}^2 \tag{5.11}$$

Assuming a value for the transmission efficiency η_{TR}, defined as:

$$\eta_{TR} = \frac{P_{LOSS}}{P_{PV}} \tag{5.12}$$

and considering the relation between resistance and conductor characteristics (length len_{Cond}, section area A_{Cond} and material resistivity r_{Cond}):

$$R_{Cond} = \frac{r_{Cond} \cdot len_{Cond}}{A_{Cond}} \tag{5.13}$$

The conductor weight W_{Cond} can be determined as a function of r_{Cond}, len_{Cond}, P_{PV}, η_{TR}, V_{TR} and conductor material density ρ_{Cond}. Starting from:

$$W_{Cond} = A_{Cond} \cdot len_{Cond} \cdot \rho_{Cond} \cdot g \tag{5.14}$$

Eq. 5.13 can be introduced to define A_{Cond}

$$W_{Cond} = \frac{r_{Cond} \cdot len_{Cond}}{R_{Cond}} \cdot len_{Cond} \cdot \rho_{Cond} \cdot g \tag{5.15}$$

From Eq. 5.11:

$$W_{Cond} = \frac{r_{Cond} \cdot len_{Cond}^2}{\frac{P_{LOSS}}{I_{TR}^2}} \cdot \rho_{Cond} \cdot g \tag{5.16}$$

And introducing the definition of transmission efficiency in Eq. 5.12:

$$W_{Cond} = \frac{r_{Cond} \cdot len_{Cond}^2 \cdot P_{PV}}{\frac{\eta_{TR} P_{PV}^2}{I_{TR}^2}} \cdot \rho_{Cond} \cdot g \tag{5.17}$$

Finally from equation 5.10, the weight of the conductor can be determined as:

$$W_{Cond} = \frac{r_{Cond} \cdot len_{Cond}^2 \cdot P_{PV}}{\eta_{TR} \cdot V_{TR}^2} \cdot \rho_{Cond} \cdot g \tag{5.18}$$

where ρ_{Cond} [kg/m^3] is the conductor material density and the conductor length is defined as double the length of the tether

$$len_{Cond} = 2 \cdot len_{init}^{tether} \tag{5.19}$$

to take into account for the closed circuit.

The material selected for the power transmission must have particular characteristics, in order to be able to significantly reduce the losses and at the same time keep the weight value to a minimum. As a trade off between these two properties, the material selected for the conductor is aluminium with a resistivity r_{Al} of 2.82e-8 Ωm and a density ρ_{Al} of 2700 kg/m^3, while the losses along the tether can be set to a value of 5% of the power generated. Having defined these parameters, the weight of the conductor is directly proportional to len_{Cond}^2 and P_{PV}, while it is inversely proportional to V_{TR}^2. The value set for the transmission voltage is therefore extremely important and deserves particular consideration. First of all an upper limit must be defined in order to avoid different electrical problems, such as a possible breakdown of the circuit due to the arcing between the terminals at high altitudes. Moreover the weight of additional components (necessary to step up the voltage and optimize the power transmission) must be assessed to find a trade off between the advantage deriving from the increased voltage and the drawbacks due to the introduction of these components.

General considerations about the voltages that can be achieved before an electrical breakdown occurs can be inferred analysing the Paschen curve [115] in the case of two electrodes at different voltage levels separated by a defined gap for different atmospheric pressure values. The curve provides the breakdown characteristics of a gap as a function of the product of the gas pressure and the gap length (Figure 37).

Considering an altitude of 6000 m (about 350 mmHg in Figure 37) the breakdown voltage value is about 10 kV for a gap of 1 cm between two conductors.

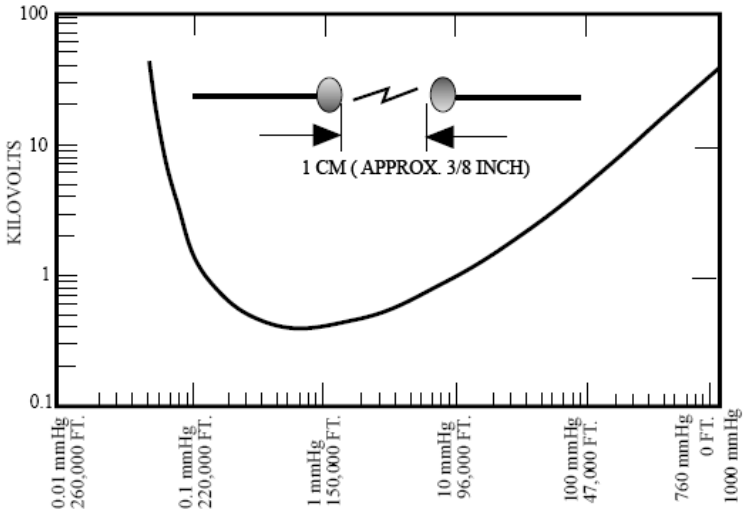

Figure 37 : Paschen Curve

In the case of the AEPG, the transmission lines terminals are not expected to be separated by a 1 cm gap of air and the values obtained are therefore quite conservative for an electrical breakdown. However other problems (like corona discharge for example) can occur at lower voltages, especially when the humidity is considerable, which might be the case of the environment experienced by the AEPG at high altitudes. These problems can significantly affect the power transmission efficiency.

Considering the configurations presented in Table 11 and Table 12, the weight of the conductor tether can be determined and compared with the disposable lift for different transmission voltage values (Table 13 for 1 kV voltage, Table 14 for 10 kV voltage).

Peak Power [MWp]	Thin Films	Crystalline Silicon	Multijunction
0.1	128.9 %	398.4 %	753.0 %
0.5	51.2 %	150.3 %	285.1 %
1		102.4 %	192.6 %
1.5			153.6 %

Table 13 : Ratio between the tether weight and the disposable lift for a voltage of 1 kV

Peak Power [MWp]	Thin Films	Crystalline Silicon	Multijunction
0.1	1.3 %	4.0 %	7.5 %
0.5	0.5 %	1.5 %	2.8 %
1		1.0 %	1.9 %
1.5			1.5 %

Table 14 : Ratio between the tether weight and the disposable lift for a voltage of 10 kV

It is interesting to notice that for a transmission voltage of 1000 V, which is commonly considered the maximum DC value that can be obtained from a PV array, the configuration presented are generally not feasible, since the weight of the conductor

becomes higher than the disposable lift. The ratio between the disposable lift and the conductor tether weight quickly decreases as the voltage value is incremented to 10 kV (conductor tether 100 times lighter). However in order to be able to step up the transmission voltage to values higher than 1 kV, it is necessary to introduce some additional components, which are typically employed in ground based PV systems, such as an inverter to convert the direct current to alternating and a transformer to step up the voltage to a value suitable for transmission. Therefore it is important to investigate the possible effect that the introduction of these components can have on the system (in particular on the overall weight).

5.4.2 Inverter and Transformer

Inverters are electrical devices capable of converting the direct current produced by the PV modules into alternating current which is generally used for transmission. In addition, the PV inverter can usually provide the maximum power point tracking necessary to adjust the current and voltage levels in order to optimize the power generation. The following analysis is focused on components available in the market with power ratings between 100 kW and 1 MW, which are mainly employed in large photovoltaic installations connected to the electric grid. The main interest is the determination of the mass of these devices as a function of their power rating. The values presented in Figure 38 are relative to the PowerGate Plus series manufactured by Satcon which can provide efficiencies between 95% and 97%.

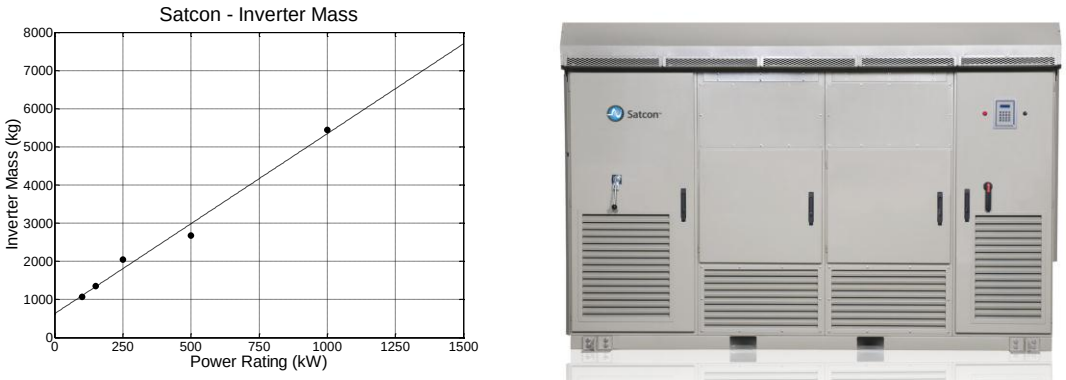

Figure 38 : Satcon PowerGate Plus Series Mass

As in the case of the solar cells and conductor tether, the weight of the inverter is compared to the value of the disposable lift for the peak power considered (Table 15). The AC current coming from the inverter unit is fed into a transformer capable of increasing the voltage to the level selected in section 5.4.1.

Peak Power [MWp]	Thin Films	Crystalline Silicon	Multijunction
0.1	6.5 %	20 %	37.8 %
0.5	1.4 %	4.1 %	7.8 %
1		2.5 %	4.7 %
1.5			3.6 %

Table 15 : Ratio between the inverter weight and the disposable lift

Transformers have a huge variety of applications from electronics to power transmission. The assessment of the possible values of mass of this device is performed considering transformers mainly used for industrial power distribution purposes, which can be dry type or oil filled (Figure 39), with power ratings up to 2500 kVA and high voltage values up to 36 kV [116]. Efficiency values are quite high, ranging between 98% and 99%.

Figure 39 : Dry Type and Oil Filled Distribution Transformers

For applications in harsh environmental conditions, where the decrease in temperature and atmospheric density can cause problems to the thermal control of the system affecting its performance, dry type transformers are generally preferred. As an example the ABB Resibloc [117] is tested at temperatures as low as -60˚C which is compatible with the temperature range expected for the AEPG, even though the supplier recommends that an operational altitude of 1000 m above sea level is not exceeded without special modifications to the design. This transformer can step up the voltage from 400 V to 10 kV with power ratings up to 3150 kVA. Focusing on power levels from 250 kVA to 1600 kVA, the mass varies linearly from 1440 kg to 4800 kg as presented in Figure 40.

The figures obtained for the comparison between transformer weight and the disposable lift are presented in Table 16.

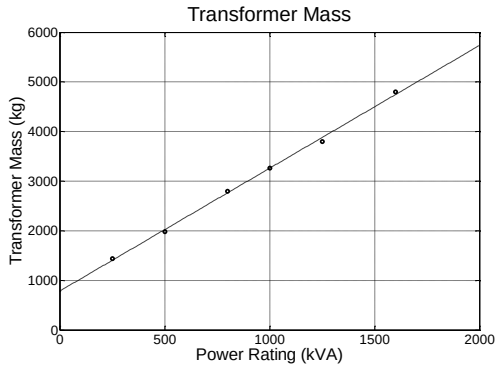

Figure 40 : ABB-Resibloc Transformer Mass

Peak Power [MWp]	Thin Films	Crystalline Silicon	Multijunction
0.1	6.2 %	19.1 %	36.1 %
0.5	1 %	2.7 %	5.2 %
1		1.5 %	2.9 %
1.5			2.1 %

Table 16 : Ratio between the transformer weight and the disposable lift

It must be pointed out that the analysis presented concerns inverters and transformers available in the market, which are generally employed in large PV plants where the power transmission is performed using three phase current and voltage. On the other hand the preliminary sizing of the conductor tether in section 5.4.1 considers two lines for the electric circuit, i.e. DC or AC single phase power transmission. The possibility of customizing the various components in order to optimize the characteristics of the system is beyond the scope of this feasibility study. Nevertheless the data presented can provide a first idea of the mass contribution of these devices to the total budget. The results obtained can be used to demonstrate the advantages deriving from the increase in transmission voltage compared to the possible drawback due to the payload weight penalty that the introduction of these additional components implies. The advantage appears evident from the comparison of the figures in Table 13-Table 16.

5.5 Free Lift and Additional Subsystems

The preliminary considerations presented have been focused on the disposable lift available for different values of balloon diameter and on the parameters describing the main subsystem i.e. the PV array and the power transmission components. The reason for this choice is that these variables are considered as the design drivers and the starting point for the successive design of the generator. However even in this very early phase of the design process it is important to take into account for the possible presence of the other components, which for the moment will be referred to as secondary subsystems. In particular it is necessary to consider the possible contribution deriving

from the employment of different structural components, such as the supporting frame for the solar cells (whose contribution is only estimated in the specific power value). Moreover the subsystem which would be used to perform the tracking of the sun, the buoyancy regulator and various electronic components are expected to represent a significant portion of the total weight. In addition to that, the weight of the composite part of the tether, which will carry the mechanical loads, has to be evaluated, as it depends on the aerodynamic forces acting on the system. This will be evaluated in the following section where the aerodynamic loads are introduced. Finally, it is important to take into account in the weight budget of the system a significant amount of free lift, which is defined as:

$$L_{Free} = B - W_{Gas} - W_{Env} - W_{P/L} - W_{Tether} \tag{5.20}$$

The value of this parameter should be around the 30% of the buoyancy [87], to allow the balloon to overcome the loads induced by the environmental conditions during ascent and normal operations.

Including the contributions of inverter and transformer and taking into account the free lift in the weight calculations, the amount of lift available for the remaining subsystems can be determined. The results are listed in Table 17, which presents the comparison between the lift available for the secondary subsystems and the disposable lift for the configurations assumed in section 5.3.

Considering these figures it is possible to exclude some configurations (highlighted in red) from further analysis based on the small amount of lift available. The remaining configurations constitute a set of possible technical solutions based on different PV technologies which will be assessed in section 6 developing a simplified mathematical model of the tethered balloon.

Peak Power [MWp]	Thin Films	Crystalline Silicon	Multijunction
0.1	42.5 %	0 %	0 %
0.5	58.9 %	43.7 %	19.9 %
1		51.2 %	35.8 %
1.5			42 %

Table 17 : Ratio between Lift Available for the Secondary Subsystems and Disposable Lift

6 STEADY STATE ANALYSIS

The previous chapter has presented some considerations that have been used to identify a set of possible configurations potentially suitable for the development of the AEPG. The present assessment aims to compare these solutions based on a steady state model and to the definition of a baseline configuration which will be the starting point for the concept design of the system.

The analysis of the different options is based on the results obtained from a simplified mathematical model of the system, presented in Sec.6.1, which provides the equilibrium cable profile when subjected to a mean wind profile (i.e. the steady state in 2D) and the main characteristics of the system in terms of weights of the different components. The assessment is then carried out with the analysis of the main output parameters, i.e. final position of the balloon, shape of the tether, aerodynamic loads and cable tension. Once the baseline configuration is defined, a sensitivity analysis to evaluate the influence of the design parameters on the final performance of the system is performed.

6.1 Steady State Model Description

The model presented in this section considers the simplified case of a LTA tethered spherical balloon subjected to a steady wind speed profile at different heights above the ground. The calculations are used to quantify the influence that the main parameters involved in the preliminary design phase can have on the performance of the system. The input parameters include the definition of the steady state atmospheric conditions in which the system is due to operate (determined in section 3.1 and 3.2) and the most important properties of the various components.

The calculations performed by the model are used to determine the maximum altitude reached by the balloon (where the envelope is assumed fully inflated), its horizontal displacement and the final shape of the tether in equilibrium conditions for a given set of input parameters. Additional output values include:

- Aerodynamic forces on the balloon and tether
- Tension force and stress along the tether

The procedure is here described, and the main equations implemented in the model are introduced. Similar procedures have already been employed in analogous analysis like the ones presented in [118] and [119]. The calculations are here adapted to the conditions assumed for the present study.

The tether length from the balloon to the ground is discretized into a defined number of segments and nodes, the first node representing the balloon while the last one corresponding to the ground station. For each node the forces along the tether and the angle of inclination are calculated considering the conditions of equilibrium. Starting from the first node, the position of each of the following nodes can be determined iteratively. Figure 41 shows the discretization of the system and the reference frame used during the calculations. Focusing on Node 1 (Figure 42), the forces involved in the determination of the tether tension are the buoyancy B [N] that needs to overcome the weight of the lifting gas W_{Gas} [N], envelope W_{Env} [N] and payload $W_{P/L}$ [N], and the aerodynamic drag on the balloon D_B [N]. The parameters that influence the weight of the payload $W_{P/L}$ [N] have preliminary been discussed in section 5 and they will be further discussed more in depth in the section 8.

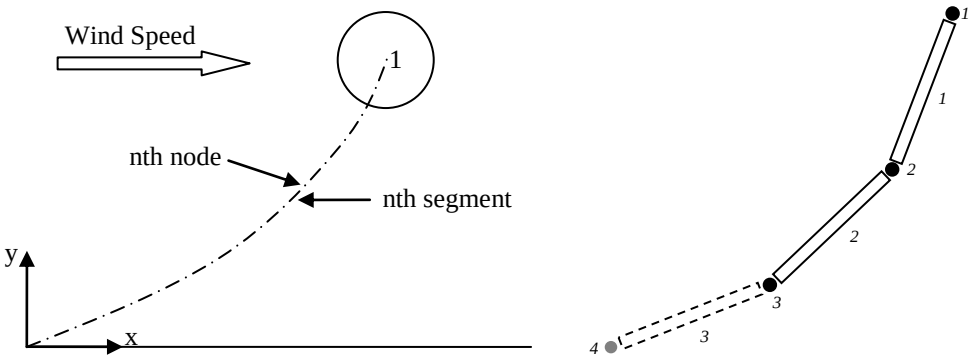

Figure 41 : Tether Discretization

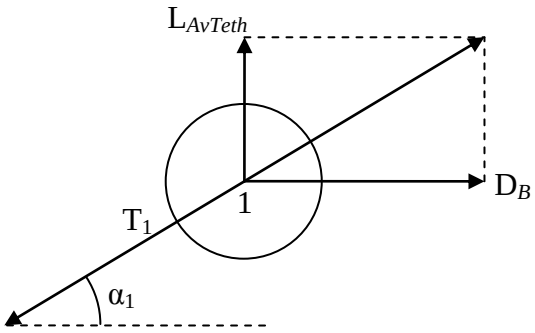

Figure 42 : Node 1 (Balloon)

Having determined the atmospheric conditions (wind speed and atmospheric density) at operational altitude, the drag force [N] on the balloon can be calculated as:

$$D_B = \frac{1}{2}\rho_{Air} V_{Wind}^2 C_D^B \frac{\phi_B^2}{4}\pi \tag{6.1}$$

where C_D^B is the drag coefficient of the balloon. This parameter is highly dependent on the value of the Reynolds number, related to the real shape of the body and to the atmospheric characteristics in which the system is operating. However for the moment a preliminary value of 0.2 [120] is assumed for the calculations presented.

For Node 1 (Figure 42), Newton's second law in equilibrium conditions becomes:

$$T_1 = \sqrt{(L_{AvTeth}^2 + D_B^2)} \tag{6.2}$$

where:

$$L_{AvTeth} = B - W_{Gas} - W_{Env} - W_{P/L}\,. \tag{6.3}$$

The angle between T_1 and the horizontal can be determined as:

$$\alpha_1 = \tan^{-1}\left(\frac{L_{AvTeth}}{D_B}\right) \tag{6.4}$$

which represents the inclination of the first segment of the tether respect to the horizontal.

Considering the first tether segment, as a result of the tension T_1 applied, the new length can be determined as:

$$len_1^{segm} = \frac{T_1}{k_{segm}} + len_{init}^{segm}\,. \tag{6.5}$$

The stiffness k_{segm} [N/m] of the segment is given by:

$$k_{segm} = \frac{E_{Comp} \cdot A_{Comp}}{len_{init}^{segm}} \tag{6.6}$$

A_{Comp} is the composite cross section (with Young modulus E_{Comp}) of the tether which is assumed to carry all the load along the cable. As a conservative assumption, the part of the section of the tether responsible of transmitting the power to the ground A_{Cond} does not carry any load.

The tension T_1 is the maximum expected along the tether, and it can therefore be used to size A_{Comp}, knowing the mechanical properties of the composite (composite ultimate stress σ_{Comp}^{Ult}) and having set the safety factor SF_{Comp} (set to a value of 3 for further calculations):

$$A_{Comp} = SF_{Comp}\frac{T_1}{\sigma_{Comp}^{Ult}}\,. \tag{6.7}$$

For these preliminary calculations, Kevlar fibres are assumed for the properties of the composite in the mooring tether, which will carry the mechanical loads. The values in Table 18 are chosen to define density, Young modulus, ultimate stress of the material and safety factor.

Composite Density	1450 kg/m^3
Composite Young Mod	83000 MPa
Composite Ult Stress	3620 MPa
Safety Factor	3

Table 18 : Kevlar Composite cable properties

The coordinates of the following node can be calculated as:

$$x_2 = x_1 - len_1^{segm}\cos(\alpha_1) \tag{6.8}$$

$$y_2 = y_1 - len_1^{segm}\sin(\alpha_1) \tag{6.9}$$

The inclination angle α_1 and the length of the tether segment len_1^{segm} are used to determine the drag and lift forces acting on it. The drag and lift coefficients for the first tether segment depend on the inclination angle, as derived in [118]:

$$C_D^1 = 0.02 + 1.1\cdot\sin^3(\alpha_1) \tag{6.10}$$

$$C_L^1 = 1.1\cdot\cos(\alpha_1)\cdot\sin^2(\alpha_1) \tag{6.11}$$

The resulting drag and lift forces on the segment can be calculated as:

$$D_1 = \frac{1}{2}\rho_{Air}V_{Wind}^2 C_D^1 len_1^{segm} d_{teth} \tag{6.12}$$

$$L_1 = \frac{1}{2}\rho_{Air}V_{Wind}^2 C_L^1 len_1^{segm} d_{teth} \tag{6.13}$$

In the determination of the diameter of the tether (d_{teth}), it is necessary to consider the section of the composite that carries the load as well as the section of the conductor used to transmit the power to the ground, which is sized on the base of electrical considerations as described in section 5.4.1. The total cross section of the tether is determined as:

$$A_{Teth} = A_{Comp} + 2\cdot A_{Cond} \tag{6.14}$$

where the factor 2 indicates the presence of two conductors in the tether, as a closed electrical circuit is necessary to transmit the power to the ground. The diameter of the tether can be defined for the moment as:

$$d_{Teth} = 2\sqrt{\frac{A_{Teth}}{\pi}} \tag{6.15}$$

It must be pointed out that this assumption is extremely simplified and that the actual internal composition of the tether needs to be revised later on in the design process. The aerodynamic forces and the weight of the tether segment are assumed acting on the following node and they can therefore be introduced in the equation of equilibrium to calculate the components of T_2 and the inclination angle α_2:

$$T_2^x = T_1 \cos(\alpha_1) + D_1 \tag{6.16}$$

$$T_2^y = T_1 \sin(\alpha_1) - L_1 - W_1^{segm} \tag{6.17}$$

$$\alpha_2 = a\tan\left(\frac{T_2^y}{T_2^x}\right) \tag{6.18}$$

The calculations presented in the equations above can be performed for each node, starting from the position of the balloon which is assumed as initial condition:

$$x_B = 0 \tag{6.19}$$

$$y_B = len_{init}^{tether} \tag{6.20}$$

where len_{init}^{tether} is the initial length of the tether. Finally, the position of each node needs to be translated in order to make the final node coincide with the origin of the reference frame on the ground, leading to the determination of the tether shape in equilibrium conditions.

The position of the balloon obtained after the first iteration is used to define the new initial condition for the calculations. The procedure described above is implemented in Matlab® code and then iterated until the shape of the tether converges to a final configuration. It must be pointed out that the tether length is divided into 500 segments and this value is kept constant for all the calculations presented. The choice of this figure is due to considerations about the convergence of the result, which has been assessed for different numbers of segments, showing negligible variations when more than 500 segments are considered (see Appendix C).

6.2 Baseline Configuration Definition

Some preliminary considerations about the weight of PV system, power conditioning and transmission components have been inferred in section 5, comparing the figures obtained from the sizing of solar cells, inverter, transformer and transmission line to the respective amount of disposable lift. This section evaluates the additional results

determined with the steady state model and adds some conclusions about the different solutions proposed. The characteristics of the possible configurations previously obtained are summarised in Table 19.

	1	***2***	***3***	***4***	***5***	***6***
Balloon Diameter [m]	41	92	65	92	75	92
Power Peak [MWp]	0.1	0.5		1		1.5
Solar Cells Type	Thin Films		Crystalline Si		Multijunction	

Table 19 : Configurations assumed for Steady State Analysis

The following output parameters are examined:

- Final Position of the Balloon when the system is subjected to the mean wind speed profile obtained from the Capel Dewi data.
- Composite Tether Weight
- Weight Breakdown

Starting from the final position of the balloon and shape of the tether, the results are presented in Figure 43, Figure 44 and Table 20. In particular Figure 44 shows the variation of the vertical and horizontal balloon displacements as a function of the sphere diameter.

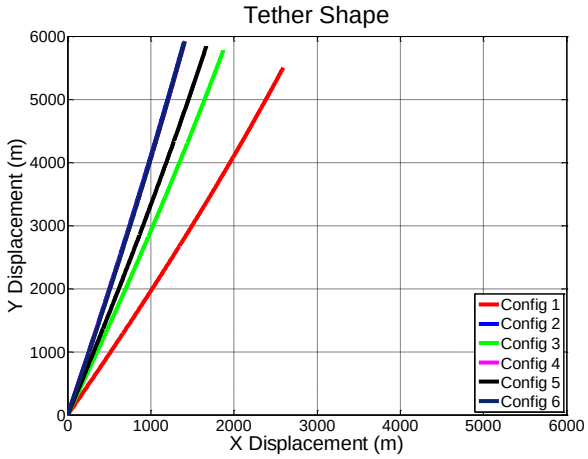

Figure 43 : Tether Shape for Configurations under Analysis

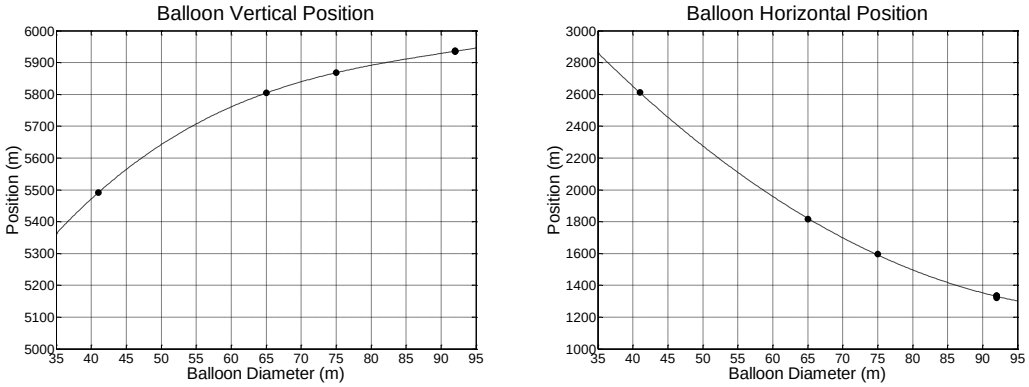

Figure 44 : Balloon Vertical and Horizontal Position as a function of the Balloon Diameter

	1	***2***	***3***	***4***	***5***	***6***
X Balloon Final [m] - Horizontal	2,612.2	1,334.0	1,816.0	1,335.9	1,597.0	1,320.4
Y Balloon Final [m] - Altitude	5,491.3	5,935.2	5,804.3	5,934.2	5,868.1	5,937.1
Min Inclination Angle [deg]	62.0	76.3	70.8	76.2	73.1	76.2

Table 20 : Final Balloon Position and Minimum Tether Angle

Larger diameters correspond to higher altitudes and smaller values of the horizontal displacement, since the buoyancy value is proportional to the volume of the balloon (i.e. ϕ_B^3). On the other hand the influence of the aerodynamic drag, which would tend to increase the horizontal displacement when larger diameters are considered (proportionally to ϕ_B^2), is less significant when compared to the buoyancy. Moreover the effect of the power installed, which would affect the PV system weight and that of the transmission components (inverter, transformer and conductor tether) is limited, probably due to the fact that the amount of free lift is set to a fixed value of 30% of the buoyancy. This is particularly evident when comparing configurations 2, 4 and 6, for which the equilibrium shape of the tether is almost coincident. These configurations have the same diameter (92 m) but employ three different PV technologies, with three different values of the power installed (0.5 MWp, 1 MWp and 1.5 MWp).

Overall the variation of the final horizontal position of the balloon is limited between 1,000 m and 2,000 m with the only exception of configuration 1 where the value of the horizontal displacement becomes more relevant. The balloon final height is always around 5,500 m or above and it is not expected to affect the amount of radiation that can be collected.

The second parameter which is important to look at is the maximum tether tension which is used to size the composite section to withstand the mechanical load. This force corresponds to the node attached to the balloon and it decreases going from the balloon to the mooring point. As a consequence an optimized design, in terms of minimized weight, would require a decreasing section as points closer to the ground are considered. For the present purpose this possibility is not taken into account and the tether is assumed to have a constant section. Figure 45 shows the variation of the maximum force on the tether obtained for increasing values of the balloon diameter. It can be noticed that the balloon diameter plays an important role in the determination of this parameter as it influences both the buoyancy (proportional to ϕ_B^3) and the aerodynamic drag (proportional to ϕ_B^2) which contribute to the determination of the tether tension.

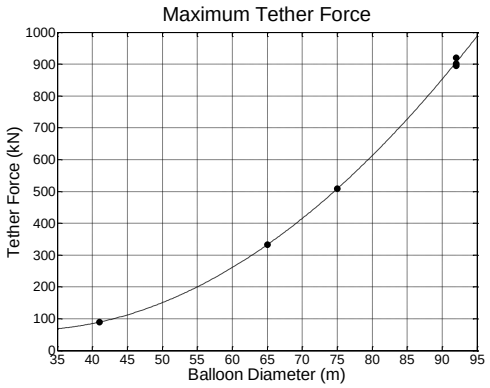

Figure 45 : Maximum Tether Force

Considering the weight breakdown presented in Table 21 (absolute values) and Table 22 (as a percentage of the disposable lift) some additional considerations about the weight contribution of each component can be inferred. The values presented are slightly different from the ones obtained in section 5, because the model considers the balloon fully inflated at final altitude, which is different from the 6000 m assumed during the preliminary considerations.

	1	***2***	***3***	***4***	***5***	***6***
Buoyancy	246.8	2,654.9	950.0	2,655.2	1,449.1	2,654.4
Gas	34.1	366.7	131.2	366.8	200.2	366.7
Envelope	34.4	173.3	86.5	173.3	115.2	173.3
Disp. Lift	178.3	2,114.9	732.3	2,115.1	1,133.8	2,114.4
PV Sys.	2.5	12.7	63.7	127.4	182.0	273.0
Inverter	10.8	29.4	29.4	52.4	52.4	75.5
Transf.	10.3	19.6	19.6	32.3	32.3	44.6
Cond. Tet.	2.1	10.7	10.7	21.5	21.5	32.2
Comp. Tet.	6.3	63.2	23.5	63.7	35.9	65.0
Sec. Subs	72.0	1,176.0	298.9	1,019.2	372.4	818.3
Free Lift	74.2	803.2	286.4	798.6	437.2	805.8

Table 21 : Weight Breakdown for Different Configurations (Absolute Values in [kN])

	1	***2***	***3***	***4***	***5***	***6***
Disp. Lift	100	100	100	100	100	100
PV Sys.	1.4	0.6	8.7	6.0	16.1	12.9
Inverter	6.0	1.4	4.0	2.5	4.6	3.6
Transf.	5.8	0.9	2.7	1.5	2.9	2.1
Cond. Tet.	1.2	0.5	1.5	1.0	1.9	1.5
Comp. Tet.	3.5	3.0	3.2	3.0	3.2	3.1
Sec. Subs	40.4	55.6	40.8	48.2	32.8	38.7
Free Lift	41.6	38.0	39.1	37.8	38.6	38.1

Table 22 : Weight Breakdown for Different Configurations (Percentage of Disposable Lift)

First of all it is interesting to compare the weight of the tether conductor part to the weight of the tether composite part. The composite weight varies according to the maximum tension force shown in Figure 45 and its contribution is around the 3% of the disposable lift for all the configurations. On the other hand the conductor weight varies from 0.5% to 1.9% of the disposable lift as it depends on the peak power installed. Moreover the composite contribution to the total tether weight is much more relevant than the conductor one, ranging from 62.5% (configuration 5) to 85.5% (configuration 2).

As mentioned in section 5.5 it is important to assess the amount of lift available for the secondary subsystems and for possible additional weight due to inaccuracies in the previous estimates. In particular it is necessary to include in the design the following principle components:

- Pointing mechanism
- Supporting frame for the solar cells
- Buoyancy regulator devices
- Structural Components
- Additional Electric Components

The weight of some of these components is expected to depend on the external surface of the balloon, i.e. it is expected to increase with ϕ_B^2. More specifically the pointing mechanism design drivers will be the inertial characteristics of the system, including total mass and ϕ_B^2. Furthermore the supporting frame for the solar cells, only partially considered in the specific power value, will be proportional to the frontal projected surface of the sphere, which again depends on ϕ_B^2 and the PV technology considered. On the other hand the buoyancy regulator, which includes the ballonet membrane and the pressurizing system, is expected to depend more on the volume of the gas contained in the envelope, and therefore its weight will presumably increase with ϕ_B^3.

On the base of the considerations presented, it is possible to skim some of the technical solutions and converge to a baseline configuration used in the following steps of the study.

First of all the results concerning the final position of the balloon would tend to exclude the configuration number 1, since the horizontal displacement would require a large amount of free area around the mooring point. On the contrary considering the weight of the payload it is more difficult to decide if this could constitute a showstopper in

some cases, even though for a given value of the power installed the lighter solution might be considered more viable. However, looking at the amount of free lift available for the secondary subsystems and considering in particular configurations 2-4-6 (95 m diameter) it can be noticed that smaller amounts of lift correspond to solutions employing heavier PV technologies. This might constitute a problem as heavier PV systems imply higher masses for the pointing mechanism and structural components. Moreover these configurations have very high value of tether composite weight compared to the conductor part.

In this sense, configurations 3 and 5 are a more balanced compromise. In particular configuration number 3 seems to constitute a reasonable starting point for the assessment of the technical feasibility of the AEPG due to its reduced size and to the employment of silicon solar cells, which are more extensively used and whose data are more widely available. Configuration number 3 will therefore be adopted as baseline configuration for the sensitivity analysis and the following dynamic analysis and concept design.

It must be pointed out that the chosen configuration is by no means definitive but it will be used to carry out the more accurate concept design of the different subsystems involved. General conclusions about the technical feasibility of the systems are expected to be still valid for the other configurations introduced in this section.

6.3 Pareto Analysis

In order to support the choice of the baseline configuration in section 6.2, a useful method to be employed is the Pareto analysis. This method allows an assessment of the different design solutions based on a comparison between cost and benefit. Different combinations of design parameters are assumed and for each combination, the cost and benefit figures are calculated.

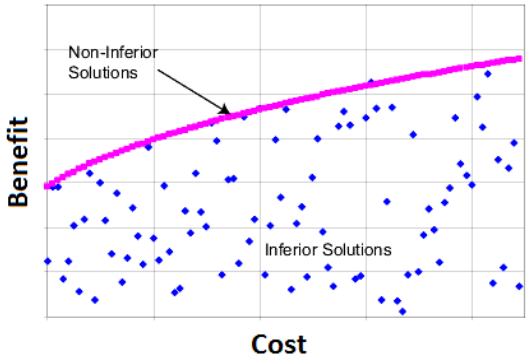

Figure 46 : Pareto Front constituted by non-inferior solutions

The values obtained are then compared in a plot, like the one presented in Figure 46, where a Pareto front can be identified. The Pareto front is constituted by non inferior design solutions. For these solutions, it is not possible to increase the benefit without increasing the cost at the same time. Therefore non inferior solutions are of particular interest to focus the following phases of the design.

In the case of the AEPG, the design parameters considered in this analysis (and relative variations) are:

- Balloon diameter: 30 m to 95 m
- Balloon drag coefficient: 0.2 to 1
- PV cells efficiency: 5% to 35%
- Tether length: 3000 m to 15000 m
- Secondary subsystems weight: 0% to 45% of the buoyancy value.

A preliminary cost model is derived from the one in [21] and data available from manufacturers. The first contribution to the total cost comes from the lifting gas. Considering Helium as the lifting gas, the cost is about about 6 $/m^3 at ground atmospheric pressure. Moreover the cost of the envelope fabric usually depends on the volume of the balloon. As a preliminary estimate the cost per square meter can vary from about 80$/m^2 for a 90 m^3 balloon to 345 $/m^2 for a large airship of about 700e3 m^3 [110]. As far as the PV cells are concerned the cost depends on the efficiency. Data available at [121] show that prices per Watt peak can range from 1.28$/W$_p$ for silicon mono-crystalline (at 20% efficiency) to 1.15$/W$_p$ for thin film (at 10% efficiency). Price data for multijunction solar cells (with efficiencies higher than 30%) are more difficult to find in literature and from manufacturers, as this type of solar cell is not usually employed for commercial applications. As a very preliminary estimate we can approximate the cost trend with the curve shown in Figure 47.

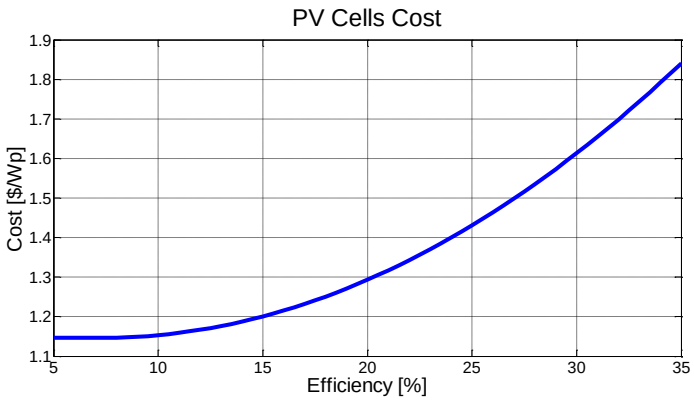

Figure 47 : PV cells cost as a function of the efficiency

Inverter and transformer prices can also be derived from the data available at [121] with a preliminary estimate set to 0.7 $/W.

As far as the mooring tether is concerned, the conductor part is assumed to be constituted by aluminium at 2$/kg while the Kevlar composite is estimated to have a cost of around 50$/kg.

The last factor to take into account when defining the cost parameter, is the weight of the secondary subsystems. As mentioned in section 6.2, the secondary subsystems include different components which contribute to the overall cost of the system as they increase the complexity of the AEPG. At this stage of the design it is difficult to provide an accurate estimate of the total cost of these components. On the other hand, it seems more reasonable to introduce in the cost estimate a multiplying factor ranging from 1 to 1.5 depending on the weight of the secondary subsystems.

As far as the system performance is concerned, this parameter is evaluated considering three different design drivers:

- Power production
- Free Lift
- Horizontal Displacement in equilibrium conditions

First of all, the power production is taken into account. This parameter depends on:

- Peak power installed.
- Advantage in terms of solar radiation collected, related to the operational altitude of the generator.
- Ability of the platform to collect the solar radiation, generate the electrical power and transmit it efficiently to the ground.

The advantage in terms of solar radiation collected is evaluated from the results obtained and presented in section 2. The ability of the platform to optimise the power production and transmission is assumed to depend on the secondary subsystems weight. In particular the pointing mechanism is expected to increase significantly the value of the power produced at high altitude when compared to the non-pointing option.

Considering the power production, the performance parameter is estimated as:

$$Perf_{Power} = P_{Installed} \cdot Gain \cdot F_{SecSubs} \tag{6.21}$$

with $F_{SecSubs}$ ranging from 1 to 2 depending on the secondary subsystems weight. The performance parameter is then normalised to 1 as:

$$\overline{Perf_{Power}} = \frac{Perf_{Power}}{\max(Perf_{Power})} \tag{6.22}$$

to compare the different designs.

The free lift parameter, necessary to withstand the aerodynamic loads during ascent, is evaluated as a percentage of the buoyancy setting the optimum value to 30%. The free lift performance parameter ($\overline{Perf_{FreeLift}}$) goes from 0 to 1 as the free lift of the corresponding design approaches this optimum value.

The horizontal displacement is normalised to 1 as in the case of the power produced as:

$$\overline{Perf_{HorDispl}} = \frac{\min(HorizDispl)}{HorizDispl} \tag{6.23}$$

where a performance parameter of 1 identifies the design with the minimum horizontal displacement in equilibrium conditions.

The overall performance parameter is calculated multiplying the three previous parameters by three different weights and summing their contributions:

$$Perf = W_{power}\overline{Perf_{power}} + W_{FreeLift}\overline{Perf_{FreeLift}} + W_{HorDispl}\overline{Perf_{HorDispl}} \tag{6.24}$$

For the moment, the power produced is considered the most important design parameter. As a consequence the three weights are assumed as:

$$\begin{aligned} W_{power} &= 0.8 \\ W_{FreeLift} &= 0.1 \\ W_{HorDispl} &= 0.1 \end{aligned} \tag{6.25}$$

The results obtained are presented in Figure 48 highlighting in red the six design solutions introduced in the previous section.

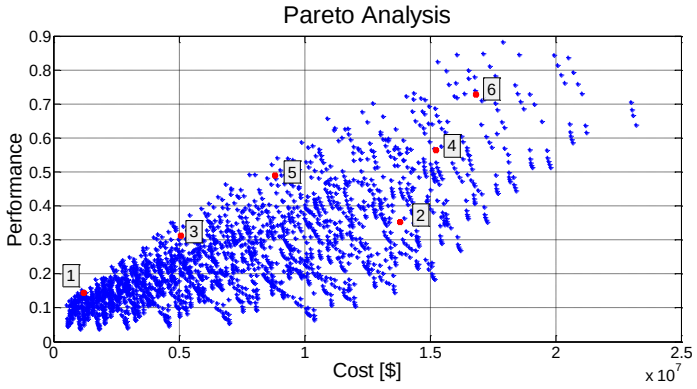

Figure 48 : Cost VS Performance - Pareto Analysis

Apart from solution 2 and 4, the solutions previously selected are quite close to the Pareto front.

6.4 Baseline Configuration Sensitivity Analysis

Before addressing the concept design of the generator, it can be useful to assess the sensitivity of the system to the variation of different design parameters in order to identify possible critical areas to investigate, in the very early phase of the project. This section presents a sensitivity analysis based on the steady state model introduced in section 6.1 which can be used to evaluate the influence of the different design parameters on the equilibrium configuration and on the performance of the system. The main parameters that identify the baseline configuration are summarised in Table 23. The results obtained from the steady state model, i.e. the final position of the balloon, the minimum tether inclination angle, and the maximum tether tension are presented in Table 24, while the weight breakdown is listed in Table 25.

In order to get a general idea of the influence of the single parameter on the final performance of the system, the variations of the following are taken into account:

- Balloon Diameter
- Envelope Weight
- PV System Weight
- Inverter and Transformer Weight
- Tether Weight
- Drag Coefficient
- Wind Speed Profile

The outputs considered for the assessment are:

- Balloon Final Position Variation
- Maximum Tether Force Variation
- Free Lift Variation

Balloon Diameter	65 m
System Power Peak	0.5 MWp
Solar Cells	Crystalline Silicon
Tether Length	6000 m
Transmission Voltage	10 kV
Inverter Mass	3000 kg
Transformer Mass	2000 kg
Transmission Losses	5 %
Balloon Drag Coeff	0.2
Conductor Tether	Aluminium
Composite Tether	Kevlar

Table 23 : Baseline Configuration Design Parameters

X Balloon Final	1816.0 m
Y Balloon Final	5804.3 m
Min Inclination Angle	70.8°
Max Tether Force	333.5 kN

Table 24 : Steady State Model Results

		% of the Buoyancy
Buoyancy	950.0 kN	-
Gas Weight	131.2 kN	13.8
Envelope Weight	86.5 kN	9.1
PV Array Weight	63.7 kN	6.7
Inverter Weight	29.4 kN	3.1
Transformer Weight	19.6 kN	2.1
Tether Conductor Weight	10.7 kN	1.1
Tether Composite Weight	23.5 kN	2.5
Secondary Subs Weight	298.9 kN	31.5
Free Lift	286.4 kN	30.2

Table 25 : Baseline Configuration Weight Breakdown

6.4.1 Balloon Diameter

Although the balloon diameter set for the baseline configuration is 65 m, it might be necessary to increase or decrease its value in the next phases of the study, depending on possible design constraints. It is therefore necessary to evaluate the effect that these variations can have on the system performance and to determine if they can represent a show stopper for its feasibility. The variation of this figure is expected to be limited, and a reasonable range is here set between 60 m and 70 m. As pointed out in section 6.2, an increment or reduction in the balloon diameter will have the combined effect of increasing or reducing both the buoyancy and the aerodynamic drag values. Moreover the variation of these two forces would have an opposite effect on the final position of the balloon. Higher buoyancy values would reduce the final horizontal displacement of the balloon while an increment in the aerodynamic drag force would lead to higher values for the same displacement. However the same variation in the balloon diameter affects more significantly the buoyancy value, being proportional to the third power of the balloon diameter, whose effect overcomes therefore the opposite effect that the aerodynamic drag would produce. Even with the small variation considered for the balloon diameter (about ±8% of the baseline value) the effect on the horizontal position can be quite significant, as shown in Figure 49. It must be pointed out that the

horizontal position of the balloon defines the amount of free area that is needed around the mooring point. This parameter has already been used as a design driver in past studies [87].

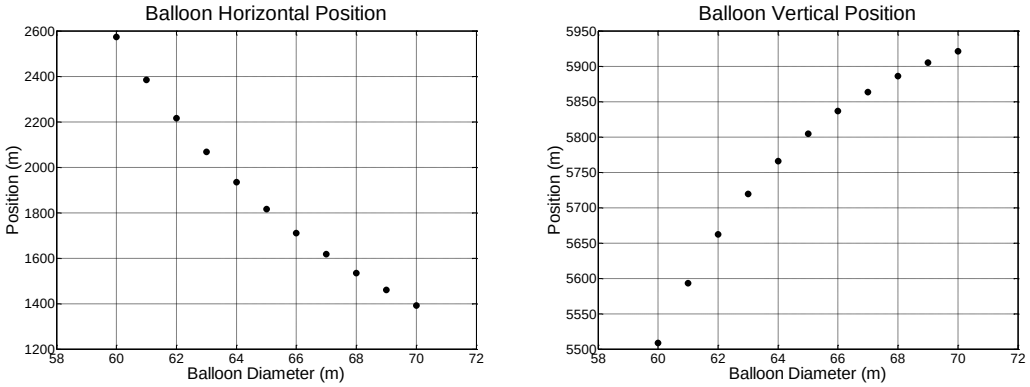

Figure 49 : Balloon Final Position as a function of the Balloon Diameter

The horizontal displacement is reduced to about the 75% of the baseline value (25% decrease) when a diameter of 70 m is considered, and increases its value by about 40% for the lowest size analysed. For what concerns the vertical position, the effect is less important and it is not expected to affect the amount of radiation collected.

Observing the results in Figure 50, it can be seen that the maximum force variation is comprised between -40% to +50% which is still within reasonable limits. On the other hand the free lift decreases to 20% of the buoyancy value for 60 m diameter balloon, which might be too low to effectively overcome the environmental conditions during the ascent. Another option in this case could be the introduction of additional temporary balloons for the ascent phase. However this solution would add a certain degree of complexity to the overall design.

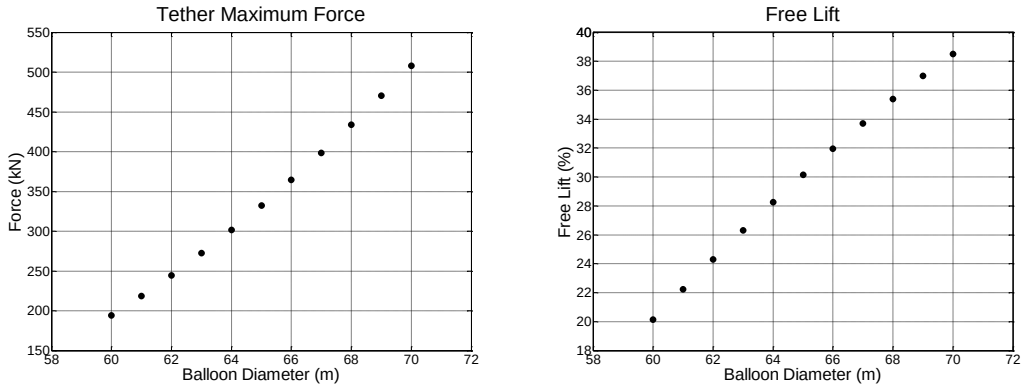

Figure 50 : Tether Maximum Force and Free Lift as a function of the Balloon Diameter

6.4.2 Envelope Weight

Keeping the balloon diameter fixed, the envelope weight can depend on different factors like the material chosen, the employment of various attachments and interface to the different subsystems and the presence of structural reinforcing components. In this sensitivity analysis the envelope weight evaluated as presented in the model description is assumed to vary between half and double the initial value. As in the case of the balloon diameter, the vertical position remains almost constant while the horizontal displacement is more affected, with variations between -10% and +23% of the base configurations (Figure 51).

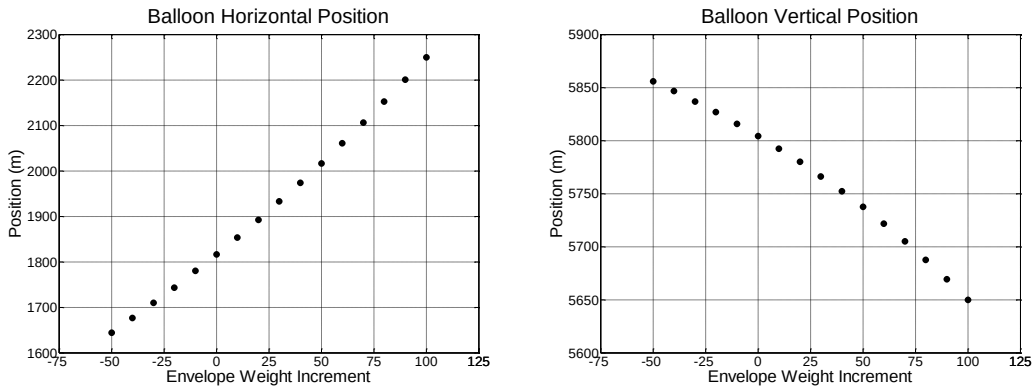

Figure 51 : Balloon Final Position as a function of the Envelope Weight

Figure 52 shows a quasi linear relation between the envelope weight multiplicative coefficient and the values of maximum tether force and free lift. For the baseline configuration a 50% decrease of the envelope weight leads to an increment of the 10% in the tether force while, doubling the envelope weight, the force is decreased of 20%. The corresponding values of the free lift range between 35% to 25% of the buoyancy, which are expected to be still acceptable for the system feasibility.

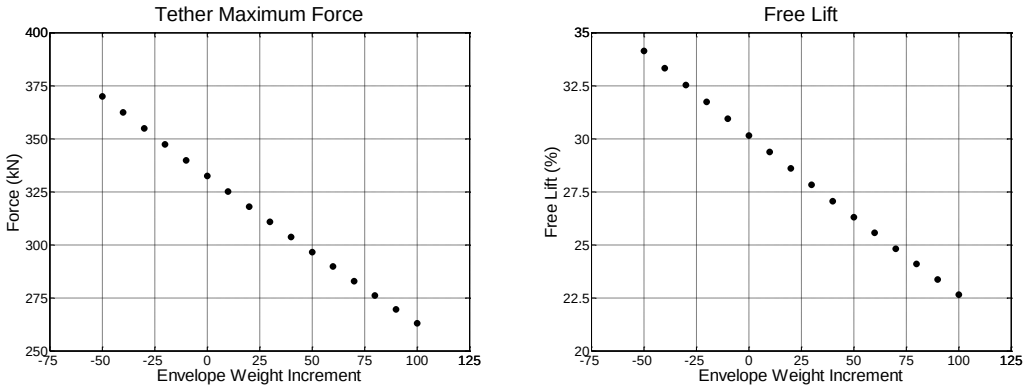

Figure 52 : Tether Maximum Force and Free Lift as a function of the Envelope Weight

6.4.3 Drag Coefficient

The balloon drag coefficient is set to 0.2 for the calculations of the steady state model. However it is necessary to add some considerations about its variability and to evaluate its influence on the final result. The balloon drag coefficient can be estimated starting from the investigation of the Reynolds number in which the system is due to operate. From the definition of Reynolds number:

$$\mathrm{Re} = \frac{\rho_{Air} \cdot V_{Wind} \cdot \phi_B}{\mu_{Air}} \tag{6.26}$$

where μ_{Air} [(N s)/m^2] is the viscosity of the air, it is possible to introduce the wind speed and atmospheric density profiles determined in section 3 and the diameter values considered for the baseline configuration, in order to estimate this parameter at different altitudes.

Figure 53 shows the Reynolds number profile that, for 6000 m of altitude, is in the supercritical regime (>3.5e5) ranging from a value of about 5.4e7, relative to the mean wind speed profile, to a maximum value of about 1.5e8. Figure 54 shows the drag coefficient for uniform flow over a sphere, experimentally determined by Schlichting [122], Achenbach [123] and Maxworthy [124] for Reynolds numbers up to 1.0e7. Moreover Hoerner [120] suggests a drag coefficient of about 0.12-0.2 for a large spherical balloon, depending on the supercritical Reynolds number. However several studies [108], [125-126], [130] suggest that this value can be increased significantly due to the presence of vortex induced vibrations in the dynamical behaviour of the tethered balloon. Although the accurate evaluation of the drag coefficient of the system is beyond the scope of this preliminary analysis, these previous studies demonstrate the importance of taking into account the possible variation of this parameter in this phase of the study. Therefore in this sensitivity analysis the coefficient value is increased from 0.2 up to 1 in order to identify a possible critical area to investigate more in depth.

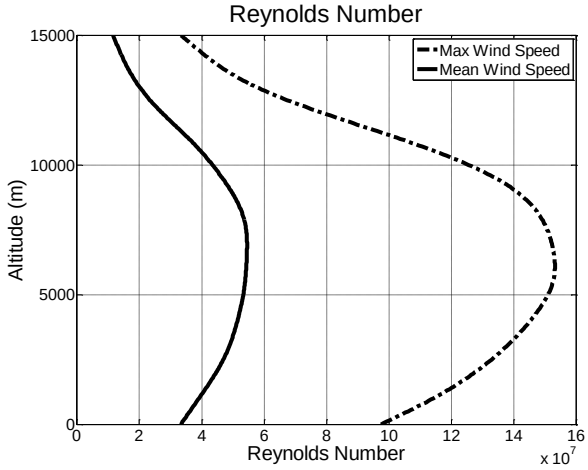

Figure 53 : Reynolds Number range

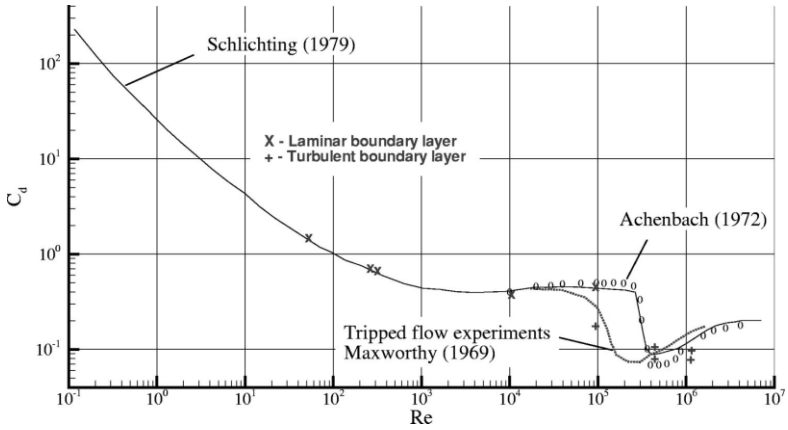

Figure 54 : Experimental drag coefficient for uniform flow over a sphere [122], [123], [124]

Figure 55 shows that the variation of the drag coefficient affects significantly the steady state horizontal displacement of the balloon. The final position is increased of the 125% when a drag coefficient of 1 is used in the model calculations. This corresponds to an absolute value of about 4100 m which can constitute an evident constraint, as a very large free area would be necessary around the mooring point. At the same time the vertical position of the balloon decreases to about 4500 m, which can affect the amount of radiation collected by 20%. Although the feasibility of the system is still verified (the balloon is still capable to stay aloft providing enough lift to support the systems) the results obtained highlight the importance of a more accurate estimate of this parameter. Furthermore the increase of the drag coefficient implies an increment of up to 75% in the maximum force along the tether as presented in Figure 56. The same figure also shows that the free lift is less influenced by the variation of the drag coefficient as the total weight of the system is not increased.

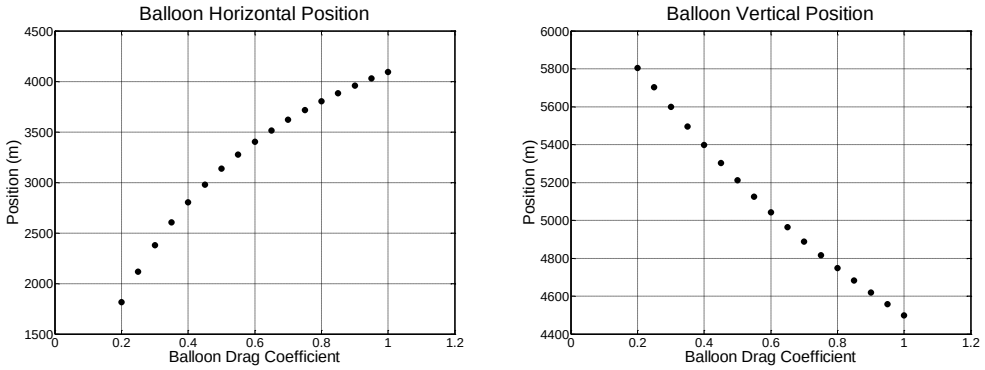

Figure 55 : Balloon Final Position as a function of the Balloon Drag Coefficient

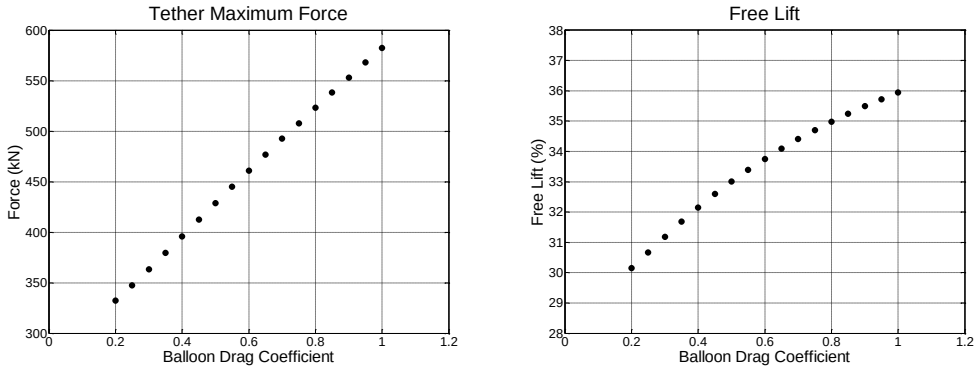

Figure 56 : Tether Maximum Force and Free Lift as a function of the Balloon Drag Coefficient

6.4.4 PV System Weight

Multiplying the PV system weight by a factor between 0.5 and 2, the position remains almost unchanged, with variations between -7% and 15% along the horizontal direction and less than 2% along the vertical (Figure 57). The effect on the maximum force value is similar while the free lift ranges from 24% and 33% (Figure 58). This means that a tolerance between -50% to 100% in the PV system weight estimate can be considered acceptable.

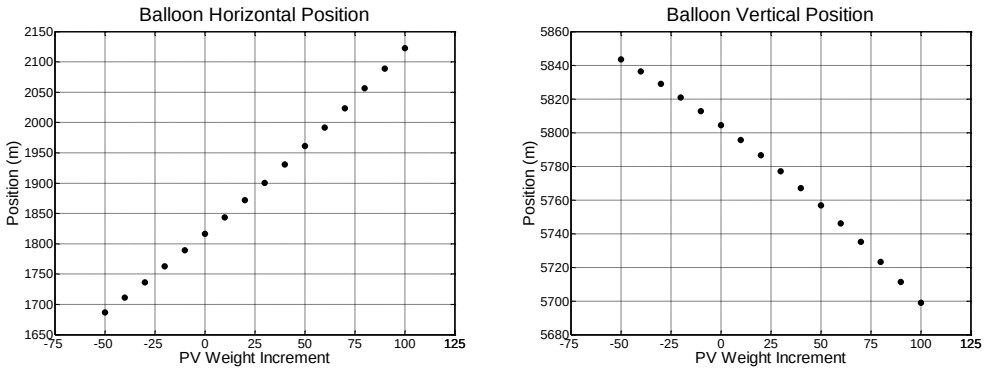

Figure 57 : Balloon Final Position as a function of the PV System Weight

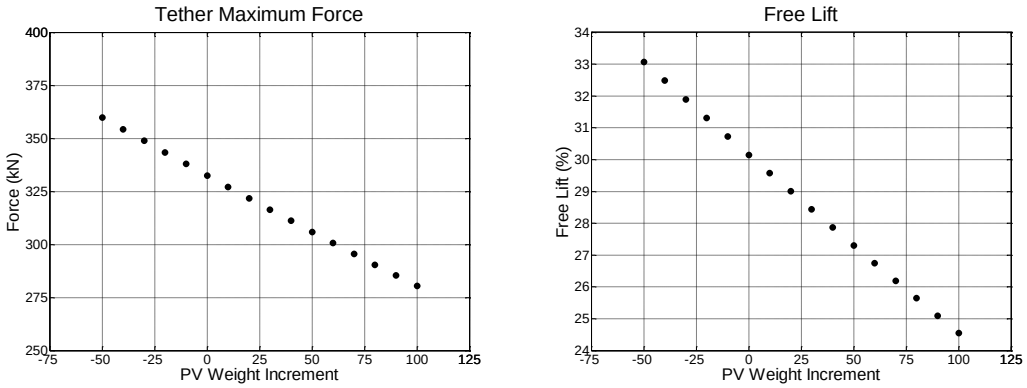

Figure 58 : Tether Maximum Force and Free Lift as a function of the PV System Weight

6.4.5 Inverter and Transformer Weight

Analogous considerations can be inferred considering the variation of the inverter and transformer weights compared in Figure 59 and Figure 60. Their contribution to the total system weight is very limited, and even considering variations of the 100% the resulting effect on the configuration is not significant.

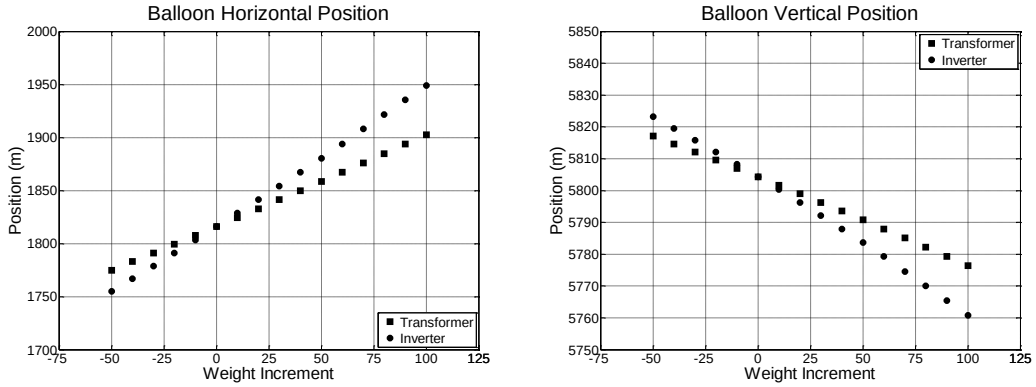

Figure 59 : Balloon Final Position as a function of the Inverter and Transformer Weight

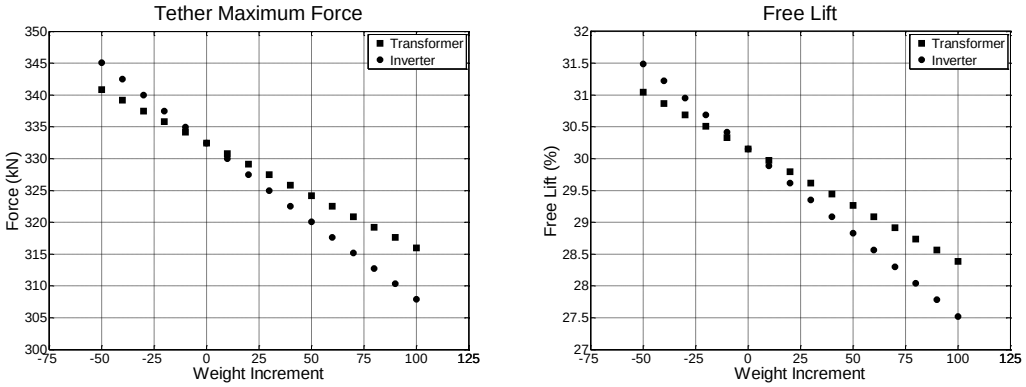

Figure 60 : Tether Max Force and Free Lift as a function of the Inverter and Transformer Weight

6.4.6 Tether Weight

For what concerns the transmission tether, the steady state model considers its internal structure as simply constituted by the conductor and the composite sections. The actual composition of cables used for power distribution and transmission includes the presence of other components like insulation layers and protective shields which can increase significantly the total weight. However it can be noticed how the final steady state result is not significantly affected by an increment in total weight between -50% and 100% as presented in Figure 61 and Figure 62.

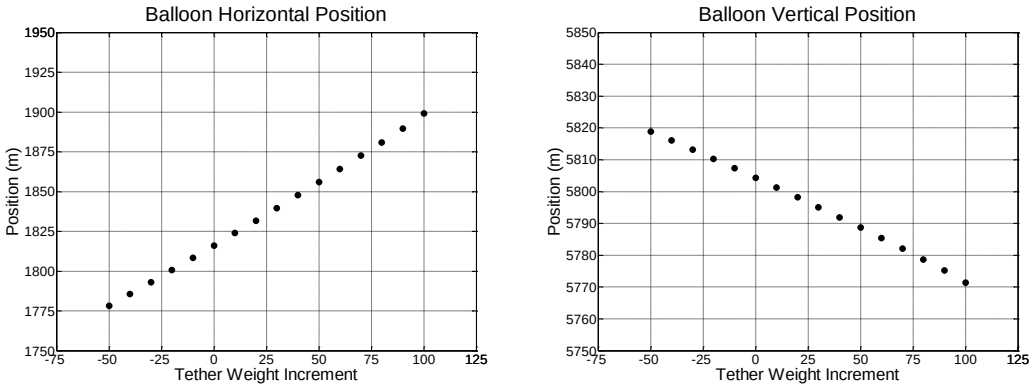

Figure 61 : Balloon Final Position as a function of the Tether Weight

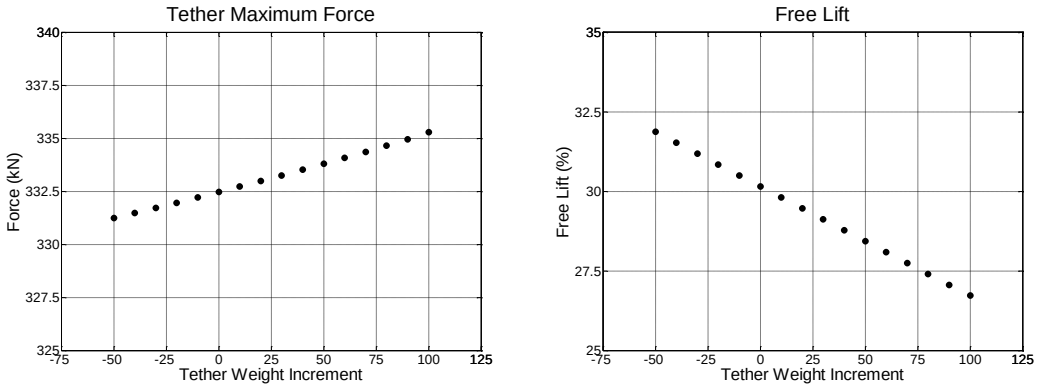

Figure 62 : Tether Max Force and Free Lift as a function of the Tether Weight

6.4.7 Wind Speed Profile

On the other hand, it is particularly important to take into account possible variations of the wind speed profile determined in section 3.2. In this sensitivity analysis the wind speed is progressively increased from the average value to the 3σ value. The probability that the wind speed will be lower than a defined value is expressed by the cumulative distribution function. Table 26 summarizes the relative cumulative distribution function values determined for different wind speeds at 6000 m.

Wind Speed [m/s]	Cumulative Distribution [%]
$\overline{V_{Wind}}$ = 20.1	58.7
$\overline{V_{Wind}} + 1 \cdot \sigma_{Wind} = 32.4$	86.0
$\overline{V_{Wind}} + 2 \cdot \sigma_{Wind} = 44.7$	96.6
$\overline{V_{Wind}} + 3 \cdot \sigma_{Wind} = 57.0$	99.4

Table 26 : Wind Speed Values with Relative Cumulative Distribution Functions

Figure 63 shows the resulting balloon position, which can be significantly affected in both horizontal and vertical directions. In particular the horizontal displacement reaches the maximum value of about 4700 m, while the corresponding vertical position is about 3800 m. It appears evident that even though the results demonstrate that the system can withstand the maximum wind speed, the very large displacements in the horizontal direction and the decreased value of the operating altitude could constitute an issue for the performance of the system. Also the combined effect of the increased wind speed and that of the variability of drag coefficient could contribute to the failure of the system in particular weather conditions. Possible considerations about the maximum tether force are quite similar to the one about the position while the free lift value seems less affected with a maximum value of about 38% of the buoyancy (Figure 64).

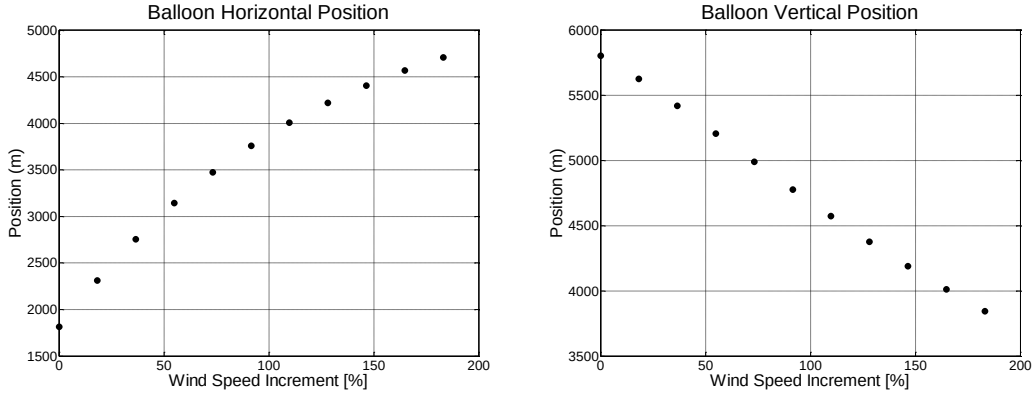

Figure 63 : Balloon Final Position as a function of the Wind Speed

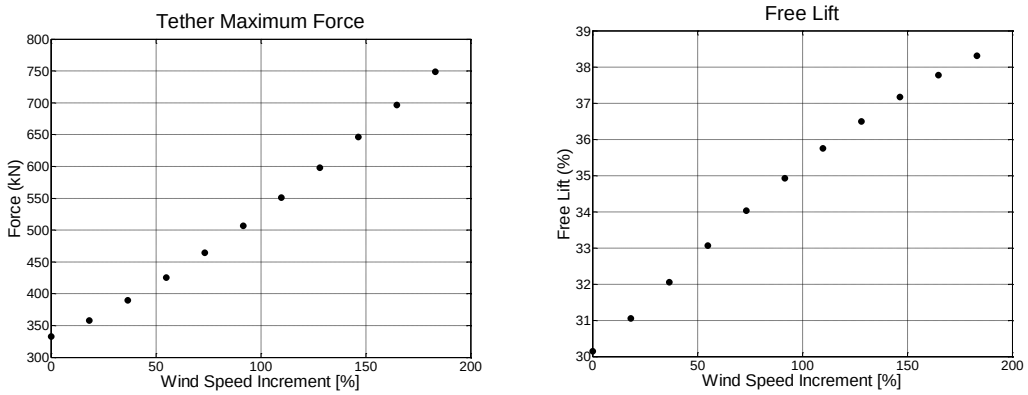

Figure 64 : Tether Max Force and Free Lift as a function of the Wind Speed

The sensitivity study presented demonstrates the overall feasibility of the system under the conditions assumed for the analysis. Moreover the results presented give more confidence about the viability of the generator. However some critical aspects involved in the design have been identified. In particular the results demonstrate the importance of an accurate estimate of the balloon drag coefficient which can have a significant effect on the final result. Furthermore the wind speed profile assessment has highlighted some important issues which could represent a problem for the performance of the system. On the other hand the weight variations assumed for the different components don’t seem to constitute a critical area to investigate, even though it must be pointed out that the sizing of many additional components remain to be addressed.

7 BASELINE CONFIGURATION DYNAMIC ANALYSIS

As a further assessment of the system feasibility before the actual concept design, this section presents the dynamic analysis implemented to evaluate the behaviour of the system when subjected to the unsteady atmospheric conditions. The analysis is based on a 3D finite element model which performs a complete transient analysis of the whole system starting from the equilibrium configuration determined by the 2D steady state model.

Several studies have been conducted in the past, most of which deal with the development of mathematical models to define the dynamic behaviour of tethered streamlined aerostats when subjected to operational atmospheric conditions [127,128]. More recent publications [87,118] present different dynamic simulations performed to assess the feasibility of very high altitude tethered balloon systems. In particular the work conducted at the McGill University has been focused on the design and analysis of the dynamics of systems based on lighter than air technology. The resulting publications ([129,130] and [108]) contain therefore a large wealth of information.

The study presented in this section introduces an alternative approach for the evaluation of the response of a tethered spherical aerostat, performing a full 3D dynamic non linear simulation based on a Finite Element Model (FEM). The method proposed has been developed and preliminarily validated by Aglietti [119] in the case of horizontal gusts. The model is here further extended and employed to perform a complete analysis of the AEPG when operating in a realistic design scenario which takes into account gusts along the three directions, vortex induced vibrations and simulated continuous turbulence. The results, including displacements and forces along the tether, are used to prove the operational viability of this tool and to further assess the technical feasibility of the system under analysis.

7.1 Model Description

The FEM model used in this study is extensively described in [119]. In this section the key points are recalled in order to identify the main characteristics of the model and introduce the possible advantages of this approach. The tethered balloon system, modeled using a commercial FE software (Ansys), is discretized into a defined number of elements and nodes, as in the case of the steady state model introduced in section 6.1. The number of nodes and segments is determined based on considerations about the

convergence of the results. The balloon is modelled as a 6 DOF (Degrees of Freedom) structural mass concentrated on a single node while the tether segments are modelled as standard FEM beam elements with tension, compression, torsion and bending capabilities which can include the effect of large deflections. The choice of beam elements instead of rods allows the simulation to take into account the bending stiffness of the tether that in some cases might be not negligible. The material properties include density, elastic modulus and Poisson's ratio. For what concerns the material damping, although this characteristic can be modeled in Ansys, its effect is assumed small compared to other sources of damping (e.g. aerodynamic damping) and it is not included in the present model. The forces due to the buoyancy, weight and aerodynamic effects are assumed to be applied on the nodes connecting two consecutive elements as in the steady state model. The constraint on the ground is modelled as a "pin", releasing the rotation about the three axes.

Since the mass of the balloon is comparable to that of the displaced fluid, a dynamic simulation needs to include the contribution of the added mass. Therefore, this contribution has been taken into account and assumed as half the value of the displaced fluid mass [120], considering the spherical shape of the balloon. It should be pointed out that this assumption is valid for irrotational flows and a more accurate estimate should be considered for applications in which the vorticity effects are significant [131]. Nevertheless the practical validity of the theoretical results in [120] has been confirmed in previous publications [125] even in the case of separated flows.

The simulation operates with an time-stepping scheme as the one presented in Figure 65. The time domain (duration of the simulation) is divided in time steps and at each time step the simulation calculates the displacements of the structure and the forces in the elements. The solution of each time step is used to update the loads on the system, which depend on position and velocity of each node. The updated loads are used as input for the following time step calculations.

Starting from the steady state condition determined in section 6 for the baseline configuration, the unsteady atmospheric conditions defined in section 3.3 are superimposed to the mean wind speed and applied to the balloon to assess the dynamic response.

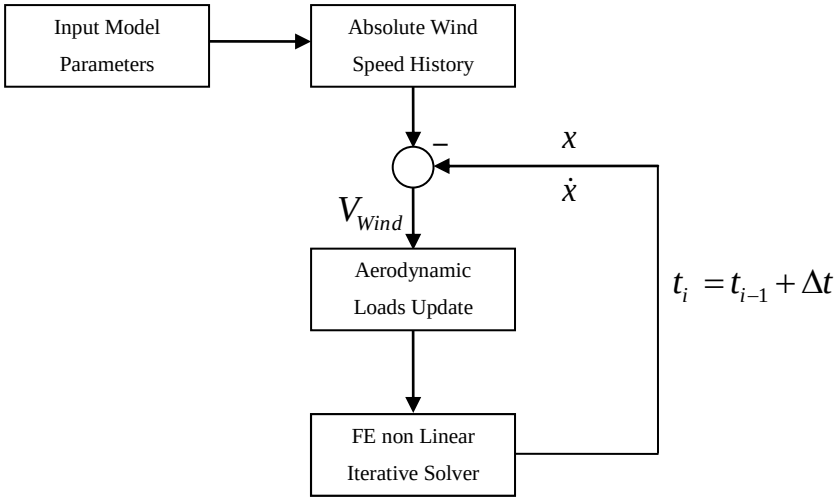

Figure 65 : FEM Simulation Iterative Scheme

7.2 Discrete Gust Response

As a first step in the study of the dynamic behavior of the system under analysis, the discrete gust described in section 3.3.1 is applied along the three different directions (longitudinal, lateral and vertical) with respect to the mean wind speed. After the application of the gust the system is subjected to the only mean wind profile until the new equilibrium condition is reached, in order to analyze the complete response to the load applied.

The results determined considering two different values for the balloon drag coefficient (0.2 and 0.8) are compared in order to evaluate the influence of this parameter on the dynamic response of the system. It must be pointed out that the drag coefficient has a significant effect on the balloon position and final shape of the tether in steady state conditions as presented in the sensitivity analysis of section 6.4. The equilibrium values obtained considering $C_D^B = 0.8$ are 4747.8 m and 3802.3 m for vertical and horizontal positions, while the minimum inclination angle is 50.2°. However the present section is focused on the evaluation of the behaviour of the tethered platform when subjected to realistic operating conditions and the results are therefore focused on the dynamic response evaluated starting from the steady state configuration.

7.2.1 Longitudinal Gust

First of all the gust is applied to the balloon only in the same direction as the mean wind speed which is defined as longitudinal. The simulation is therefore still 2 dimensional

since the response of the balloon will still be on the longitudinal-vertical plane. Figure 66 shows the longitudinal and vertical displacements of the balloon, relative to the steady state position. It can be noticed how the response in the longitudinal direction is overdamped and it does not experience any evident oscillations. The same overdamped behaviour can be seen in the vertical response although a higher frequency oscillation is superimposed. From the plot the period of oscillation can be determined which results equal to 34.5 s. Another important result to be considered is the maximum value of the force along the tether obtained for the node attached to the balloon. Figure 67 shows an increment of about 9% (Cd = 0.2) and 25% (Cd = 0.8) compared to the force in equilibrium conditions. The observed period of oscillation is 34.5 s.

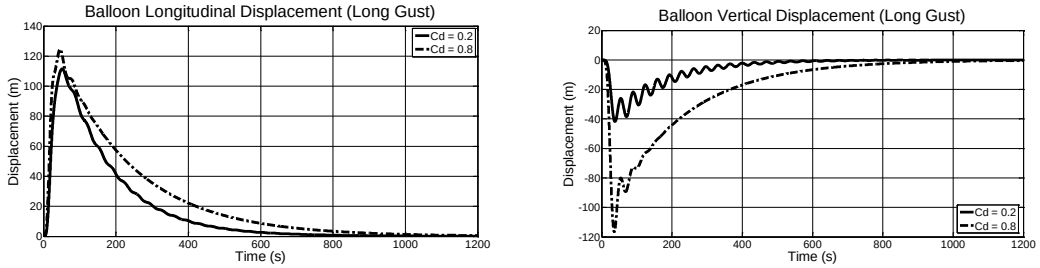

Figure 66 : Longitudinal (left) and Vertical (right) System Response to a Longitudinal Gust

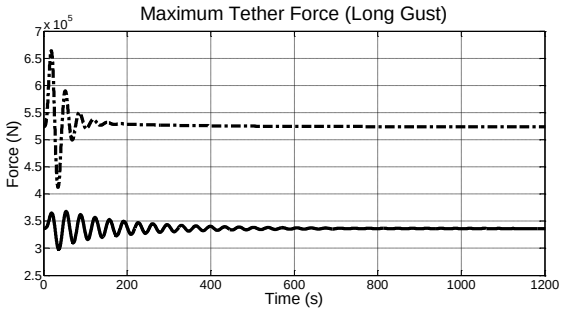

Figure 67 : Tether Maximum Force due to a Longitudinal Gust

7.2.2 Vertical Gust

The results obtained when a vertical gust is applied to the balloon are shown in Figure 68 and Figure 69. Again the response is on the longitudinal-vertical plane and the absolute values of the displacements are lower than in the case of a gust in the longitudinal direction. Moreover the period of the oscillations observed in the displacement plots are 34.5 s as the one determined in the case of the longitudinal gust. For what concerns the value of the force, the maximum increment is about 8% (Cd = 0.2) and 17% (Cd = 0.8) compared to the steady state case.

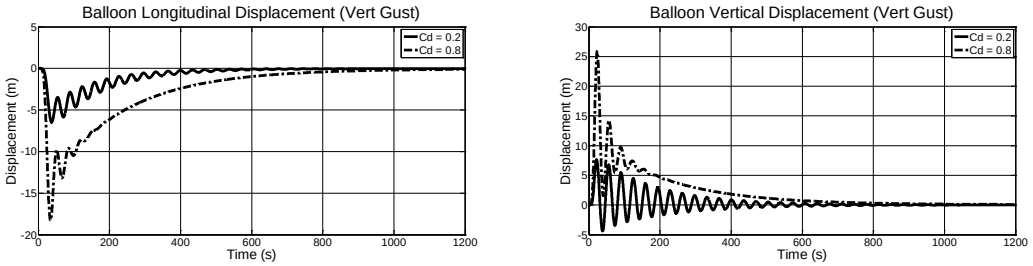

Figure 68 : Longitudinal (left) and Vertical (right) System Response to a Vertical Gust

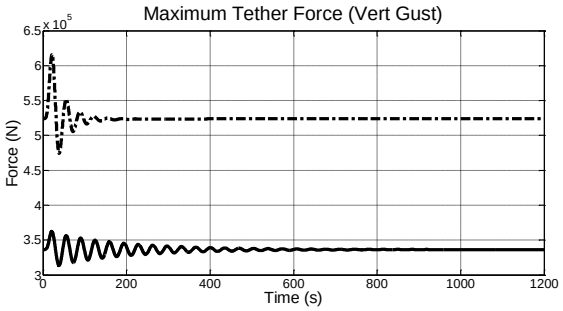

Figure 69 : Tether Maximum Force due to a Vertical Gust

The application of the lateral gust results in a response of the system in the vertical-lateral plane (Figure 70) as the oscillations in the longitudinal direction are negligible. In this case the results include a first oscillation visible in the vertical response plot and a second one at lower frequency in the lateral direction. The higher frequency oscillation shows the same period as the previous simulations (34.5 s). The lower frequency oscillations that can be determined by the lateral displacement plot is 289.5 s. The increase of the maximum value of the force (Figure 71) is less significant in this case (0.03% for Cd = 0.2 and 0.19% for Cd = 0.8).

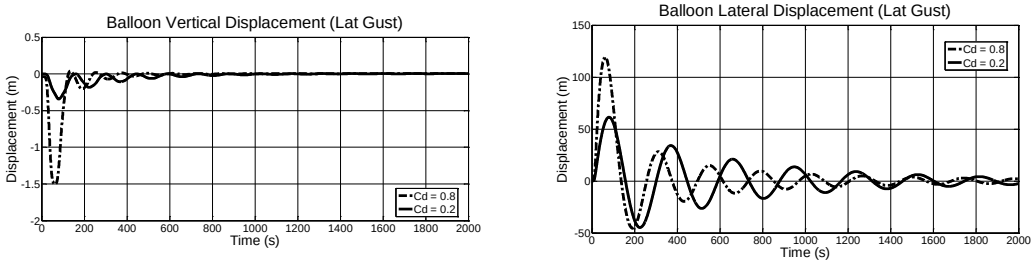

Figure 70 : Vertical (left) and Lateral (right) System Response to a Lateral Gust

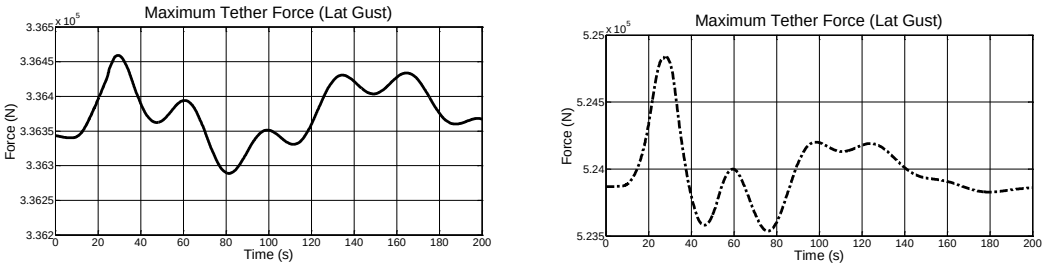

Figure 71 : Tether Maximum Force due to a Lateral Gust (Cd = 0.2 and Cd = 0.8)

7.2.3 Oscillation Period Comparison

The periods of the oscillations determined in the three cases can be compared to the analytical solutions obtained for different idealized cases. The frequencies for the pendulum and the axial spring modes are determined in [129] as:

$$\omega_n = \sqrt{\frac{B - mg}{m_e \cdot len^{tether}}} \tag{7.1}$$

for the pendulum mode and:

$$\omega_n = \sqrt{\frac{E_{Comp} \cdot A_{Comp}}{m_e \cdot len^{tether}}} \tag{7.2}$$

for the axial spring mode, where m_e is the total mass of the aerostat which includes the value of the added mass (assumed as one half of the mass of the displaced fluid). The tether length considered is the initial value (non-stretched). The period of oscillation is determined as:

$$T = \frac{2\pi}{\omega_n} \tag{7.3}$$

Table 27 provides the comparison between the values of the oscillation periods obtained from the simulation and the theoretical results calculated.

	Simulation	Theory
Pendulum	289.5 s	286.2 s
Axial Spring	34.5 s	33.9 s

Table 27 : Comparison between theory and simulation oscillation periods

The comparison shows a good accordance since the discrepancy is of 1.15% in the case of the pendulum and 1.77% in the case of axial spring.

7.3 Vortex Induced Vibrations Response

Previous publications ([125], [126] and [132]) have demonstrated that a tethered sphere subjected to a constant wind speed, will tend to oscillate both in line and transversely to the flow direction. The amplitude of the transverse oscillation can reach a saturation value of close to one spherical diameter, while the in line oscillations are less important, leading to eight or crescent shaped trajectories.

In particular the study presented in [132] identifies 4 different vibration modes which are related to the formation of vortices in the wake behind the sphere. These modes are found to be function of the reduced flow velocity defined as:

$$V_{\mathrm{Red}} = \frac{V_{Wind}}{f_N \phi_B} \tag{7.4}$$

where f_N is the pendulum natural oscillation frequency [Hz]. The first two modes (Mode I and II) occur for reduced velocities between 5 and 10. In this range the natural frequency of the pendulum is close to the vortex formation frequency in the wake behind the sphere. The two modes are therefore associated with a lock in of the principal vortex shedding frequency with the body oscillation frequency. On the other hand, the third mode (Mode III) described in [132] occurs at higher reduced velocities (between 20 and 40) where the vortex formation frequency is much higher than the vibration frequency. This mode is the result of a movement induced vibration (as explained in [133]) which is responsible of an energy transfer between fluid and sphere for each cycle. For reduced velocities between 40 and 100 the sphere amplitude response is negligible until the fourth mode (Mode IV) occurs, which is not periodic but characterized by intermittent bursts of large amplitude vibrations. The value of reduced velocity calculated for the configuration considered in this study is 87.9 which is outside the ranges of reduced velocities of the four modes presented in [132]. However another important result obtained in the extensive study performed by Williamson and Govardhan [125] concerns the effect of the mass ratio on the synchronization regime, i.e. the range of velocities in which the vortex induced vibrations can occur. The mass ratio is defined as:

$$m^* = \frac{m}{m_{Fluid}} \tag{7.5}$$

where m_{Fluid} is the mass of the displaced fluid [kg]. Lower values for the mass ratio have the effect of extending the synchronization regime. Moreover a critical value for this parameter, below which large amplitude vibrations persist to infinite reduced velocities, is determined in [125] as:

$$m^*_{Crit} = 0.6 \pm 0.05 \tag{7.6}$$

The mass ratio values estimated for the particular configuration considered in this study is 0.6. It is therefore important to consider the possible presence of these oscillations and their effect on the system. In particular, in order to assess the technical feasibility of the generator, it is necessary to estimate the increased value of the maximum force along the tether. Considering the reduced velocity value obtained, it can be noticed that the system operates far from the flow conditions, in which the lock in occurs. As a

consequence the vortex induced vibrations response is assumed to belong to the movement induced vibrations category described in [133].

The method used to model the forces responsible for the transverse vibrations is derived from [130], approximating the forces with sine functions. The magnitude of the lateral force (F_0) is determined starting from the amplitude of the lateral displacement (Y_{Amp}) and from the value of total aerostat mass (including added mass), system damping ratio (ς) and oscillation frequency:

$$F_0 = 2Y_{Amp} m_e \omega_n^2 \varsigma \tag{7.7}$$

A first estimate of the damping ratio can be derived from the results obtained in section 7.2 when a lateral gust is applied to the system (Figure 70b). The value obtained for this parameter is 0.09. The resulting sinusoidal force, determined as

$$F(t) = F_0 \sin(\omega_n t) \tag{7.8}$$

is applied to the system considering an oscillation amplitude equal to the diameter of the balloon.

As the force is applied starting from the equilibrium conditions, the first phase of the response is a transition in which the lateral oscillation amplitude increases until it reaches the value set for Y_{Amp} . The peak forces obtained in this phase are not representative of the load condition as in the case of the single gust and the analysis is focused on the assessment of the response in stationary conditions. The lateral displacements obtained are presented in Figure 72.

For what concerns the longitudinal displacements, the values observed are negligible compared to the lateral oscillation. Moreover the increase in the maximum tether force is extremely small as shown in Figure 73 and it constitutes the 0.05% of the value obtained in steady state conditions.

As a caveat it must be pointed out that the characteristics of the system under analysis are quite different from the one considered for the study presented in [125]. In particular the tether weight is significant and affects the value of the sag, which is negligible in the experiments described in [125].

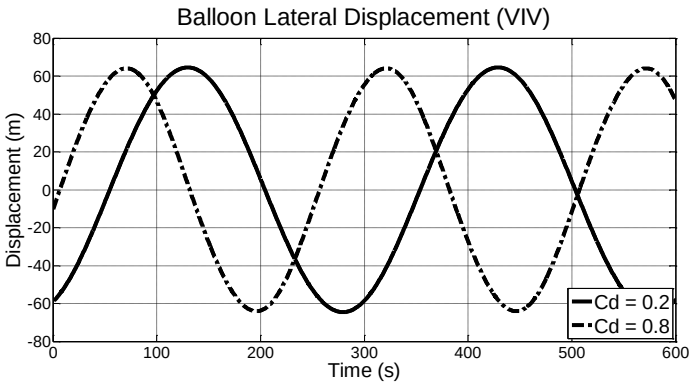

Figure 72 : Lateral Displacements due to Vortex Induced Vibrations

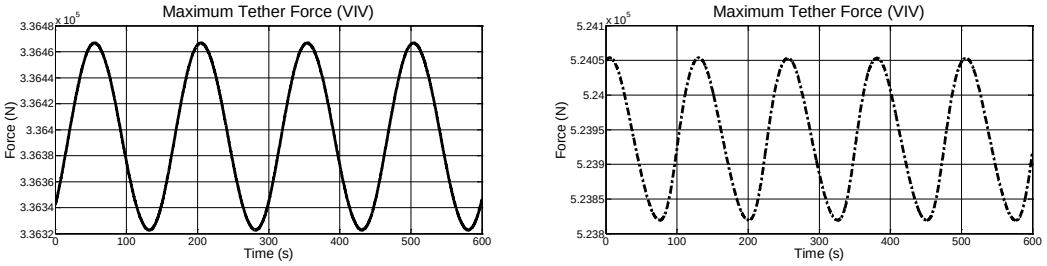

Figure 73 : Tether Maximum Force due to Vortex Induced Vibrations (Cd = 0.2 and Cd = 0.8)

7.4 Atmospheric Turbulence Response

As described in section 3.3.2, atmospheric turbulence is simulated considering the power spectral density provided by Von Karman as a function of the wave number Ω and of the mean wind velocity $\overline{V_{Wind}}$. As a first approximation, the mean wind velocity is set to 20.1 m/s in the following calculations, which is the value relative to an altitude of 6000 m. The wave number range of interest is divided into N intervals with an increasing width of $\Delta\Omega_i = 1.2\Delta\Omega_{i-1}$, having set the initial values to $\Omega_0 = 0.0001$ and $\Delta\Omega_0 = 0.0001$. The turbulence is generated selecting a random wave number for each of the intervals determined. Since the wave number can be related to the turbulence frequency as $f = \frac{\overline{V_{Wind}} \cdot \Omega}{2\pi}$, the choice of a defined N number of intervals determines the maximum frequency content of the simulated turbulence.

7.4.1 Frequency Content Evaluation

In order to obtain representative results of the dynamic behaviour of the system, it is important to include all the frequencies that can influence the response of the system in the range considered for the simulation. The maximum frequency selected also determines the time step value which needs to be small enough to avoid problems

related to the aliasing of the signal. From a computational point of view, the possibility of increasing the size of time steps allows the simulation to be less time consuming even though it might be detrimental for the accuracy of the final result. It is therefore necessary to include some preliminary exploratory calculations aimed to the identification of suitable values for the parameter N and for the simulation time step. Three different turbulence profiles are considered setting the parameters to the values presented in Table 28. Slightly different values of the maximum frequency for the longitudinal, lateral and vertical turbulence are due to the fact that the values are randomly selected in each interval.

Turbulence	**1**			**2**			**3**		
Direction	**Lon**	**Lat**	**Ver**	**Lon**	**Lat**	**Ver**	**Lon**	**Lat**	**Ver**
N intervals	50	50	50	40	40	40	30	30	30
Max Freq [Hz]	13.65	12.83	14.42	2.27	2.21	2.14	0.33	0.34	0.36
Solution ΔT [s]	0.025	0.025	0.025	0.1	0.1	0.1	0.25	0.25	0.25

Table 28 : Turbulence Parameters for Frequency Comparison

It can be noticed that the lowest of the three maximum frequencies chosen (turbulence 3) is about 10 times the axial spring frequency determined in section 7.2. The comparison between the three generated turbulences is presented in Figure 74-Figure 76. The displacements obtained in the three cases are shown in Figure 77. It can be noticed that the results are comparable, with minimal differences even in the case of the third turbulence. For what concerns the maximum value of the force along the tether, obtained for the node attached to the balloon, the results are presented in Figure 78. As mentioned in the previous sections, the turbulence is applied after the system has reached an equilibrium condition due to the constant mean wind profile. The results show therefore an initial (10 seconds) high frequency oscillatory transient. Again, the differences between the simulations are small even though it can be seen how turbulence 3 introduces some other oscillation, probably due to numerical effects. The solution stabilises after about 30 seconds and converges to the same results as the ones obtained with turbulence 1 and 2. The choice of using the parameters set for turbulence 3 to define the input of the model seems reasonable. This allows saving computational time (50% duration) while obtaining a result representative of the real situation, since higher frequencies in the input turbulence are filtered by the system. As an indication of the time necessary to perform the computations, the simulation presented in section 7.4.2 required about one hour to run on an Intel Core2 Duo processor (@ 3 GHz, 3.9GB RAM).

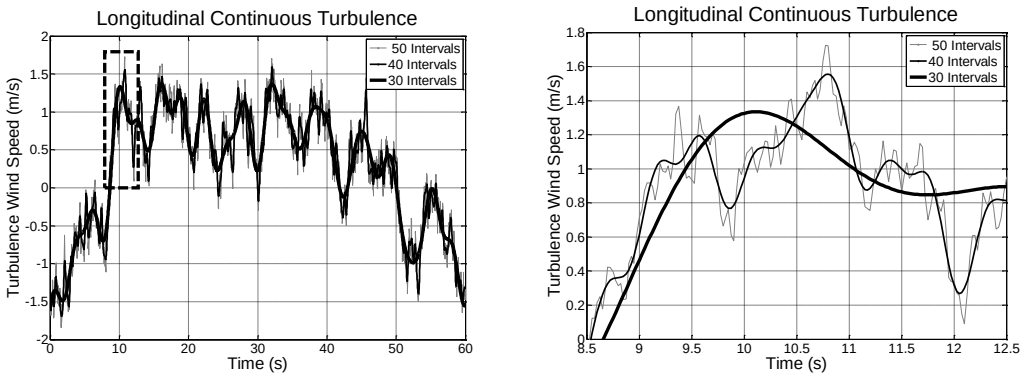

Figure 74 : Longitudinal Turbulence - Frequency Content Comparison (Left: Full Time Scale- Right: Detail)

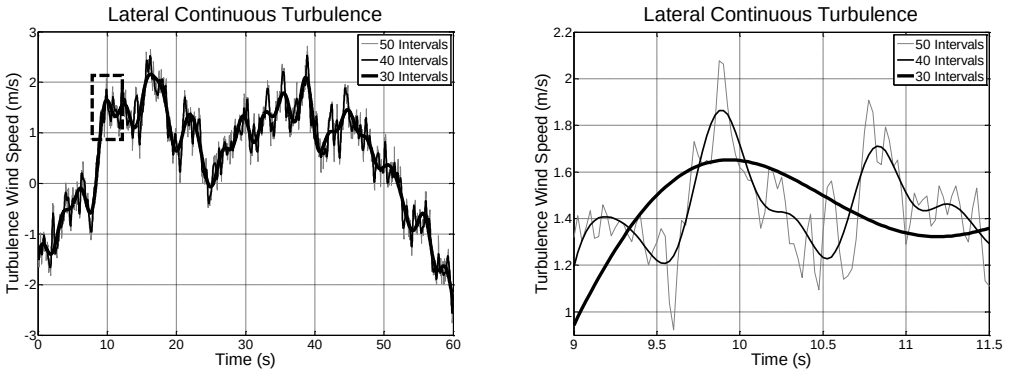

Figure 75 : Lateral Turbulence – Frequency Content Comparison (Left: Full Time Scale- Right: Detail)

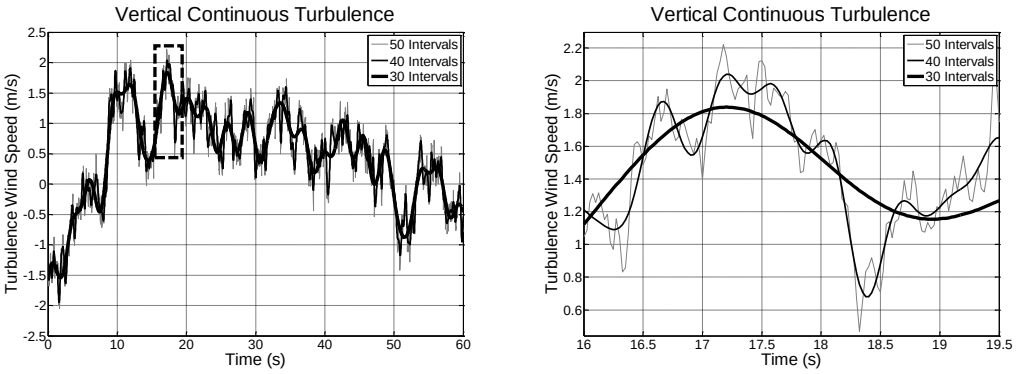

Figure 76 : Vertical Turbulence – Frequency Content Comparison (Left: Full Time Scale- Right: Detail)

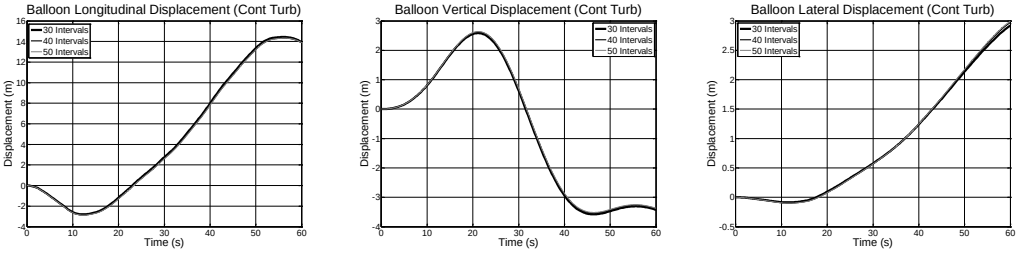

Figure 77 : Longitudinal (Left), Vertical (Center) and Lateral (Right) System Response to Turbulence

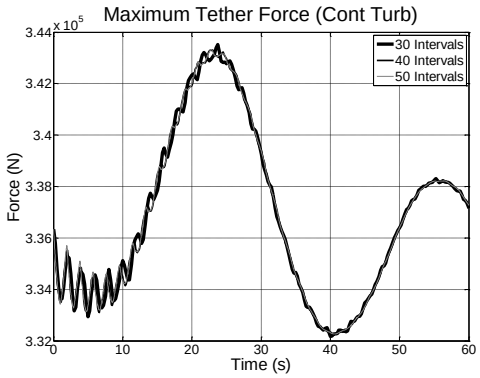

Figure 78 : Tether Maximum Force due to Turbulence

7.4.2 Dynamic Simulation Results

The turbulence parameters and time step defined in the previous section are used to perform a 20 minutes simulation and to evaluate the response of the AEPG in realistic working conditions. As in the case of the single gust along the three directions and the vortex induced vibrations, the results considered concern the balloon displacements and the maximum force along the mooring tether (Figure 79-Figure 81).
Considering the longitudinal displacements, the absolute values obtained are less than 100 m and the effect of the increased drag coefficient is not significant. On the other hand, the effect of the increased balloon drag coefficient appears more evident evaluating the vertical displacements, where the maximum values obtained are 30 m for $C_D^B = 0.2$ and 80 m for $C_D^B = 0.8$. A similar effect can be observed in the case of the lateral direction, where the magnitude of the displacements is comparable with the vertical ones (30 m and 50 m). In order to assess the technical feasibility of the system it is important to compare the absolute values of the displacements obtained with the application of the three dimensional turbulence, to the position determined in steady state conditions. The longitudinal oscillations represent the 5.7% and 2.7% of the equilibrium position for the two drag coefficients considered, while the amplitude of the vertical displacements are less than 0.5% and 1.7% of the steady state altitude value. Finally the forces presented in Figure 81 show an oscillation about the steady state value which produces an increase in the tether tension. The maximum increase can be estimated from the peak forces as the 3.3% of the equilibrium value in the case of low balloon drag and 9% in the case of high drag coefficient.

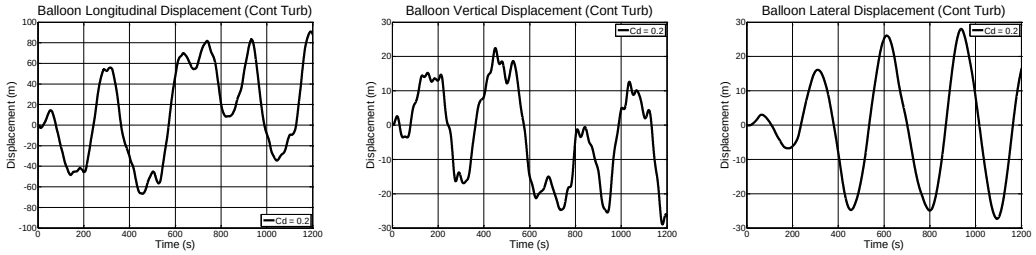

Figure 79 : Longitudinal (left), Vertical (Center) and Lateral (Right) Response to Turbulence ($C_D^B = 0.2$)

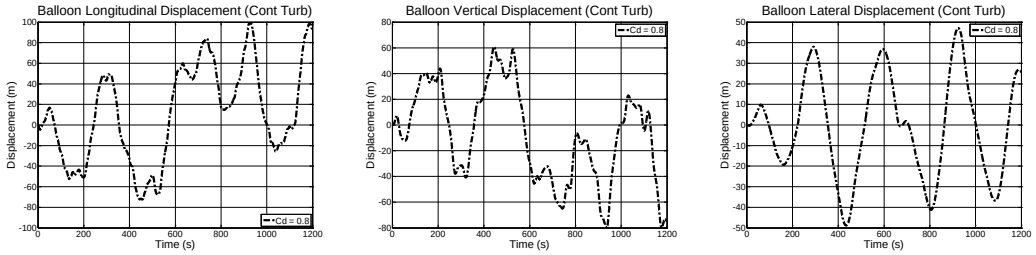

Figure 80 : Longitudinal (left), Vertical (Center) and Lateral (Right) Response to Turbulence ($C_D^B = 0.8$)

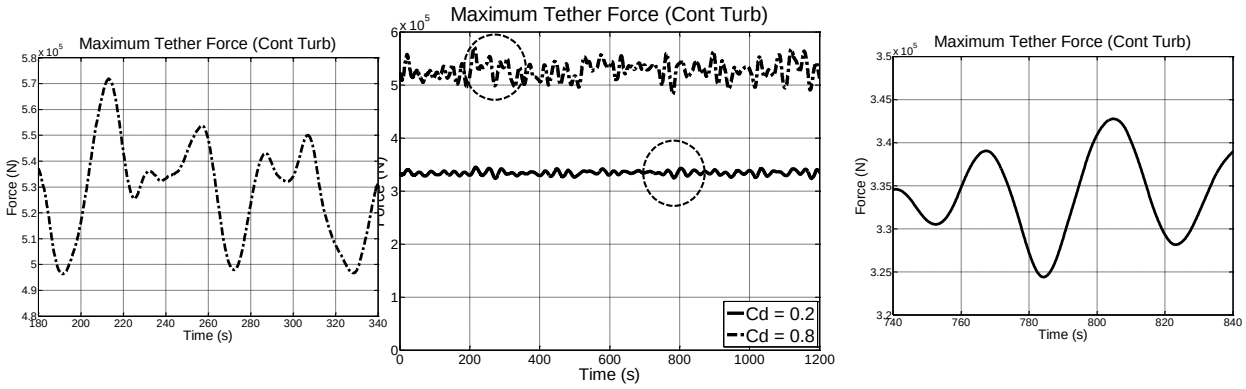

Figure 81 : Tether Maximum Force due to Turbulence

The response to a discrete gust presented in section 7.2 has highlighted the presence of two oscillation modes, i.e. lateral pendulum and axial spring with two specific frequencies of 0.0035 Hz and 0.029 Hz in the case of $C_D^B = 0.2$. Figure 79 and Figure 81 show some characteristic oscillations whose frequencies can be determined by the time distances between the peaks. In particular the results obtained for the lateral displacement (0.0034 Hz) and for the tether force (0.031 Hz) demonstrate that the two oscillation modes are still represented in the continuous turbulence simulation.

The figures presented in this section quantify the dynamic response of the system in terms of displacements and tether forces contributing to the assessment of the technical feasibility of the AEPG. On the base of the results obtained, it can be inferred that the

dynamic behavior of the system doesn’t constitute a show stopper for the development of the flying generator.

8 AEPG CONCEPT DESIGN

After having addressed important preliminary issues which can be considered common to other flying platforms and tether balloons, this chapter focuses on the specific application of the Aerostat for Electric Power Generation (AEPG) introducing the main technical aspects involved in the design process.

The analysis starts from the selection and sizing of the structural components which need to provide structural integrity to the overall system. Moreover the choice of a particular layout for the structure of the AEPG is also driven by the need of minimizing problems related to the inertial characteristics of the system such as instabilities due to the relative positions of centre of mass and centre of buoyancy. Therefore the structure has to provide the interfaces to the various subsystems in order to distribute the different mass contributions and obtain a convenient equilibrium configuration. The structural components include the external envelope, the annular plates employed to support the solar arrays as well as the elements responsible for the distribution of the loads on the membrane.

Once the mass of these components and the structural layout are defined, the inertial characteristics of the system can be evaluated preliminarily. These characteristics, together with preliminary considerations about the performance required to point the sun direction, constitute the input for the choice and sizing of the pointing mechanism components.

The concept layout is finally presented and the total mass breakdown is compared with the previously determined value for the disposable lift. Moreover different considerations on the inertial characteristics and overall balance of the system are added in order to complete the preliminary assessment of the technical feasibility of the generator.

8.1 LTA Structural Solutions

Before addressing the concept layout of the generator, it is important to introduce the different structural solutions usually employed for the design of LTA vehicles in order to get a better idea of the available options during the development of the AEPG.

Traditionally the typologies of the lighter than air vehicles can be divided into three groups, i.e. rigid, non rigid and semi-rigid. Rigid airships have an internal skeletal frame which carries all the mechanical loads and is covered by an external envelope that

provides the aerodynamic shape. The lifting gas is contained in separated gas bags located inside the frame which also provides the support for all the different subsystems. This technology has been used to design and build huge airships like the Zeppelin (Figure 82) and the R100, but it has now become less common for the development of modern systems.

Figure 82 : Rigid Airship [134]

On the contrary present airships can rely on the membrane stresses generated by the internal gas superpressure to withstand the bending moments and the forces applied to the vehicle. They have no internal frame or supports to maintain the shape of the external envelope and the weight of the subsystems is distributed with the use of a system of curtains and catenary (Figure 83).

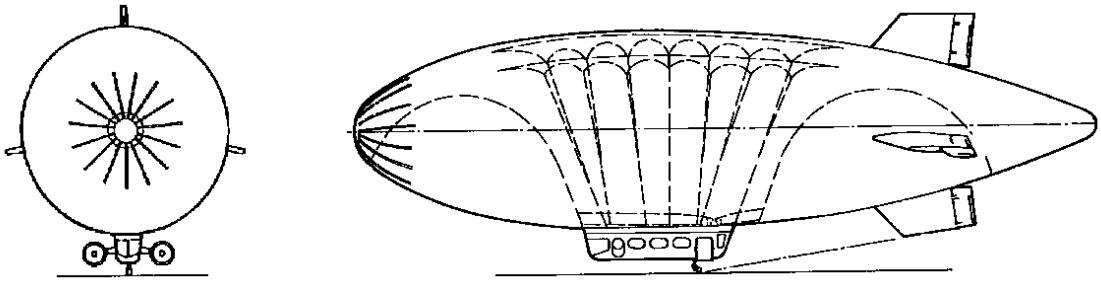

Figure 83 : Non rigid Airship – Blimp (available at [135])

As a compromise between the two solutions presented above the semirigid airships combine the features of rigid and non-rigid vehicles. They have both a keel structure located on the bottom part of the vehicle and a pressurised envelope which carry together the structural loads due to the weight of the subsystems and withstand the dynamic pressure due to the speed of the relative wind (Figure 84).

Figure 84 : Semirigid Airship [136]

The three mentioned structures can provide an overview of the available possibilities for the preliminary design phase. Nevertheless it must be pointed out that the AEPG has requirements that can be quite different from the ones of the traditional lighter than air vehicles. First of all the AEPG belongs to the particular category of tethered aerostats which don't carry people and are used at the moment mainly for scientific and military observation. These systems usually have non rigid envelopes which provide the necessary lift and stability to maintain the payload aloft. They don't need propulsion and attitude control systems since they are attached to the ground via the mooring cable and the payload can be autonomously pointed (Figure 85).

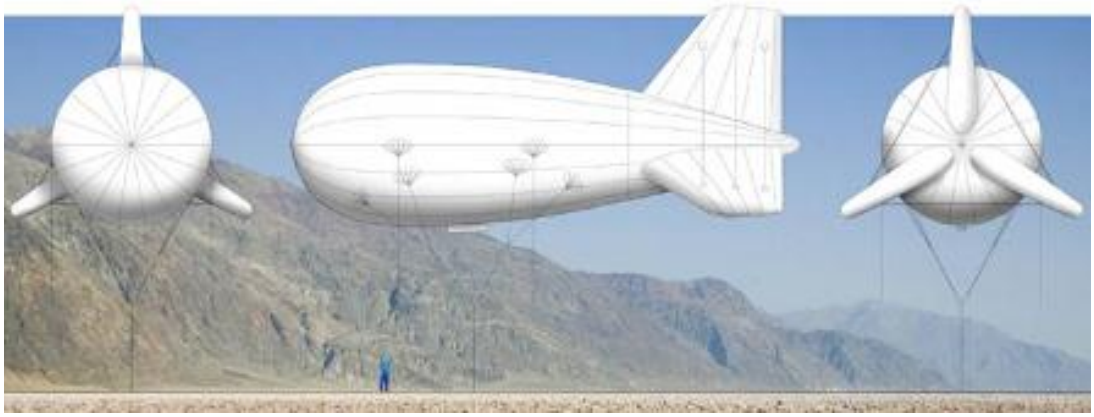

Figure 85 : Tethered Aerostat

In the case of the AEPG the lighter than air vehicle is moored to the ground but at the same time it needs to point the solar array towards the sun direction performing the azimuth and elevation rotations of the whole system. Moreover the cells are located on the external surface of the spherical balloon, while the other subsystems need to be stored in protected housings to prevent them from damage. For these reasons the types

of structures presented can only be considered to have an idea of the direction where to point (rigid, non rigid or semi-rigid). The specific technical solution adopted will be different from the ones traditionally employed for the lighter than air vehicles currently in operation.

8.2 External Envelope

The external envelope layout presented in Figure 86 includes a spherical membrane (highlighted in red) and a stepped structure (highlighted in green) employed to support the photovoltaic arrays. These arrays are mounted on a lightweight rigid substrate which is highlighted in grey. The stepped structure is necessary to compensate for the curvature of the spherical envelope and obtain a series of parallel surfaces pointing towards the same direction. When performing the Sun pointing manoeuvres, this structure allows to minimise the angle of incidence between PV cells and solar beam and to optimize the power generation.

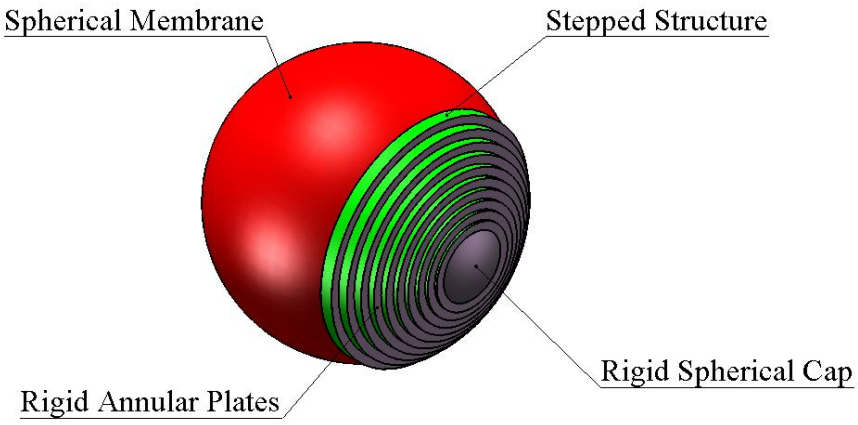

Figure 86 : External Envelope

The spherical envelope is assumed to be constituted by a simply pressurised membrane which maintains its shape thanks to a properly defined value of the internal gas pressure that prevents the structure from collapsing when external loads are applied. The external loads are mainly constituted by the dynamic pressure due to the relative wind speed and the level of internal pressure must be high enough to overcome the dynamic pressure at the stagnation point. Moreover the loads due to the weight of the different subsystems supported by the envelope needs to be considered.

On the other hand two different technical solutions are considered for the stepped structure responsible for the support of the PV array. The first one concerns the possible employment of a rigid structure externally attached to the spherical envelope. This structure consists of a lightweight truss which has to support the PV array and distribute

the loads due to the external dynamic pressure over the membrane surface. The second solution assumes the stepped structure to be constituted by a membrane which is internally pressurised like the spherical envelope.
The analysis starts from the spherical envelope. The superpressure necessary to maintain the overall shape is determined together with the stress generated in the membrane. The layout of the PV array is then introduced and the two different solutions for the support of this component are assessed.

8.2.1 Pressurised Spherical Membrane

Internal Superpressure Determination

As a first step in the evaluation of the required internal gas pressure value, it is necessary to introduce the physical mechanism that generates the aerostatic lift force on the balloon, extensively described in [109] and here summarised. Considering the LTA gas filled spherical envelope shown in Figure 87, the internal and external static pressures at the bottom level ($z = 0$) are, for the moment, assumed to be equal:

$$p_{Air}(0) = p_{Gas}(0) = p_0 \tag{8.1}$$

As higher values of z along the vertical axis are considered, the static pressure inside the balloon varies as:

$$p_{Gas}(z) = p_0 - g \cdot \rho_{Gas} z \tag{8.2}$$

where ρ_{Gas} is the buoyant gas density [kg/m^3] and g is the gravity acceleration [m/s^2]. The external atmospheric pressure varies according to the same function, but substituting the density value with ρ_{Air}:

$$p_{Air}(z) = p_0 - g \cdot \rho_{Air} z \tag{8.3}$$

Since $\rho_{Gas} < \rho_{Air}$, the difference:

$$\Delta p(z) = p_{Gas}(z) - p_{Air}(z) = g \cdot (\rho_{Air} - \rho_{Gas}) z \tag{8.4}$$

will be positive and it will increase as larger values of z are taken into account, reaching a maximum for the top of the spherical envelope. The pressure difference integrated over the total envelope surface will produce a force in the upward direction defined as aerostatic lift. It is important to notice that the pressure acts on the internal surface pushing outward, and generating stress on the structure as described in the following sections.

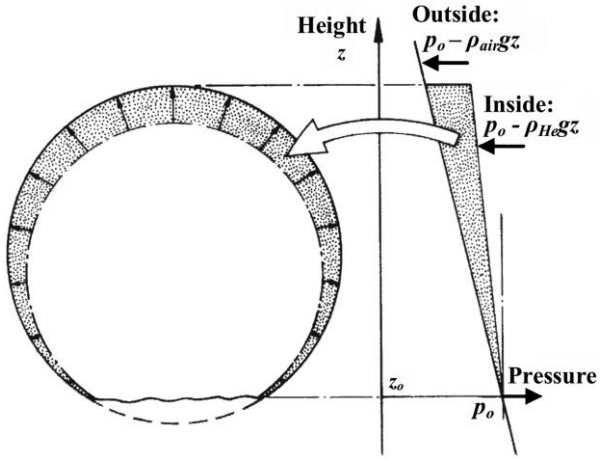

Figure 87 : Buoyancy Effect [109] – Buoyant Gas Helium

For the moment the analysis will focus on the determination of the pressure difference required for the envelope to maintain its shape. It is therefore important to evaluate the external load due to the dynamic pressure (i.e. deriving from the relative wind speed value) as it represents the value that needs to be internally provided in correspondence to the stagnation point.

Considering the layout presented in Figure 88, the envelope is assumed to be subjected to a constant relative wind speed, directed in the upward direction even though generally speaking the relative wind could come from any direction (not necessarily vertical nor horizontal). As previously stated, a LTA vehicle which employs a non rigid structure (blimp) relies only on the internal gas pressure to maintain its shape when subjected to the external loads. Therefore, in order for the envelope to keep its shape (non-dimpling condition [108]), it is necessary that on the stagnation point the internal static pressure (p_{Int}) is equal to the external static pressure (p_{Ext}) plus the contribution of the dynamic pressure due to the wind speed:

$$p_{Int}(0) = p_{Ext}(0) + \frac{1}{2}\rho_{Air} V_{Wind}^2 \tag{8.5}$$

As the difference between internal and external static pressure increases considering higher values of z along the vertical, the scheme presented in Figure 88 (i.e. wind speed directed upwards and stagnation point located on the bottom of the balloon) is expected to generate the largest static pressure differential on the envelope (largest value on the top), thus representing a conservative assumption.

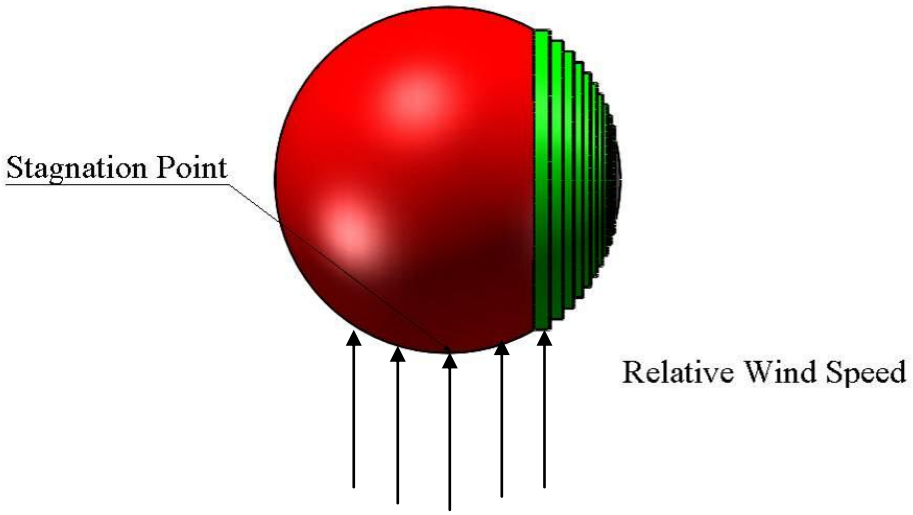

Figure 88 : External Envelope Load Assumption

As a first approximation atmospheric and helium densities can be assumed constant when considering higher values of z from the bottom to the top of the balloon. Under these assumptions and considering air and helium as ideal gases, the external and internal static pressures at the top of the balloon can be estimated as:

$$p_{Int}(\phi_B) = p_{Int}(0) - \rho_{Helium} \cdot \phi_B \cdot g \tag{8.6}$$

$$p_{Ext}(\phi_B) = p_{Ext}(0) - \rho_{Air} \cdot \phi_B \cdot g \tag{8.7}$$

where ϕ_B [m] is the balloon diameter. The difference between the static pressure at the top of the balloon is:

$$\Delta p_{TOP} = p_{Int}(\phi_B) - p_{Ext}(\phi_B) \tag{8.8}$$

acting outwards of the envelope, perpendicular to the surface and including the contribution of the dynamic pressure. Table 29 presents the values of Δp obtained for the bottom and the top of the 65 m diameter envelope for the different wind speeds calculated in section 3.2 (6000 m altitude). These values represent the static superpressure that needs to be provided in order to satisfy the non-dimpling condition at the stagnation point for the spherical balloon.

Wind Speed		Δp_{BOT}	Δp_{TOP}
$\overline{V_{Wind}}$	20.1 m/s	133.3 Pa	495.6 Pa
$\overline{V_{Wind}} + \sigma_{Wind}$	32.4 m/s	346.3 Pa	708.4 Pa
$\overline{V_{Wind}} + 2 \cdot \sigma_{Wind}$	44.7 m/s	659.1 Pa	1020.8 Pa
$\overline{V_{Wind}} + 3 \cdot \sigma_{Wind}$	57.0 m/s	1071.7 Pa	1432.9 Pa

Table 29 : Internal Superpressures for Different Values of Relative Wind Speed

However while the superpressure is compensated by the dynamic pressure component on the stagnation point, this doesn't happen elsewhere on the envelope surface. This means that the superpressure generates some stresses in the structure that the materials need to overcome. On one hand the superpressure is therefore necessary to maintain the shape of the external envelope while on the other hand it creates structural stresses in the membrane. These stresses need to be evaluated in this phase of the study in order to assess the viability of the non rigid structural solution.

Spherical Membrane Calculations

The first structural scheme concerns the spherical part of the envelope subjected to the internal pressure Δp_{TOP} shown in Figure 89a. As a conservative assumption the value of Δp_{TOP} shown in Table 29 is considered uniformly applied to the internal surface. The constant stress σ_{Sphere} generated in the membrane can be evaluated isolating a portion of the envelope, by cutting it along the equatorial plane as shown in Figure 89b.

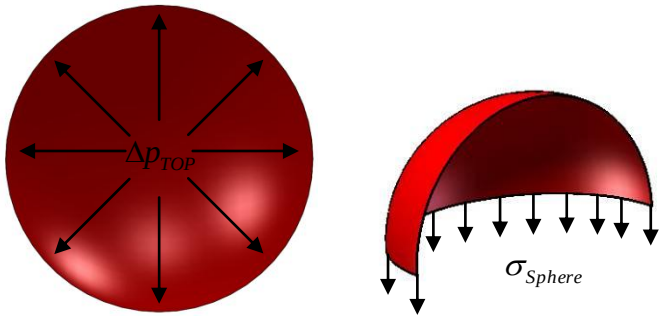

Figure 89 : Pressurised Spherical Envelope – Membrane Stress (Section View)

Considering the vertical direction (the reasoning is analogous for any direction) the force produced by the stress in the membrane must be in equilibrium with the total force produced by the superpressure acting on the internal surface. Assuming the thickness of the membrane small compared to the radius of the balloon, the equilibrium between the two forces can be written as:

$$2\pi \cdot t \cdot R_B \cdot \sigma_{Sphere} = R_B^2 \cdot \Delta p_{TOP} \cdot \pi \tag{8.9}$$

The equilibrium equation leads to the determination of the stress in the spherical envelope as:

$$\sigma_{Sphere} = \frac{R_B \cdot \Delta p_{TOP}}{2 \cdot t} \tag{8.10}$$

where R_B is the balloon radius and t is the envelope thickness. The envelope material resistance is expressed as a force over a length. In order to determine the margin of

safety (MS_{Sphere}) it is necessary to compare the product $\sigma \cdot t$ with the material characteristics. The material properties considered for the present calculations are relative to the laminate materials employed in state of the art lighter than air applications. A review of these material properties is included in Appendix B. On the base of the data collected, a reasonable value for the material resistance is set to 5.25 kN/50mm (500 g/m^2).

The margin of safety obtained for different values of the wind speed (and the relative superpressure calculated in the previous section) are summarised in Table 30. It should be pointed out that a superpressure of the lifting gas corresponds to an increase in the gas density. As a drawback the increased gas density causes a loss in the lift produced by the balloon which needs to be evaluated. The third column in Table 30 summarised the figures obtained.

Wind	MS_{Sphere}	$Lift_{LOSS}$
$\overline{V_{Wind}}$	13.0	0.04%
$\overline{V_{Wind}} + \sigma_{Wind}$	9.1	0.12%
$\overline{V_{Wind}} + 2 \cdot \sigma_{Wind}$	6.3	0.22%
$\overline{V_{Wind}} + 3 \cdot \sigma_{Wind}$	4.5	0.36%

Table 30 : Margin of Safety and Lift Losses Relative to Different Wind Speeds (Spherical Envelope)

Considering that the margin of safety to be taken into account is 4 [74] when working with fabric materials, the results show that the laminate material assumed for calculations will survive the superpressure required to maintain the shape if subjected to wind speeds up to $\overline{V_{Wind}} + 3 \cdot \sigma_{Wind}$. It must be noticed though that the employment of this kind of material is indeed necessary under the assumptions considered, as alternative materials currently is use (like coated fabric) wouldn't be able to resist the resulting stress. On the other hand it must also be pointed out that the dynamic behaviour of the balloon presented in section 7 is not taken into account and it could lead to lower speeds of the relative wind, considering the fact that the platform is usually moving dragged by the wind speed. The results obtained are therefore expected to be conservative and prove the technical feasibility of employing a pressurized spherical envelope.

8.2.2 PV Array Layout

As mentioned before the power output of a PV cell depends on the cosine of the angle between the solar beam and the surface of the device. Therefore an important task of the

PV array designer is to minimise the value of this angle during the operational life of the system. Ideally the system should be capable of performing the tracking of the Sun direction so that the solar beam is always perpendicular to the surface of the solar cells. However in many terrestrial applications the designer sets a constant value for the orientation of the solar array depending on the geographical location of the system, in order to optimize the overall energy production, limiting at the same time the cost of installation.

In both cases (with or without the Sun tracking mechanism) it is necessary to guarantee that the orientation of the solar cells is the same for all the devices, i.e. the PV cells need to be pointing towards the same direction. A series of rigid lightweight annular plates is therefore employed as a substrate to attach the devices to the external envelope surface and compensate for the curvature of the spherical balloon.

Different issues are involved in the choice of the PV layout and in the sizing of the rigid plates. These issues are related to the optimization of the system power output and to aerodynamic and structural constraints. The following analysis is aimed at the definition of a number of annular plates (steps) on which the cells are mounted in order to identify a suitable layout for the PV arrays. The structural sizing of these annular plates will be presented in the following sections.

First of all, although an optimization of the system power output would require all the cells to be attached to the flat plates, the need of reducing the aerodynamic drag of the structure implies that some of the PV devices can actually be located on a rigid spherical nose. The first constraint is therefore represented by the size of this spherical cap which implies that the cells located at the external edge are not directed towards the direction of the sun, even when the pointing mechanism has no error (Figure 90). Assuming the maximum power loss due to this reason is 5%, as the output of the solar cell is dependent on the cosine of the incidence angle, the maximum angle between the horizontal and the edge of the spherical cap is given by:

$$\alpha_{Max} = \cos^{-1}(0.95) = 18.2^{\circ} \tag{8.11}$$

The maximum edge angle of the spherical cap (Figure 90) must be less than 18.2° in order to limit the power losses due to the misalignment of the cells. For the following calculations a target around 15° is set.

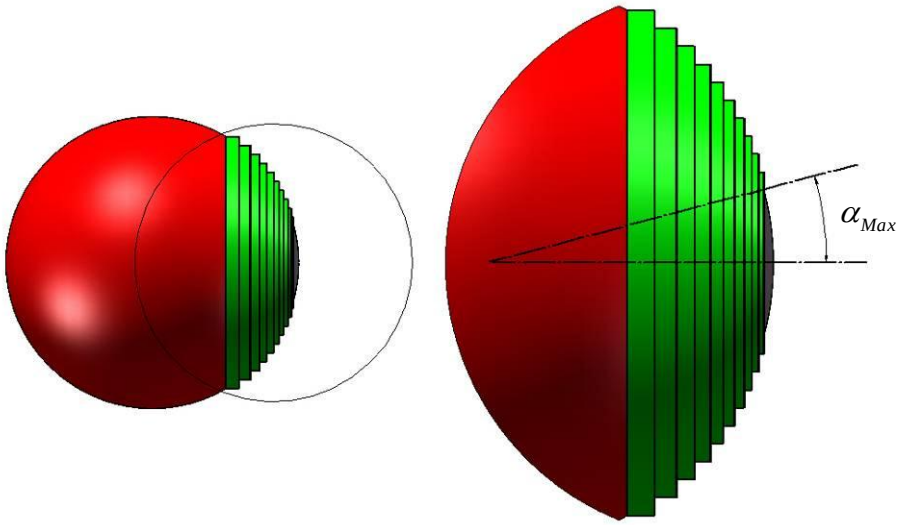

Figure 90 : Angle between Horizontal Direction and Edge of the PV Cells Spherical Cap

Another problem to be considered is the possible accuracy of the pointing mechanism and its influence on the shadow of the PV array due to the stepped structure. The problem is schematically presented in Figure 91. The accuracy of the pointing mechanism has a direct influence on the angle of incidence that can be expected which can cause part of the array to be in shadow.

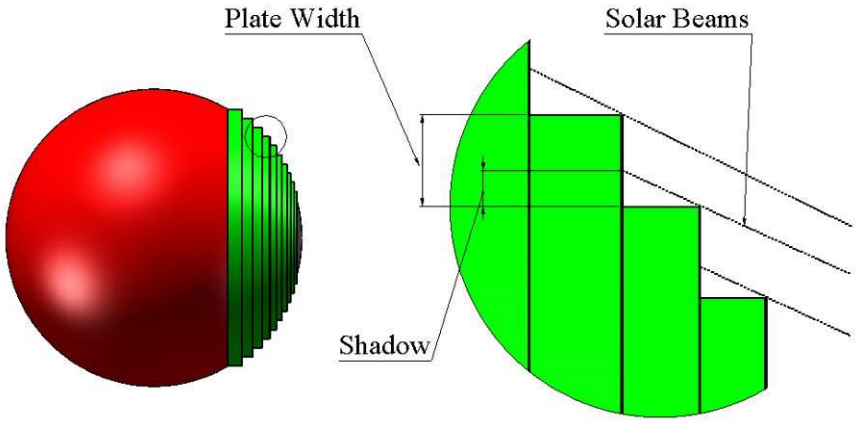

Figure 91 : Shadow effect due to stepped structure

Setting the accuracy of the pointing mechanism to 5˚, the amount of shadow surface can be determined as a function of the number of rigid plates employed and a corresponding value of the plate's width (assumed constant). As an example Table 31 shows the results obtained for the case of 10 annular plates (2m width). Plates are numbered starting from the spherical cap and the first plate right next to the spherical cap is assumed not to be shaded. The figures presented concern the amount of shaded area for each panel, expressed as a percentage of the total annular surface and they are obtained assuming a constant value for the accuracy of the pointing mechanism. This situation represents indeed the worst case scenario, as the misalignment of the solar beam is expected to be

at most equal to the accuracy value. During the operational life of the generator the angle value is expected to vary between zero and this maximum limit. The values presented show an increment of the portion of shaded area obtained as larger plates are considered. This is due to the fact that the height of the step increases going from plate 2 to 10, while the plate width is kept constant. The average value is around 2% of the total plate surface.

Plate Number	Perc Area Shadow
1	-
2	0.74%
3	0.94%
4	1.15%
5	1.38%
6	1.64%
7	1.94%
8	2.29%
9	2.72%
10	3.29%
Average	1.79%

Table 31 : Shadow Values due to Pointing Accuracy

However it is necessary to point out that the value chosen for the total number of flat rigid plates must constitute a trade-off between the optimization of the power output and aerodynamic (and structural) issues. Generally speaking a reduced number of annular plates leads to a smaller value of the shadow area, the limit case being a single surface which wouldn't have any shadow at all. On the other hand a high number of steps in the structure allows the external shape to be more similar to a sphere. This is expected to be beneficial from an aerodynamic point of view, reducing the moments and the drag of the system and, as a consequence, the external loads (due to the winds) on the structure.

Number of Plates	Plate Width [m]	Edge Angle [deg]	Shaded Surf [%]
5	4	14.5	1.53
6	3.3	14.9	1.62
7	2.8	14.6	1.67
8	2.5	14.5	1.72
9	2.2	14.9	1.77
10	2	14.5	1.79
11	1.8	14.9	1.83
12	1.6	14.9	1.85
13	1.5	14.8	1.87
14	1.4	14.6	1.88
15	1.3	14.7	1.90

Table 32 : Shadow Values Comparison for different Annular Plates Numbers

In Table 32 different solutions are compared, which employ a number of annular plates between 5 and 15. The figures compared concern the width of the plate, the edge angle of the spherical cap and the average value of the shaded surface. For the moment a value of 10 annular plates seems a good compromise between the need of reducing possible power losses due to the shaded area and the aerodynamic and structural problems that may arise.

8.2.3 PV Array Support Structure

This section addresses the preliminary design of the components introduced to support the PV array. These are constituted by the annular plates mentioned in the previous section and by the stepped structure shown in Figure 86. In particular the design of the stepped structure is addressed considering two different technical solutions, the first one employing a rigid frame externally attached to the spherical envelope and the second one employing a series of cylindrical pressurised membranes.

Non Pressurised Stepped Structure

The analysis presented in this section concerns the solution in which the stepped structure is constituted by an external frame (non pressurised) attached to the spherical envelope. The solution is presented in Figure 92.

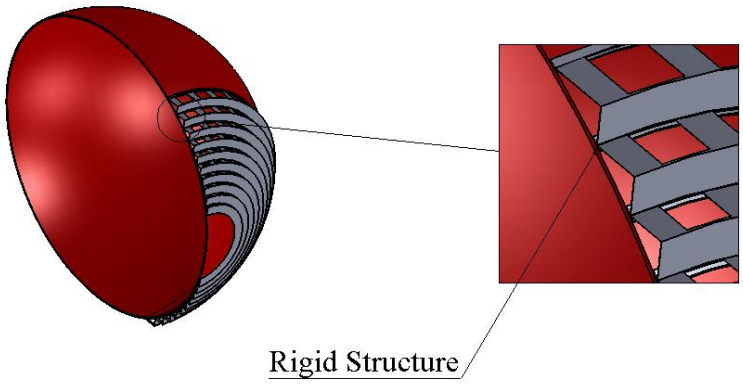

Figure 92 : PV Support – External Rigid Frame

The dynamic pressure is assumed acting on the arrays' surface and the loads are transmitted through the frame to the pressurised spherical envelope generating a concentrated load on the membrane which can constitute an issue for the feasibility. Therefore the design driver in this case is the distribution of the loads on the fabric. The resulting external pressure must be at most equal to the internal gas superpressure in order to avoid the dimpling conditions and possible failure of the membrane. As a

conservative assumption the internal superpressure in this case can be assumed equal to the dynamic pressure contribution 1071.7 Pa (Δp_{BOT} at $\overline{V_{Wind}} + 3 \cdot \sigma_{Wind}$ - Table 29) acting on the array surface. The loads conditions are shown in Figure 93.

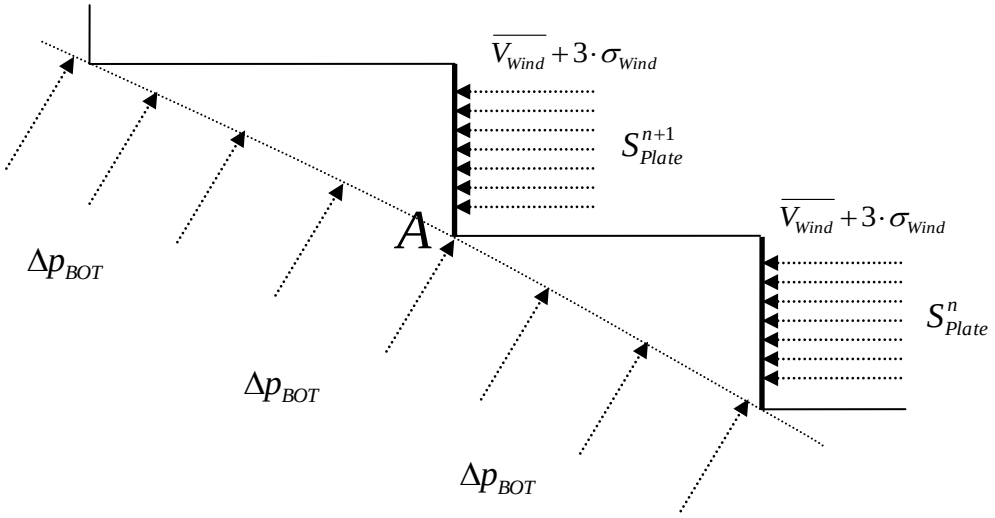

Figure 93 : External Frame Loading Conditions

Each of the annular plates that constitute the substrate for the PV array, can be considered as simply supported by the frame structure. As a first approximation the total force acting externally on the spherical membrane at the generic point A in Figure 93 can be calculated as:

$$F_A^n = \frac{p_{Dyn}}{2} S_{Plate}^n + \frac{p_{Dyn}}{2} S_{Plate}^{n+1} \tag{8.12}$$

where p_{Dyn} is the dynamic pressure value and S_{Plate} refers to the surface of the rigid annular plate.

In order to be able to distribute effectively this force over the membrane, it is necessary to include a solid clad along the circular interface with the spherical envelope. The value of the interface area for non-dimpling conditions can be evaluated by imposing the equilibrium at the interface as presented in Figure 94. Assuming the solid clad to be flat (actually it will be a spherical segment), the width required for the equilibrium to be satisfied is 2 m (i.e. between 30% and 150% of the distance between the steps).

State of the art materials can be used to reduce significantly the mass of the rigid frame. However, considering the value determined for the clad width, the total contribution of this component to the overall budget is expected to be significant.

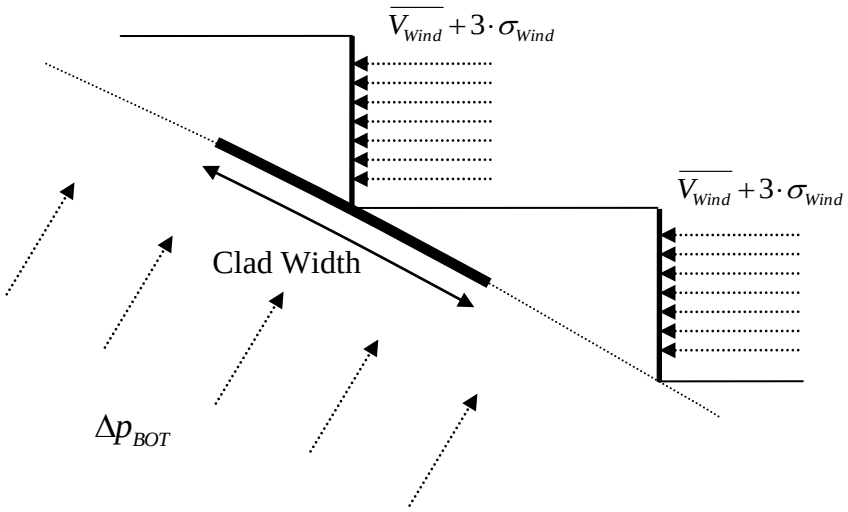

Figure 94 : Equilibrium at Interface

As a first estimate, assuming a carbon fibre sheet of 5 mm thickness, the mass obtained is 16.4 T only for the solid clad at the interface (support frame not included) which represents around the 17% of the total buoyancy. The drawback in terms of added mass is evident. Moreover the design of a rigid support frame is expected to add a certain degree of complexity to the overall design. A detailed design of the components is beyond the scope of this analysis. However, based on these considerations, it seems more reasonable at this stage of the research to investigate an alternative technical solution, which doesn't need to include a rigid frame in the design.

Pressurised Stepped Structure

The alternative solution employs a series of cylindrical membranes pressurised with the same level of superpressure used for the spherical envelope. Moreover each cylindrical membrane is assumed to be internally constrained by another membrane which is not pressurised. The solution is presented in Figure 95.

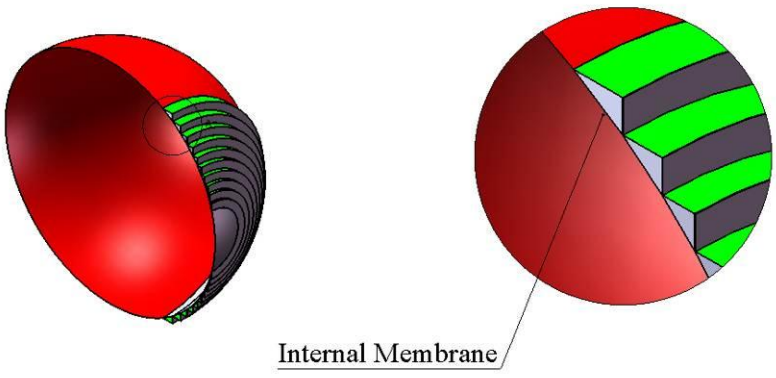

Figure 95 : PV Support – Pressurised Cylindrical Membranes and Internal Membranes

While in the case of the sphere the stress is the same no matter which direction is considered, in the case of a cylinder it is necessary to calculate the values of the two principal stresses, i.e. in the longitudinal and hoop directions by imposing two different equilibrium equations. Considering the hoop stress, the internal membranes are not expected to have any effect in this direction. It is therefore possible to isolate a single pressurised membrane as shown in Figure 96 and write the equilibrium in the transverse direction (per unit of length of the cylinder) as:

$$2 \cdot t \cdot \sigma_{Cylinder}^{Hoop} = 2R_C \cdot \Delta p_{TOP} \tag{8.13}$$

where R_C is the radius of the cylindrical membrane. Rearranging this equation, the expression for $\sigma_{Cylinder}^{Hoop}$ becomes:

$$\sigma_{Cylinder}^{Hoop} = \frac{R_C \cdot \Delta p_{TOP}}{t} \tag{8.14}$$

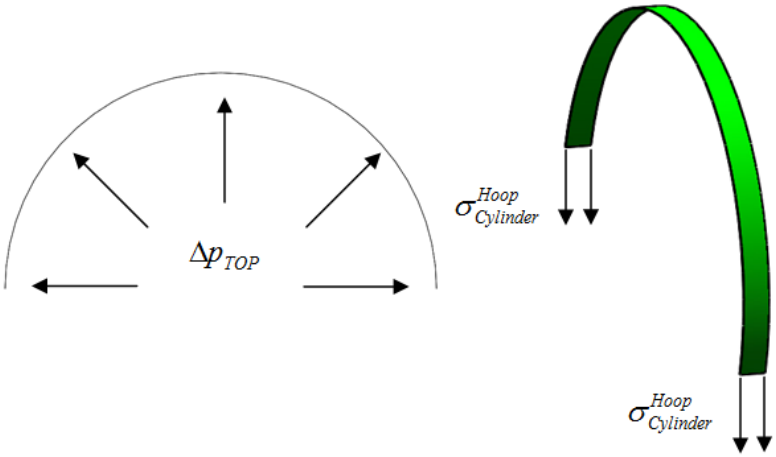

Figure 96 : Cylindrical Membrane Hoop Stress

As the stress value is proportional to the radius of the cylinder, the maximum stresses are obtained for the largest maximum radius (28.15 m) which leads to the margins of safety listed in Table 33 (evaluated for the material properties assumed for the spherical envelope).

Wind	$MS_{Cylinder}^{Hoop}$
$\overline{V_{Wind}}$	7.5
$\overline{V_{Wind}} + \sigma_{Wind}$	5.3
$\overline{V_{Wind}} + 2 \cdot \sigma_{Wind}$	3.6
$\overline{V_{Wind}} + 3 \cdot \sigma_{Wind}$	2.6

Table 33 : Margin of Safety relative to Different Wind Speeds (Cylindrical Envelope – Hoop Stress)

The figures obtained demonstrate that for high wind speeds the margin of safety drops to a value of 2.6 in the case of the hoop stress, which wouldn't be acceptable for the design. The results suggest therefore that the cylindrical surface would break with a tear propagating along the longitudinal direction as a result of the internal pressure applied. Different technical solutions can be evaluated in order to address this problem, including the possibility of employing some internal rigid stiffeners to help preventing any damage to the membrane. In this preliminary phase it seems reasonable to assume that the fabric can be locally reinforced, for example by doubling the thickness of the cylindrical surfaces in order to get acceptable figures for the margin of safety. By doing that the worst case safety factor would increase to a value of 5.2, although at the same time the envelope would become heavier in those regions. Considering the size of the regions, the increased mass is expected not to be significant, compared to the overall mass of the system.

Concerning the cylindrical membrane stress in the longitudinal direction, this has to be evaluated together with the stress values in the internal non pressurised membrane. The schematic representation in Figure 97 shows a section view of two following steps, including the internal membrane.

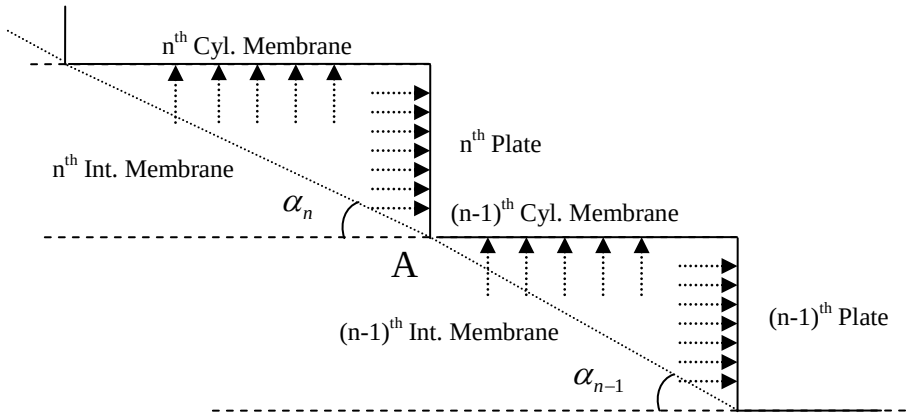

Figure 97 : Schematic Representation for Analytical Calculations

The superpressure is assumed to act on the internal surface of the cylindrical membranes and of the rigid annular plates, while the internal membrane is assumed to be not pressurised. As a first approximation the force in each internal membrane can be calculated by imposing the equilibrium equation at the interface between the different structural components. For example the forces acting at point A in Figure 97 are assumed to be:

- The force in the n^th internal membrane, $F^{n}_{IntMembr}$.

- The force in the n-1th internal membrane, $F_{IntMembr}^{n-1}$.
- The longitudinal component of the force in the n-1th cylindrical membrane, $F_{CylMembr}^{n-1}$, which is assumed to be equal to one half of the total force due to the pressure acting on the n-1th plate, i.e. $F_{CylMembr}^{n-1} = \frac{\Delta p}{2} S_{Plate}^{n-1}$.
- One half of the total force $\frac{\Delta p}{2} S_{Plate}^{n}$ acting on the nth plate.

Actually the calculation starts from the internal membrane attached to the edge of the spherical cap. In this case the equilibrium imposed is between the stress in the first membrane, and the pressure acting on the first annular plate and the cap. The value obtained for $F_{IntMembr}^{1}$ is then used to work out the values relative to the other membranes both internal and cylindrical. The stresses are then derived from the forces, introducing the values of the radius of the membrane and the fabric thickness as:

$$\sigma_{IntMembr}^{n} = \frac{F_{IntMembr}^{n}}{2\pi \cdot R_n \cdot t} \tag{8.15}$$

$$\sigma_{CylMembr}^{n} = \frac{F_{CylMembr}^{n}}{2\pi \cdot R_n \cdot t} \tag{8.16}$$

where $\sigma_{CylMembr}^{n}$ refers to the longitudinal stress. It must be noticed that under the current assumptions the radius R_n is variable for the internal membrane as the section increases going from the (n-1)th to the nth plate, reducing the value of the stress. The figures obtained for the margins of safety for the two membranes are presented in Table 34. The values are relative to the superpressure obtained for $\overline{V_{Wind}} + 3 \cdot \sigma_{Wind}$.

Membrane	$MS_{CylMembr}^{n}$	$MS_{IntMembr}^{n}$	
1	81.3	4.9	4.0
2	79.9	4.9	4.1
3	78.9	4.8	4.1
4	78.1	4.8	4.2
5	77.6	4.8	4.2
6	77.1	4.7	4.3
7	76.7	4.7	4.3
8	76.4	4.7	4.3
9	76.2	4.7	4.3
10	76.0	4.7	4.3

Table 34 : Margins of Safety for Internal Membranes (Min and Max Values) and Cylindrical Membranes

Annular Plates Calculations

Having evaluated the stress values in the membranes, it is now important to address the design of the rigid annular plates. The outputs evaluated for these components concern not only the structural stresses but also the displacements and rotation caused by the application of the distributed pressure. As the plates provide the support for the solar cells, it is important to limit the rotation of the external surface on which the devices are mounted for the reasons already described before. As the final result of the analysis has to be an estimate of the mass of these components, specific power figures ([W/kg]) previously derived from literature are revised on the base of considerations about the materials employed and of the results obtained from structural calculations.
The material chosen for the rigid plates needs to be stiff enough to withstand the internal pressure but at the same time it needs to be lightweight to limit the overall mass value. These characteristics can be found in different materials used in the aerospace sector. In particular sandwich panels are widely employed due to the significant advantages of these materials especially in terms of low weight and stiffness which make them particularly suitable for aerospace applications. For the rigid panels of the AEPG, a sandwich panel constituted by an internal core of aluminium honeycomb between two epoxy/carbon fiber composite layers is chosen. A schematic representation of the internal structure of the sandwich panel is shown in Figure 98 while the mechanical properties of the epoxy/carbon fiber material (assumed isotropic) and of the honeycomb core are summarised in Table 35 and Table 36.

Figure 98 : Schematic Representation of a Sandwich Panel

Some preliminary calculations can be performed to evaluate the displacements, rotations and stresses of the plates depending on the values set for core and skin thickness. These calculations are based on the relations developed for the flat plates in [137] which are derived from the elastic beam theory, and on the guidelines provided by HexWeb [138] which has an extensive expertise in the design and manufacture of

honeycomb sandwich panels. The calculations involve some assumptions due to the employment of this particular material that are here summarised.

Elastic Modulus [MPa]	200e3
Poisson's Ratio	0.3
Ultimate Stress [MPa]	600
Density [kg/m^3]	1600

Table 35 : Epoxy/Carbon fiber composite properties

Elastic Modulus [MPa]	165
Shear Modulus (L) [MPa]	110
Shear Modulus (W) [MPa]	55
Compression Strength [MPa]	0.90
Shear Strength (L) [MPa]	0.65
Shear Strength (W) [MPa]	0.40
Density [kg/m^3]	29

Table 36 : Aluminium Honeycomb properties

The bending stiffness of a sandwich plane can be determined considering the thickness of core and skins (t_c and t_f respectively) shown in Figure 98 under the assumption $t_c >> t_f$:

$$D = \frac{E_c}{1-\nu_c^2} \cdot \frac{t_c^3}{12} + 2 \cdot \frac{E_f}{1-\nu_f^2} \cdot \frac{t_f^3}{12} + 2 \cdot \frac{E_f}{1-\nu_f^2} \cdot \frac{t_c^2}{4} t_f \tag{8.17}$$

where E_c and E_f are the Young moduli and ν_c and ν_f are the Poisson ratios of core and skins respectively. The first two terms on the right hand side of the equation are significantly smaller than the third one and the expression can be simplified as:

$$D \cong \frac{E_f}{1-\nu_f^2} \cdot \frac{t_c^2}{2} t_f \tag{8.18}$$

The value of the bending stiffness obtained with this expression can be introduced in the relations developed for annular plates in [137] and calculate the displacements and rotations, given a defined set of constraints for the internal and external edge do the plate. Moreover the maximum value of the stress due to the bending moment is obtained in a sandwich plate for the external carbon fibre skins. From the beam theory adapted to the particular case of a flat plate, the stress in the skins can be determined as:

$$\sigma = \frac{E_f}{1-\nu_f^2} \cdot \frac{M}{D} \cdot \frac{t_c}{2} = \frac{M}{t_c \cdot t_f} \tag{8.19}$$

The exploratory calculations consider two different thickness ranges for the honeycomb core and the composite skins. These values, relative to materials commonly employed in aerospace applications, are presented in Table 37.

Core Thickness [mm]	15-30
Skin Thickness [mm]	0.5-1.0

Table 37 : Sandwich Beam Parameters

The presence of the internal membrane creates a support along the internal edge of each plate which constraints the displacements and releases the rotations. The schematic representation of the new constraints is shown in Figure 99. The deformed shape has a maximum in the middle of the plate and the maximum rotations for the internal and external edges as presented in Figure 100 in the case of a core thickness 20 mm of and a skin thickness of 1 mm.

Figure 99 : Constraints and Loads Applied (Supported- Supported)

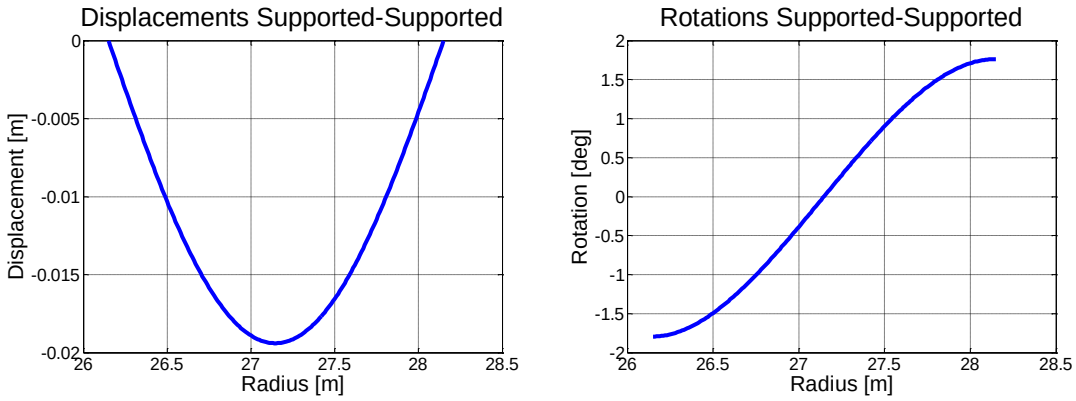

Figure 100 : Deformed Shape and Rotations (Supported-Supported Edges)

The results presented in Table 38-Table 40 show the significant effect that the introduction of the internal membranes brings in terms of displacements and rotation angles. The angle values vary between 0.78˚ and 6.27˚ while the displacements range is between 9 mm to 6.9 cm.

Even in the worst conditions, the angle obtained would affect the output of the solar cells reducing the total value by about 0.01%, which doesn't seem to represent a significant issue for the viability of the AEPG. However in this phase it is important to take into account possible inaccuracies deriving from the simplifying assumptions introduced in the calculations. Moreover the results obtained need to be compared to the preliminary values set during the exploratory calculations in section 5.3. Therefore it is more reasonable not to choose the smallest values for skins and core thicknesses, but to add some considerations about the mass values of the different solutions presented, in

order to find a suitable trade-off between the total weight of the PV array and its performance.

Rotations [deg]					
		Core			
		15	20	25	30
Skin	0.5	6.27	3.53	2.26	1.57
	0.75	4.18	2.35	1.50	1.04
	1	3.13	1.76	1.13	0.78

Table 38 : Rotations for Supported- Supported Edges (3 Sigma Wind Speed)

Displacements [m]					
		Core			
		15	20	25	30
Skin	0.5	0.069	0.039	0.025	0.017
	0.75	0.046	0.026	0.017	0.011
	1	0.034	0.019	0.012	0.009

Table 39 : Displacements for Supported- Supported Edges (3 Sigma Wind Speed)

Stress [MPa]					
		Core			
		15	20	25	30
Skin	0.5	95.49	71.62	57.30	47.75
	0.75	63.66	47.75	38.20	31.83
	1	47.75	35.81	28.65	23.87

Table 40 : Skin Stress for Supported- Supported Edges (3 Sigma Wind Speed)

As already explained the sandwich panel is the substrate which will be employed to support the solar cell blanket. Considering a figure of 0.7 kg/m^2 relative to high efficiency silicon [139] cells and a penalty factor of 1.3 to take account for the presence of cables, diodes and other electrical components, the total PV mass is evaluated in Table 41.

PV Array Mass [kg]					
		Core			
		15	20	25	30
Skin	0.5	8841.6	9307.6	9773.6	10239.7
	0.75	11430.6	11896.7	12362.7	12828.7
	1	14019.7	14485.7	14951.7	15417.8

Table 41 : PV Array Mass

The figures presented show a possible mass range between 8,841.6 kg and 15,417.8 kg which can be compared to the first estimate provided in order to evaluate possible discrepancies. The increments are between the 36.6% to the 138.2% respect to the mass evaluated previously. Considering the sensitivity analysis described in section 6.4 an increment of about 50% is not expected to significantly affect the system, both in terms of balloon final position and free lift value. Based on these results, a thickness of 25 mm for the honeycomb core and a thickness of 0.5 mm for the two carbon fiber skins are

selected, which would lead to a rotation of about 2.26˚ and a total maximum displacement of 2.5 cm. The results relative to these thicknesses are summarised in Table 42.

Core Thickness [mm]	25
Skin Thickness [mm]	0.5
Displacement [m]	0.025
Rotation [deg]	2.26
PV Array Mass [kg]	9773.6

Table 42 : PV Array Design Parameter

FEM Models

As the analytical calculations are based on different simplifying considerations, it is important to compare the results obtained with the output of a finite element model simulation in order to gain more confidence of the final results. The FEM simulates the static response of the envelope when subjected to the internal pressure. Since the structure is axis symmetric it is possible to model a quarter (Figure 101) and apply symmetry constraints along the edges.

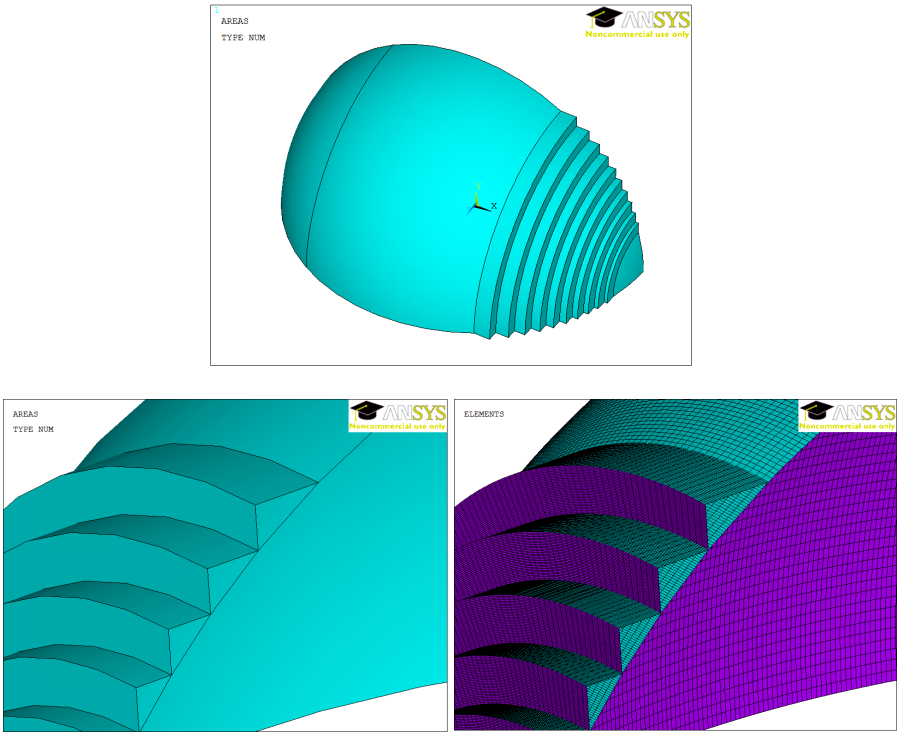

Figure 101 : FEM of the Pressurised Envelope

The membranes are modelled using shell63 elements which can be employed to simulate the mechanical characteristics of fabric materials. The material properties introduced for the membranes are relative to the polyester fabric used for previous calculations (with a thickness 0.2mm and an elastic module of E=10GPa [145], [109]).

The rigid annular plates and the spherical cap are modelled with the same shell63 elements. However the material properties introduced in this case, are the ones determined for the honeycomb/carbon sandwich.

In the analytical calculations presented above different structural schemes are introduced separately (spherical envelope, cylindrical and internal membranes, annular plates). It is important to notice though that these simplified models can have some problems in quantifying the structural stresses along the interfaces. While the interfaces between the membranes and the rigid plates are not expected to have any problems in terms of structural stiffness, on the contrary some structural problems may arise where the spherical membrane meets the largest cylindrical membrane (Figure 102).

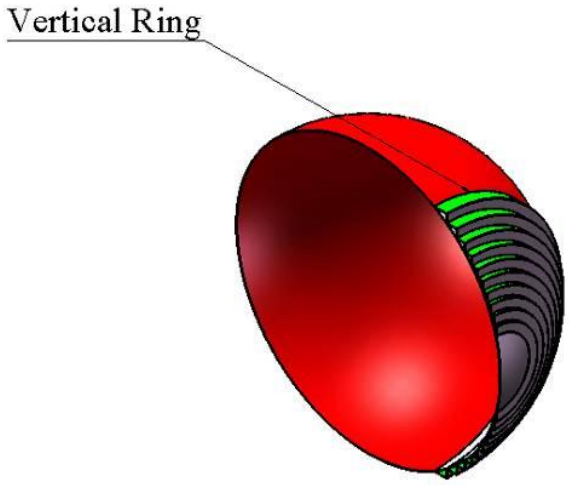

Figure 102 : Composite Vertical Ring

A ring of carbon/epoxy material is therefore modelled with beam4 elements and added to the structure where the spherical part meets the largest cylindrical membrane. The beam section is assumed to be circular with a diameter of 5 cm.

As mentioned before the analysis needs to be particularly focused on the stress in the cylindrical membranes and in the internal supports. Starting from the internal membranes, Figure 103 shows the comparison between the stress results obtained with analytical calculations (max and min for each membrane) and the ones determined by the FEM. The discrepancies are below 5% which don't represent a significant problem for the margins of safety determined before. Analogous considerations can be inferred looking at the results on the cylindrical membranes, where the discrepancies reach values around 3% (Figure 104).

As mentioned during the analytical calculations the hoop stress in the cylindrical membranes might be critical for the structural integrity of the envelope. The results

presented for the simplified case of an inflated cylinder have highlighted the need of increasing the thickness of the fabric of the envelope in those regions to withstand the stress. The FEM model confirms those results as presented in Figure 105. It is therefore necessary to consider in the weight budget determination, the contribution coming from the increased thickness of the cylindrical membrane.

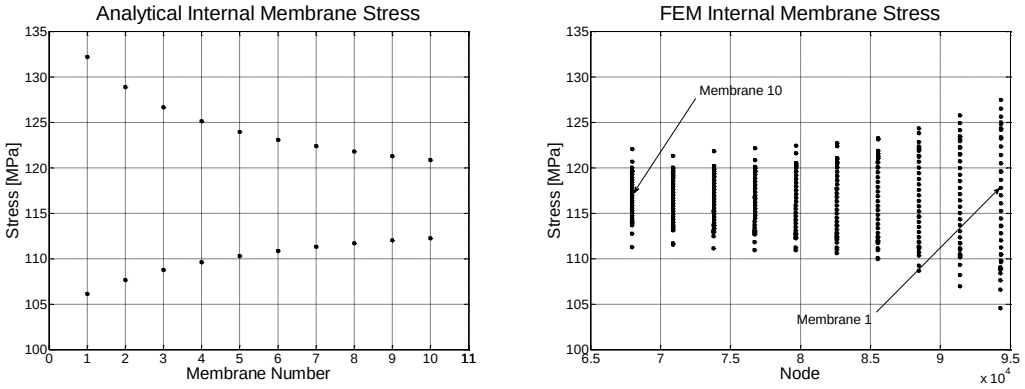

Figure 103 : Comparison Internal Membrane Stress (Analytical - FEM)

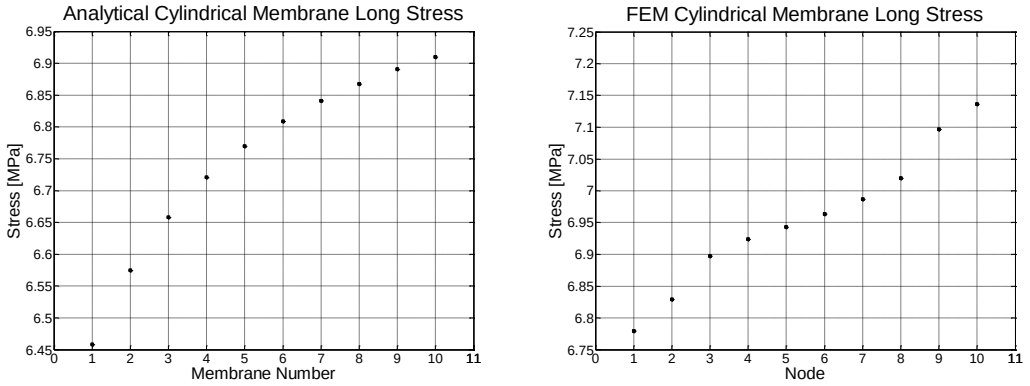

Figure 104 : Comparison Cylindrical Membrane Long Stress (Analytical - FEM)

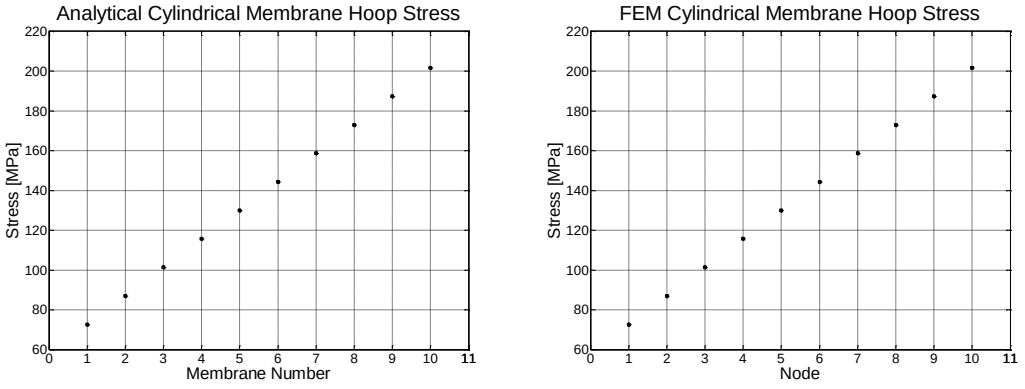

Figure 105 : Comparison Cylindrical Membrane Hoop Stress (Analytical - FEM)

Another useful result concerns the displacements and rotations of the rigid plates supporting the PV panels. The analytical calculations assumed an annular plate simply supported along both the internal and external edges to simulate the effect of the internal membrane. This assumption is extremely simplified as the two edges are not perfectly

fixed and some displacement is here allowed, i.e. the plates edges constraints are somewhere in between the supported-guided and the supported-supported conditions. These constraints can lead to a deformed shape different from the one presented in Figure 100. The deformed shapes obtained for plate 1, 6 and 10 are shown as an example in Figure 106, while the maximum displacements and rotations are presented in Figure 107. As expected, the values are higher than the ones evaluated analytically even though the maximum value obtained for the rotations (i.e. around 4.5˚ for plate 1) is expected to affect the power produced by less than 0.5%. Conclusions about the impact that these values will have on the performance of the PV cells remain substantially unchanged.

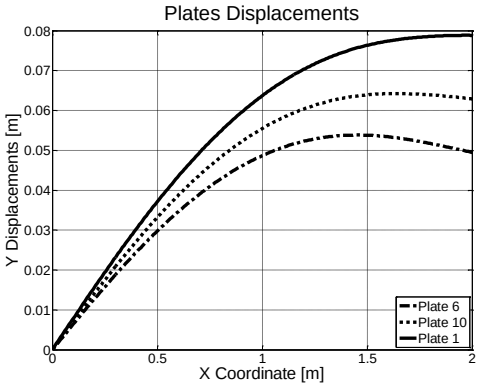

Figure 106 : Plates Displacements (FEM)

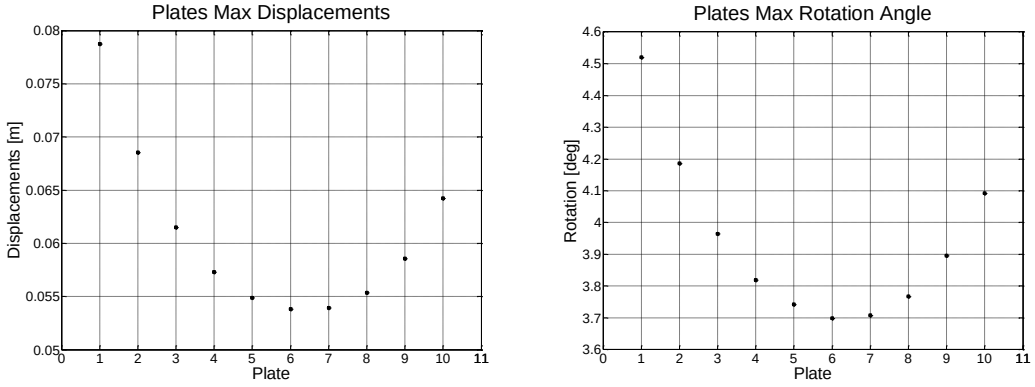

Figure 107 : Maximum Plates Displacements and Rotations (FEM)

The results obtained highlight the importance of performing FEM simulations. Even though the simplified analytical calculations are confirmed, the additional analysis is useful to gain more confidence about the viability of the concept presented. In this sense the finite elements provide added value to the quality of the assessment of the technical feasibility of the AEPG.

8.2.4 Subsystems Interface and Load Supports

One of the technical challenges that need to be addressed during the design of a LTA vehicle is the possible concentration of loads on the envelope which can result in the local damage of the fabric and consequent leaks of lifting gas or even total failure of the vehicle. Therefore the preliminary analysis of the structural layout of the AEPG is completed introducing the elements responsible for the distribution of the mechanical loads due to the mass contributions of the different subsystems all over the surface of the external envelope.

These elements are constituted by two series of fabric strips both running along the upper hemisphere of the envelope and an equatorial rigid ring as presented in Figure 108. Moreover the figure shows a rigid case located on the back part of the AEPG. This case is employed to house some of the subsystems already mentioned in section 5.4.2 (inverter and transformer) and some others which will be described in section 8.3. The introduction of this case allows taking into account another important issue, i.e. the inertial characteristics of the system and in particular the location of the centre of mass with respect to the centre of buoyancy.

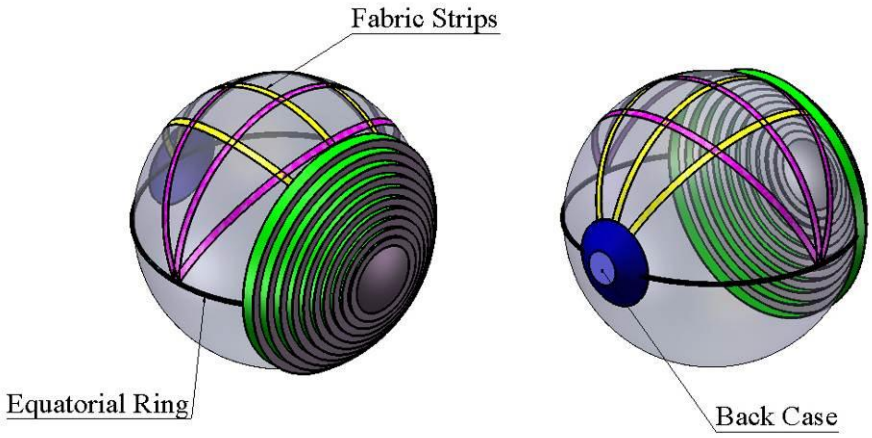

Figure 108 : Strips, Equatorial Ring, Back Case

In particular two sets of fabric strips are introduced. The first set (highlighted in purple in Figure 108) is assumed to be attached at two opposite points along the equator which constitute the interface with the mooring tether. The second set of strips (highlighted in yellow in Figure 108) is attached to the back case and to the vertical ring at the interface between the spherical envelope and the largest cylindrical membrane. Both sets are constituted by 3 strips, a central one and two side ones at an angle of 30 deg. The main requirements that these elements have to comply with are the effective distribution of

the mechanical loads in order to avoid possible concentrations and the resistance of the strips' fabric.

The analysis is performed employing the FEM model shown in Figure 109, which simulates the static response of a set of 3 fabric strips assumed to be supported by a spherical surface. This is simulated in the model by imposing the constraints to the node in spherical coordinates. Moreover the top end is assumed to be pinned as the fabric strip is symmetric and the load is applied to the lower end. Each strip is divided into 104 nodes (each element has a length of 0.5 m) and modelled in Ansys with link elements. As the mass parameter needs to be kept to a reasonable limit, Kevlar is taken into account for the material properties.

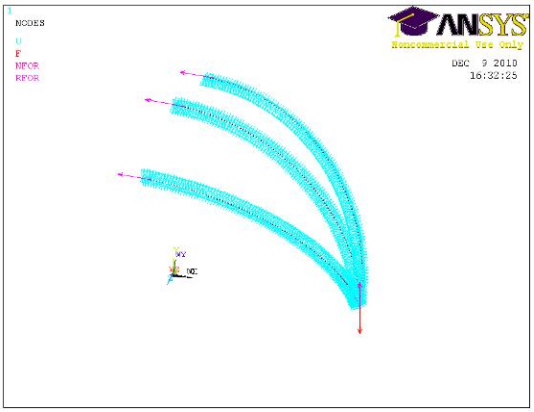

Figure 109 : FEM Model Fabric Strips

The load applied is mainly derived from the tether tension resulting from the aerostatic/dynamic forces acting on the balloon and evaluated in section 6. As a worst case scenario, the tether tension which is expected to represent the largest load applied is increased in order to take into account for the additional effect of the weight of the different components. The total force of 333.5 kN is split between the two joint located on two opposite sides along the equator. The resulting force of 166.75 kN (around 17 T) is increased to 200 kN and applied to the strips modelled in the FEM of Figure 109.

The results considered are:

1. The displacement of the lower node as a result of the deformation of the strips
2. The internal stresses of the strips
3. The resulting pressure distribution on the spherical envelope

All these results need to be contained for the concept to be feasible. In particular the resulting pressure distribution on the spherical envelope is evaluated with the reaction forces determined by the FEM which are assumed to be spread over the strip surface. The resulting pressure needs to be at most equal to the internal super-pressure not to

cause any dimpling of the fabric. The thickness of the strip is fixed to 0.5 mm and the width is then determined based on the internal super-pressure value. The reaction force calculated for the central strip is considered as this strip is expected to carry the most of the load. For the central strip the reaction calculated is 1220 N (max value), directed towards the centre of curvature of the strip. Considering this force distributed on an element of length 0.5 m, the width can be determined assuming the external pressure equal to the internal superpressure (1432.9 Pa), leading to a strip width of 1.7 m.
The results concerning the internal stress and the displacements are presented in Figure 110. The total mass of Kevlar required for the 3 longitudinal strips and the 3 lateral strips is estimated as 630.3 kg.

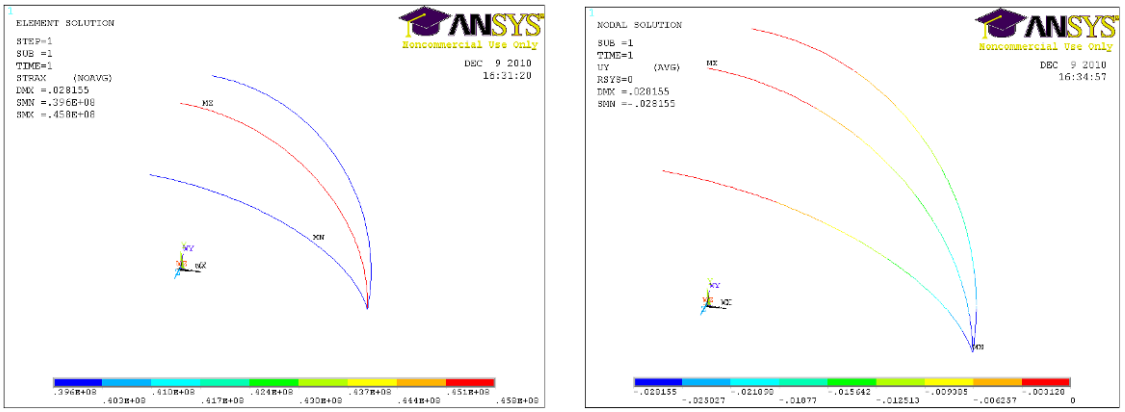

Figure 110 : FEM Model Strips - Results

As the mechanical loads (tether tension and subsystems weight) are concentrated on the strips attachments, the equatorial ring is not expected to carry much load, but only to contribute to the overall stiffness of the structure. Therefore its mass contribution is not expected to be significant and some preliminary values can be assumed on the base of sound engineering judgment. A rectangular 0.3x0.3 m section with a wall thickness of 3 mm would lead to an overall mass of 347.6 kg in the case of a carbon fibre reinforced plastic.
Finally the back case is intended not only to protect the subsystems from the external environment but also to provide an aerodynamic shape which can reduce the aerodynamic drag. The detailed design of the shape of this component requires aerodynamic simulations which go beyond the purpose of this study. For the moment the case is assumed to be a cone shaped rigid shield made of lightweight material with an internal base attached to the equatorial ring and the second series of strips.
The conic shield just needs to provide an aerodynamic surface and it is not expected to be subjected to significant mechanical loads. On the other hand the internal base is

expected to require some structural properties as it needs to constitute an interface between the fabric strips, the equatorial ring and the subsystems. Therefore, considering carbon fibre reinforced plastic as in the case of the equatorial ring, a first figure for the total mass of this component can be set to about 3 T assuming the parameters summarised in Table 43.

Base Radius [m]	6.75
Base Height [m]	1
Base Wall Thickness [mm]	5
Conic Surface [m^2]	367.5
Conic Wall Thickness [mm]	1

Table 43 : Back Case Parameters

8.3 Gas Pressure Control System

While the AEPG ascends to operational altitude the external atmospheric pressure and density change as a function of the height above the ground. Therefore the system must be able to adjust the pressure and density of the internal gas in order to maintain the fixed value of superpressure determined in section 8.2, through the introduction in the design of a pressurization system. This subsystem consists of a membrane located internally of the envelope (ballonet) that can be inflated and deflated with atmospheric air by one or more electrically powered blowers connected to a combination of ducts and valves. The internal ballonet is schematically represented in Figure 111 when the AEPG is on the ground, i.e. with the membrane fully inflated. During the ascent the ballonet is deflated until it reaches the configuration at pressure height shown in Figure 112.

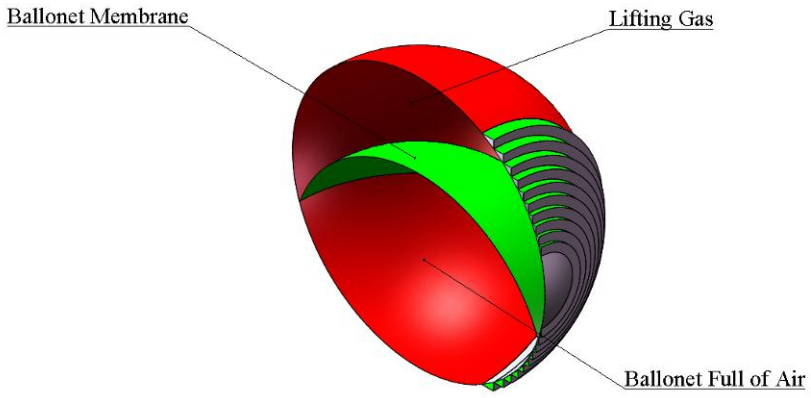

Figure 111 : Ballonet Fully Inflated – AEPG on Ground

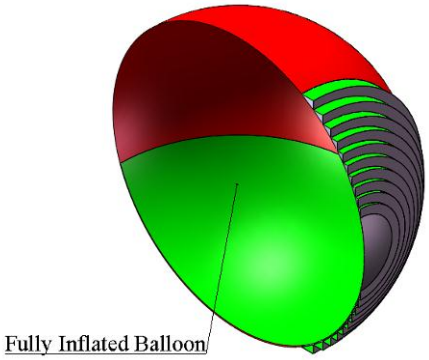

Figure 112 : Envelope Fully Inflated – AEPG at Pressure Height

The size of the membrane mainly depends on the value set for the operational altitude since it determines the maximum expansion of the lifting gas. The parameter used for this kind analysis is called inflation fraction and it indicates the ratio between the gas bag initial volume and the maximum volume of the envelope. Under the assumptions considered in this study (pressure height of 6000 m and standard atmosphere conditions) the inflation fraction can be estimated around 55%, which means that the gas volume at operational altitude becomes about twice the initial value on the ground. Therefore the volume contained within the ballonet must be about half the value of the total envelope volume. Figure 111 shows that the ballonet membrane is a fabric spherical cap attached to the internal surface of the envelope. The ballonet volume is the sum of the volumes contained in the two equal spherical caps which can be related to the radius of the sphere and the height of the cap (Figure 113) as:

$$V_{Cap} = \frac{1}{3} \cdot \pi \cdot h^2 \cdot (3R - h) \tag{8.20}$$

By imposing

$$V_{Cap} = \frac{1}{4} V_B \tag{8.21}$$

The value of the cap height can be determined which is:

$$h \cong 21.25m \tag{8.22}$$

From this value the surface of the ballonet membrane can be evaluated as:

$$S_{Cap} = 2 \cdot \pi \cdot R \cdot h \tag{8.23}$$

Materials employed in ballonets require limited strength as there is no difference in pressure between the contained gas and air. However they must have good flexibility and permeability characteristics since they are subjected to frequent movement and possible sloshing [109]. Both coated and laminate materials can be used, usually constituted by lightweight nylon or polyester fabrics and polyhuretane coatings. The

density can be around 0.18 kg/m^2 [110] which gives a total membrane mass of 781 kg. Considering the presence of blowers, ducts and valves it seems reasonable at this stage to allocate about 1500 kg for the whole subsystem.

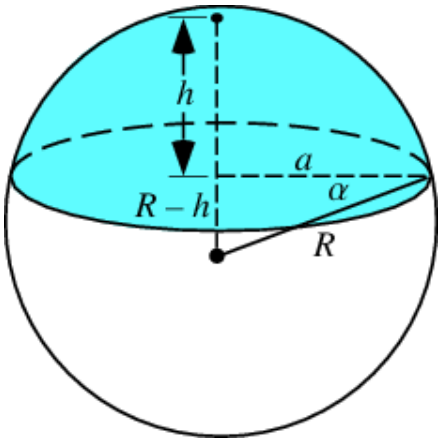

Figure 113 : Ballonet Volume and Surface Calculation

8.4 Pointing Mechanism

This section addresses the design of the mechanism employed to track the sun movement during the day. A description of a possible solution to be implemented is provided together with a preliminary sizing of this subsystem which is based on the inertial characteristics of the AEPG and on the pointing performance required.

The power output of a solar cell depends on the angle between the incident light and the surface of the device. Therefore this angle needs to be minimised, making sure that the solar cells are all facing the sun during the day. The annular rigid plates have been introduced in section 8.2 in order to guarantee that all the PV cells face the same direction. However as the Sun position in the sky changes during the day, it is necessary to include in the design a mechanism responsible for the tracking of this changing position.

In ground based applications, the introduction of a sun tracking device is usually justified only in the case of large PV plants as the added cost introduced can be significant. Most of these plants employ high efficiency solar cells or concentrator systems (like Fresnel lenses) which require pointing accuracies of about ±2° for low concentration systems up to values of ±0.1° in the case of high concentration systems. Other applications of these devices include heliostats which consist of a series of mirrors that reflect the solar radiation towards a fixed point, usually a gas tank that needs to be heated. The mirrors must therefore maintain a fixed angle between the direction of the sun and the direction towards which the light has to be reflected.

Tracking systems can perform single or dual axis rotations (Figure 114) and it is estimated that the increase of the total solar production due to their introduction in the design of the PV plant can be as high as 35% of the values obtained with fixed solar panels (at optimum inclination angle and facing South).

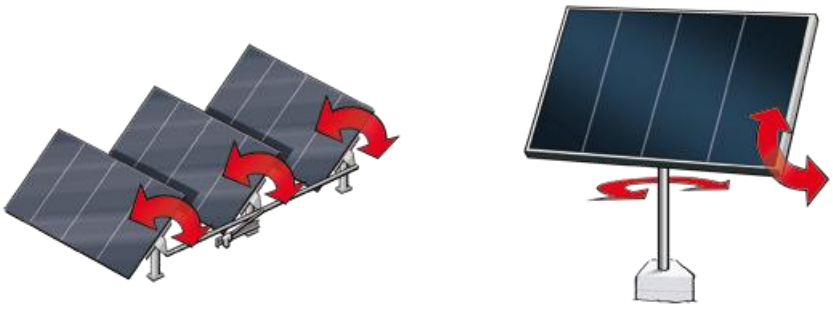

Figure 114 : Single and Dual Axis Tracking System for Ground Based PV Arrays (http://www.solar-tracking.com/)

In the case of the AEPG the pointing mechanism needs to be capable of tracking the sun position by providing enough torque to overcome the inertia of the entire system and possible external disturbances. The pointing mechanism concept is shown in Figure 115. The sun tracking movement is performed through the implementation of a gimballed system that provides rotations around two different axes. The balloon is constrained by two rotational joints on two opposite points along the equatorial line that allow control for the first rotation by actuation of two electric motors.

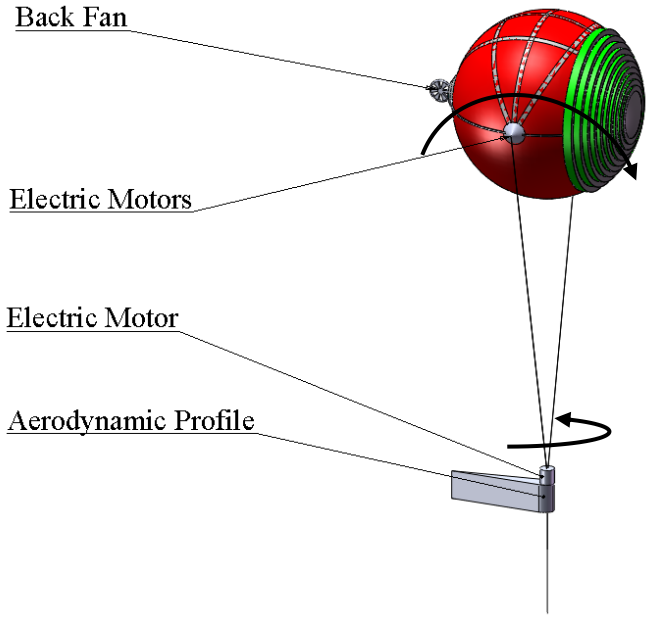

Figure 115 : Pointing Mechanism Concept

On the other hand control about the second axis can be performed locating another electric motor at the confluence point of the harness tethers. This motor would generate a relative rotation between the balloon and the mooring tether. A symmetric aerodynamic profile is introduced which will line itself up with the wind direction (like a weathervane) and stabilize the lower part of the cable. A possible drawback of this relatively simple concept is that it can't guarantee the stability of the tether in case the wind speed is too low for the effect of the aerodynamic profile to be significant. A possible solution would employ a propeller located behind the aerostat which can provide the necessary rotation.

The pointing mechanism can be operated in feedback mode. Therefore the subsystem needs to detect the relative orientation between the AEPG and the sun in order to generate an error signal which is used to create the command for the electric motors. This operation can be performed using the signal coming from some sensors (such as photodiodes) located on different areas of the external surface. The comparison of these signals can be directly employed to adjust the orientation of the AEPG.

As an alternative method, the information about the position of the sun in the local reference frame can be stored on board the vehicle. This information determines the target attitude of the AEPG, depending on the geographical location, day of the year and time of the day. On the other hand the orientation of the AEPG in the local reference frame can be determined by using other types of devices. For example, as the size of the balloon is significant, a set of GPS antennas could be located in different points of the envelope and the orientation could be calculated from the relative positions detected. Other devices would include magnetometers to measure the local magnetic field or accelerometers to detect the local vertical.

The assessment of which method is the most suitable is beyond the scope of this preliminary analysis and the final aim of this research. More important in this phase is to evaluate the possible masses contributions of the components included in the pointing mechanism design as presented in the following section.

8.4.1 Components Preliminary Sizing

The preliminary sizing of the components concerns the selection of a set of electric motors with characteristics suitable for the performance required. The assessment is based on different considerations about the inertia characteristics derived from the

geometric and mass properties obtained so far and on an evaluation of the angular velocities and accelerations necessary for tracking.

Requirements

Considering the ideal case of absence of external moments applied, the torque required to rotate a rigid body about an axis is obtained by multiplying the angular acceleration by the moment of inertia with respect to that particular axis. In the case of the AEPG, the spherical shape of the external envelope is expected to significantly reduce the effect of external aerodynamic disturbances. Moreover the effect of the atmospheric air viscosity is considered negligible for the present analysis.

Another important issue to be taken into account is the position of the centre of mass with respect to the centre of buoyancy which can generate a torque proportional to the distance between the two points and to the total mass of the system. As the total of mass is large, even small distances between the centre of mass and centre of buoyancy could lead to significant values of external torque.

The contributions to the moment of inertia of the system derive from the structural components assessed so far, the PV array located on the frontal area of the balloon, the subsystems components located in the back case and the ballonet membrane. As a first approximation the AEPG can be assumed as a perfect sphere of radius 32.5 m and the total mass of the system can be assumed to be distributed over the external surface. Under this assumption the moment of inertia with respect to any axis of the sphere can be determined as:

$$I = \frac{2}{3} M \cdot R^2 \tag{8.24}$$

The mass evaluated so far can be set to a value of about 34.2 T which leads to a moment of inertia of about 2.4e7 kg*m^2. A more precise estimate of this parameter can be determined using the CAD developed during the study. The values obtained for azimuth and elevation rotations are 3.0e7 kg*m^2 and 3.1 e7 kg*m^2 respectively.

At the high latitudes considered in this study, i.e. where the AEPG is expected to be employed, the values of Sun Azimuth and Elevation velocities and accelerations are very low as presented in Figure 116 and Figure 117 for the Summer solstice. However if these values were considered to calculate the torque and power required by the electric motors, the final results would lead to an undersized component.

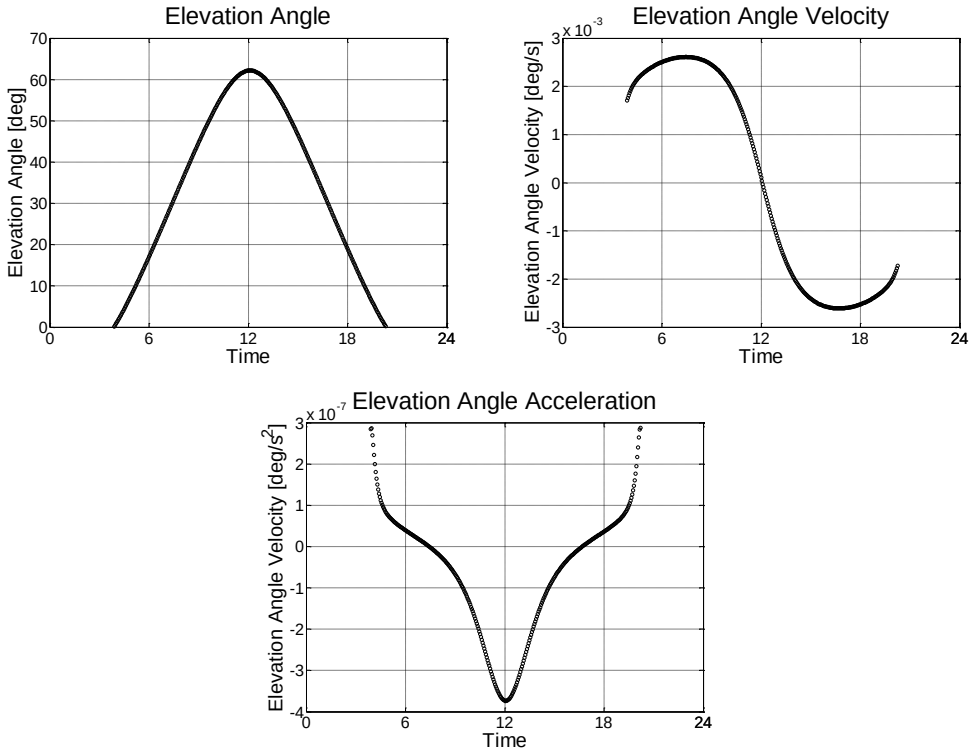

Figure 116 : Elevation Angle, Velocity and Acceleration for South of the UK at Summer Solstice

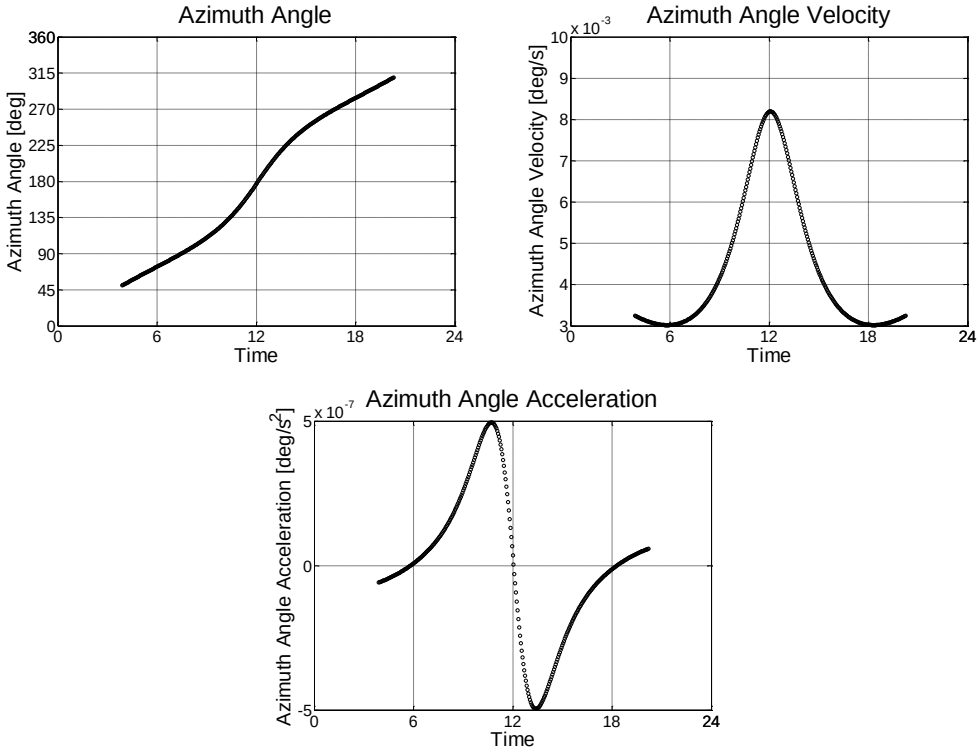

Figure 117 : Azimuth Angle, Velocity and Acceleration for South of the UK at Summer Solstice

This is due to the fact that one of the motors is located along the mooring tether which can be tilted with respect to the horizontal plane due to the aerodynamic drag acting on the balloon. In particular the analysis presented in section 6 has determined a value of about 71 deg for the steady state conditions. Considering this scenario, the velocity and

acceleration required by this motor can increase significantly as the Sun elevation at culmination can be very close to the inclination of the tether. This condition (target passing above the tracking station) is usually the design driver for different tracking systems that employ two independent rotations to perform the pointing as presented in [140]. Figure 118 shows the angles, angular velocity and accelerations required by the motor in order to perform the tracking, when the Sun Elevation at culmination is close to the tether inclination. It can be noticed how the velocity and acceleration values increase as the limit condition is approached (curves from 5° to 1° in the figure), which is constituted by the Sun passing perfectly above the balloon at culmination. This is indeed a limit condition as the tracking in this case can be performed rotating the motors located along the equator by 180°. Table 44 summarises the maximum values of the velocities and accelerations obtained, while Table 45 presents the resulting figures for the torque and power required by the motor.

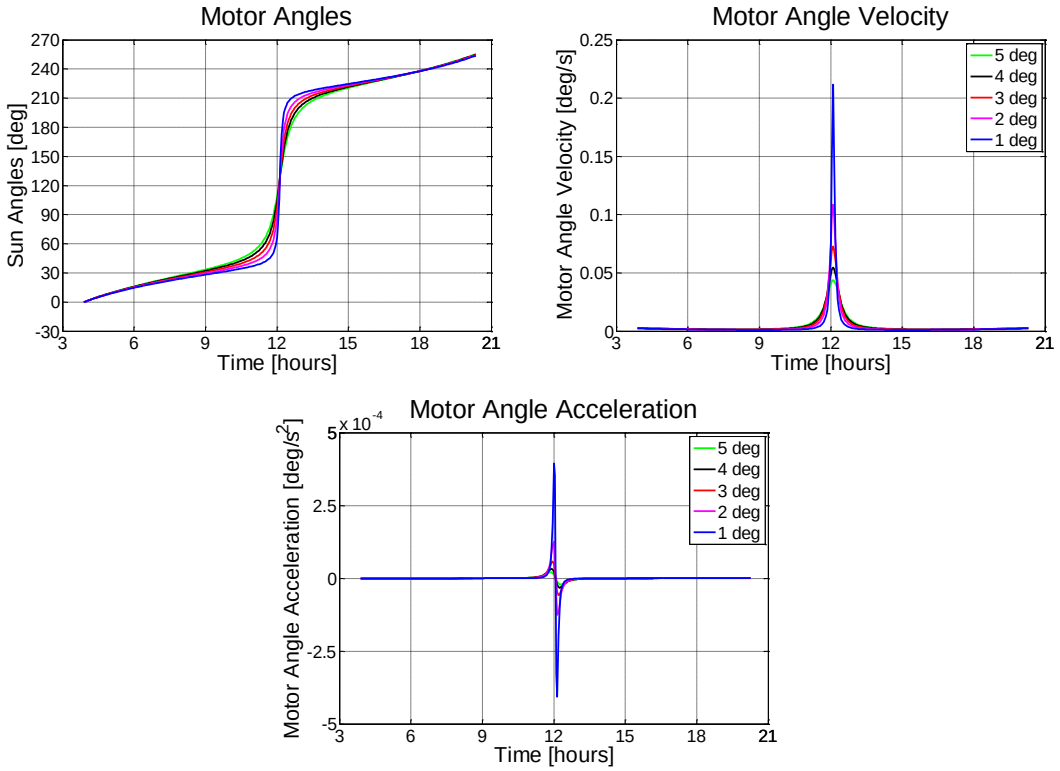

Figure 118 : Electric Motor Angle, Velocity and Acceleration

Angle from Tether Inclination	Max Ang. Velocity [°/s]	Max Ang. Acceleration [°/s^2]
1°	2.1E-01	3.9E-04
2°	1.1E-01	1.3E-04
3°	7.3E-02	5.8E-05
4°	5.5E-02	3.3E-05
5°	4.4E-02	2.0E-05

Table 44 : Angular Velocity and Acceleration for Different Values of the Zenith Angle

Angle from Tether Inclination	Motor Torque [Nm]	Motor Power [W]
1°	1.7E+02	6.1E-01
2°	5.3E+01	1.0E-01
3°	2.4E+01	3.1E-02
4°	1.4E+01	1.3E-02
5°	8.4E+00	6.5E-03

Table 45 : Motor Torque and Power Required for Sun Tracking

The value of power required is very low as the velocities levels are not significant while torque can reach a value of 170 Nm in the worst case. The figures obtained under these assumptions are not expected to constitute a show stopper.

However it is important to evaluate the electric motors requirements related to a possible unbalance of the system. In order to be able to assess the torque required, it is very important to evaluate the distance between the centre of mass and the centre of buoyancy. The centre of buoyancy is fixed and it corresponds to the geometric centre of the displaced fluid. On the other hand, the position of the centre of mass can be different from the geometric centre of the system as it depends on the distribution of the different mass components.

During the ascent, the centre of mass will be located in the lower part of the envelope (below the centre of buoyancy) as the ballonet will be partially inflated with air (Figure 119). The location of the centre of mass below the centre of buoyancy stabilises the balloon during the ascent as possible instabilities are damped by the moment created by the weight force with respect to the centre of buoyancy.

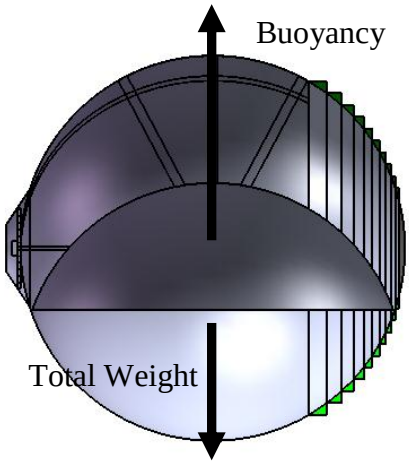

Figure 119 : Relative Positions of Centre of Mass and Buoyancy during Ascent

During the operational phase, i.e. when the sun tracking movement has to be performed, it is important to reduce the effect of the moment created by the weight force with respect to the centre of buoyancy. During operational conditions at pressure height, with the ballonet is completely empty, the centre of mass and centre of buoyancy should be

ideally coincident in order to effectively reduce the torque required by the electrical motors located along the equator. This needs to be done balancing the effect of the different mass contributions, in particular compensating the effect of the frontal PV array weight with the other subsystems located in the back case (schematically presented in Figure 120).

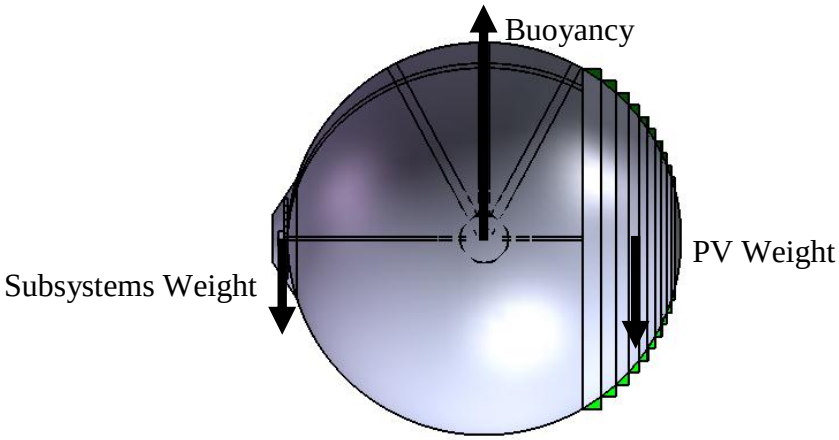

Figure 120 : Minimization of the Relative Positions of Centre of Mass and Buoyancy

Assuming a maximum tolerance in the distance between the centre of mass and centre of buoyancy of 1 m and a mass of 34.2 T, the resulting moments would be 3.4e5 Nm which is evidently the design driver if compared to the figures previously evaluated. Moreover considering the same values of angular velocities presented in Table 44, the power required by the motor would vary between 0.3 kW and 1.2 kW.

These performances can be obtained coupling the electric motor with some form of torque multiplication (Figure 121), constituted by a gearbox which can allow very high reduction ratios. The main drawbacks of this configuration concern the added mass and complexity, the possible wear of the components and the decreased efficiency of the overall mechanism.

As the power levels are still quite low due to the small angular velocity, the mass of the electric motor is not significant. For example the results obtained for AC servo motors, usually employed in applications which require quick and precise response, are shown in Figure 122. On the other hand the speed reduction mechanisms are expected to provide the main contribution to the overall weight. This figure depends on the reduction ratio, input/output velocities and torque [141]. As a first conservative estimate at this preliminary stage of the study a total mass of 500 kg for each unit (motor+gearbox) is allocated.

Figure 121 : AC Servomotor and Gear Box [141]

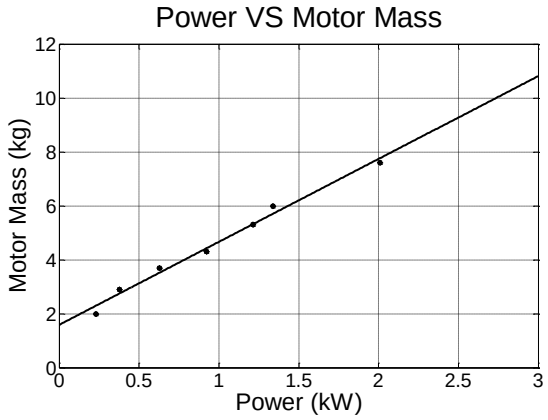

Figure 122 : SDD Servomotors Power VS Mass [142]

In this phase of the research it is not possible to provide an accurate estimate of the mass of the aerodynamic profile responsible for the stability of the lower part of the mooring tether. The analysis of this component would require a detailed aerodynamic analysis in order to define chord length, camber characteristics and total span which is beyond the scope of this study. The mass contribution can be significant (see Table 46 for typical values of the wing system mass for some small commercial aircrafts). However it must be pointed out that it won't affect the value of the balloon inertia and the choice of the electric motors.

Aircraft	Wing System Mass [kg]	Wing Span [m]
Citation-500	463	13.3
F-28	3414	23.6
DC-9	4248	28.5
727-100	8020	40.6

Table 46 : Mass Values for Small Commercial Aircrafts [143]

Similar conclusions can be inferred about the possibility of employing a propeller (or more than one) to be located on the back case, which would be operated in low wind conditions. The actual need for this component must be assessed on the basis of the aerodynamic profile performance and its sizing will be a trade-off between the

improvement in terms of pointing capabilities and the drawbacks coming from the increased mass and power consumption as the propeller will be driven by an electric motor. The mass is therefore expected to be of the same order of magnitude of the electric motors assessed above.
Finally the design of a pointing mechanism involves different technical problems related to the choice of the control law to implement and the overall stability and accuracy of the subsystem. These control aspects of the design are not assessed for the moment. Nevertheless it is important to stress the fact that these issues are very important for the feasibility of the concept and need to be evaluated in detail during the next phases of the project.

8.5 Final Concept Layout

This section summarises the results obtained for the subsystems analysed so far and adds some considerations about the components that remain to be assessed. The final aim is to present the layout of the AEPG concept, a preliminary weight breakdown and highlight the important issue of the balance of the system which has a direct influence on the performance of the generator.
The final external layout is presented in Figure 123 while Table 47 shows the weight breakdown of the AEPG expressed as absolute values [kN] and as a percentage of the buoyancy value. The components evaluated so far constitute the 82% of the total buoyancy available. Fixing the value of the free lift to the 30% of the buoyancy, the unallocated weight is 168.5 kN (17.2 T mass) which represents around the 18% of the buoyancy value. This value is quite significant although it must be noticed that this amount of available buoyancy must be distributed among all the subsystems that haven’t yet been assessed. In particular it is necessary to take into account for the presence of additional components such as energy storage devices to be employed in low sun conditions to power the subsystems and electronic components necessary for the optimization of the power production. The available buoyancy allocation also needs to consider possible inaccuracies of the previous weight estimates, verifying the assumptions made and checking if the revised values can constitute a show stopper for the technical feasibility of the system.

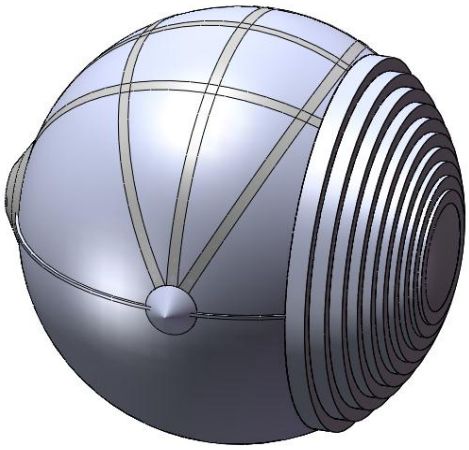

Figure 123 : AEPG External Layout

	Weight [kN]	% of the Buoyancy
Buoyancy	950.0	-
Lifting Gas (Helium)	131.2	13.8
Spherical Envelope	64.9	6.8
Cylindrical Membranes	27.3	2.9
Internal Membrane	20.2	2.1
PV Array	95.8	10.1
Vertical Ring	5.4	0.6
Equatorial Ring	3.4	0.4
Support Strips	6.2	0.7
Back Case	29.4	3.1
Pointing Mechanism Motors	14.7	1.5
Gas Pressure Control System	14.7	1.5
Inverter	29.4	3.1
Transformer	19.6	2.1
Tether Conductor	10.7	1.1
Tether Composite	23.5	2.5
Free Lift	285.0	30.0
Buoyancy Available	168.5	17.7

Table 47 : AEPG Weight Breakdown

As described in the previous section the importance of the overall balance is crucial as small distances between the centre of mass and the centre of buoyancy generated high torque for the pointing mechanism. Therefore these two points should be ideally coincident. A possible drawback can be that the system becomes unstable and the effect of external disturbances is not damped. However as the external shape is spherical, the effect of disturbances is expected to be small and the presence of a stabilising moment is not necessary. The requirement of minimising the torque required by the motors

remains the priority due to the high value of the weight involved in the design. At this stage of the study it is important to stress the importance of this technical issue which needs to be constantly assessed during each phase of the design. However at the present stage this doesn't seem to constitute a show stopper for the technical feasibility also considering that part of the available buoyancy margin can actually be allocated as ballast to guarantee the overall balance of the system.

9 CONCLUSIONS

The work presented in this thesis has been focused on the assessment of the technical feasibility of the Aerostat for Electric Power Generation concept. The research is very multidisciplinary and different areas have been investigated following a system engineering approach. The next sections summarise the main conclusions obtained for each of the technical areas considered throughout the project.

Due to the preliminary character of the study, the analysis is based on different conservative assumptions which need to be revised in the next phases in order to optimize the design of the AEPG. Furthermore, although the present preliminary analysis hasn't found a specific show stopper for the technical feasibility of the AEPG, some important areas have been identified on which the next activities of the research should be focused.

9.1 High Altitude Solar Irradiation

In section 2 a new simple method has been derived to assess the solar radiation available as a function of the altitude. Previous analogous models are usually targeted at scientific applications and they imply a certain degree of complexity that goes beyond the requirements of a preliminary study. On the other hand user friendly applications have been developed just for ground based PV generators for the evaluation of the potential energy production of a specific location.

Therefore the development of the model described in section 2 represents the first contribution of this study as it allows a relatively easy preliminary assessment of the potential of a solar generator located at different altitudes above the ground.

The evaluation has shown that for a typical location in the south of the UK, the gain in solar radiation collected at different altitudes ranges between 3.3 and 4.9 for a platform located between an altitude of 6km and 12km, compared to a ground based PV system. Moreover a platform at 12 km could collect around 45% the energy falling on a solar generator orbiting the Earth in geostationary orbit (Solar Power Satellite option). For the present study an operating altitude of 6 km has been selected on the base of considerations about solar radiation, wind speed values and non technical constraints.

The model is based on simplifying assumptions; however it must be pointed out that these assumptions are generally conservative and would lead to an underestimate of the advantage deriving from the installation of the AEPG.

First of all the location assumed for the calculation is relatively well placed in terms of weather conditions. Secondly the contribution of the reflected radiation to the total irradiation budget has not been included in the estimate. This component is expected to be significant as the generator will be located above a cloud layer with high reflection coefficient. Taking into account these conservative assumptions, the estimated advantage is expected to increase when considering locations at higher latitudes and including the reflected components in the calculations.

9.2 Steady State Analysis

In section 6 the possible variations of the different design parameters were investigated. In particular the analysis has assessed the possibility of employing different photovoltaic technologies, i.e. thin films, crystalline silicon and multijunctions. Depending on the technology chosen for the PV array, the values of peak power that can be expected range from 0.1 MWp and 1.5 MWp, with a balloon diameter ranging from 41 m to 92 m. These sizes are compatible with the dimensions of other lighter than air vehicles developed in the past and currently in operation. On the other hand the values of peak power are analogous to PV power plants installed in remote areas which are not connected to the national grid.

Moreover a steady state model has been developed for the evaluation of the equilibrium configuration of the system when subjected to a mean wind speed profile. The model is based on a discretization of the tethered aerostat which allows the determination of the aerodynamic loads on the structure and the final displacement values. Although analogous models have already been developed for the study of tethered balloons, the one presented in section 6 includes the specific design parameters used to characterise the AEPG, providing a significant contribution towards the assessment of the viability of the system.

The results obtained for different combinations of design parameters show that (setting a tether length of 6000 m) the horizontal displacement of the tethered balloon when subjected to a mean wind speed can reach values of up to 2,600 m while the minimum value for the final altitude is 5,500 m. The horizontal displacement can represent an important issue as a large free area around the mooring point has to be provided. However it must be pointed out that the minimum values for the tether inclination angles range from 62° to 76°. The tether position is therefore expected not to affect the possible exploitation of the ground area around the mooring station, such as for

cultivation purposes. Concerning the operating height, the minimum value evaluated for the final altitude is not expected to significantly reduce the solar radiation collected.
The steady state sensitivity analysis performed on the baseline configuration demonstrates the preliminary viability of the concept under the conditions assumed for the analysis. In particular the inaccuracies assumed for the mass of the different components don't seem to be particularly critical for the further development.
Nevertheless the uncertainty on the drag coefficient value and mean wind speed, could lead to increased levels of aerodynamic loads which, even non representing a critical show stopper, would significantly affect the final position of the tethered balloon.

9.3 Dynamic Analysis

The dynamic analysis performed in section 7 has evaluated the system displacements and the tether forces due to possible unsteady atmospheric conditions. This is an extension of an existing finite model developed to estimate the 2D response of a tethered balloon when subjected to a single gust. The finite element model has been improved in order to provide a full 3D simulation of the AEPG when subjected to realistic operational conditions (gusts and continuous turbulence). The validation of the model has demonstrated the viability of this method for the present investigation. Therefore the model further contributes to the study of the dynamic behaviour of tethered balloons providing a validated tool which can be employed for the analysis of similar LTA systems.
The results demonstrate that the characteristics of the system are such that the high frequency turbulence components are effectively filtered, i.e. the dynamic loads are only marginally larger than the static ones. Under the assumptions considered during the analysis, the dynamic behaviour of the AEPG doesn't seem to constitute a show stopper for the feasibility of the system. Moreover the effect of an increase in the drag coefficient is less significant than in the case of the steady state configuration.

9.4 Concept Design

The concept design has addressed the layout of the innovative photovoltaic generator and the preliminary sizing of its main components. In particular the structural components have been considered and their mass contributions have been evaluated on the base of the expected load conditions. The results obtained demonstrate the viability of the structural solution adopted, consisting of a single pressurised envelope

constituted by a spherical part and a series of cylindrical membranes used to support the PV array. Moreover the layout selected for the PV array is expected to have a negligible effect on the solar cells power output, while the components responsible for the loads distribution are expected to be able to provide a convenient equilibrium configuration during operations.
The analysis has also highlighted the importance of evaluating the accurate position of the centre of mass of the system with respect to the centre of buoyancy.
Finally the breakdown presented in section 8.5 has summarised the mass contributions allocated to each of the subsystems considered in the preliminary analysis, evaluating the margin left to include possible inaccuracies, the contributions coming from unallocated components and the possibility of introducing some ballast to guarantee the overall balance.

9.5 Further Work

High Altitude Solar Irradiation

Due to the preliminary character of the study, the model introduced for the evaluation of the solar radiation is based on simplifying conservative assumptions and further activities would be necessary to provide a more accurate estimate of the potential of the AEPG. First of all a more accurate analysis of the extinction parameter would require the attenuation to depend on the radiation wavelength considered, as the atmospheric components can have different effects on different wavelengths.
Secondly some considerations have been included which point out the importance of the reflected radiation contribution especially taking into account for the presence of a cloud layer located under the collector and the Earth surface albedo. The analysis needs to be completed evaluating this contribution, which is expected to significantly increase the total energy budget.
Finally the method is applied to a particular location in the South of the UK and general conclusions are inferred for other locations at analogous latitudes and with analogous climates. However the present values estimated for the potential of the AEPG are expected to be quite conservative due to the relatively good location in a UK context (in terms of solar radiation reaching the ground) considered in the calculations. A more accurate analysis would require the model to employ experimental datasets relative to the specific location potentially considered for the installation of the AEPG. The

employment of specific experimental data would allow a more accurate estimate of the potential of the solar generator and a more precise evaluation of the optimum value for the operating altitude.

Steady State Analysis

The steady state model is based on a parametric description of the main subsystems involved in the design of the AEPG. Therefore the model can be updated during the following phases of the system design as more refined characterisations of the different subsystems are available.

Moreover since the sensitivity analysis has highlighted the importance of a more accurate evaluation of the drag coefficient, an aerodynamic analysis of the entire system is required in the very next phase of the research including CFD simulations and wind tunnel tests.

Dynamic Analysis

Analogous considerations can be inferred in the case of the dynamic simulation about the opportunity of performing a more detailed aerodynamic analysis in order to provide an accurate estimate of the drag coefficient.

More important in the case of the dynamic model is the introduction of the aerodynamic torques which would potentially affect the performance of the mechanism employed to track the sun movement. The updated version of the FEM model needs to include these contributions and the resulting rotations in order to assess if they can be critical for the performance of the AEPG.

Concept Design

The concept design has provided a first assessment of the different subsystems involved in the development of the AEPG and a preliminary sizing of the various components. Some potentially important technical areas remain to be investigated in order to complete the design of the AEPG. Moreover for each phase of the study, it is necessary to revise the design of the components already evaluated in the present analysis and update the mass breakdown determined. Where possible, this recursive design process should employ off the shelf components in order to reduce the potential cost of the generator.

In particular it is necessary to evaluate the possibility of introducing an energy storage system to be employed in low irradiation conditions. Moreover the different electronic components responsible for the condition and distribution of the produced power must be evaluated as well as the internal structure of the mooring tether.
Concerning the sun tracking subsystem, the components considered so far include the electric motors to provide the rotations along two different axes. Other components such as the aerodynamic profile and the fans remain to be evaluated. Their contribution in terms of mass and performance needs to be included in the following phases of the design as they might be critical for the overall viability. Furthermore the control stability of the mechanism must be addressed, defining the control law suitable for the dynamic characteristics of the system and the performance of the pointing.
Once these components are introduced in the design and the technical feasibility is confirmed, it is important to assume an operational scenario and include in the assessment the possible performance of the generator. It will then be possible to evaluate with more accuracy the potential advantage of the AEPG when compared to traditional ground based PV systems.
The revised value of the gain will lead to the assessment of the economic viability of the PV generator. This economic analysis will need to identify the specific applications in which the AEPG would be employed including possible non-technical aspects such as safety and regulatory issues which could prevent the system from being installed in some areas. Once the technical feasibility of the PV generator is verified together with its economic viability, it will be possible to infer if the AEPG will be able to provide a suitable solution to contribute to release the potential of the photovoltaic technology regardless the weather condition of the location in which the generator is installed.

10 APPENDIX A : Photovoltaic Cell: Basic Principles [111]

The PV cell is the fundamental element of a PV system, in which the conversion of the solar radiation into electrical energy occurs. This device is able to absorb the incident solar radiation, generate and separate mobile charged particles and produce electrical current, exploiting the electronic structure of semiconductor materials.

The electronic structure of an atom can be thought as constituted by different bands, which are related to the energy level of the electrons. In particular the electrons responsible for the atomic bonds are located in the valence band, while those responsible for the conductive behaviour of the material are located in a higher energy band defined as conduction band. The two bands are separated by a bandgap, also called energy gap (E_g), which is defined as:

$$E_g = E_c - E_v \tag{10.1}$$

where E_c and E_v identify the energy level of the conduction and valence band respectively.

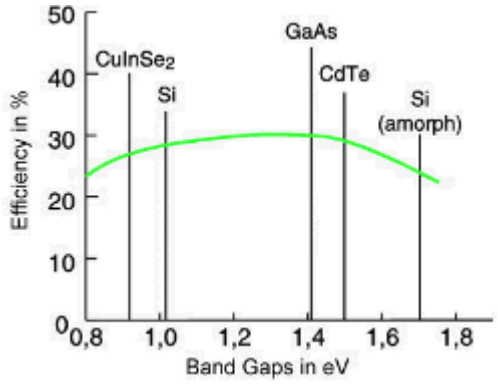

Figure 124 : Band Gaps for different materials

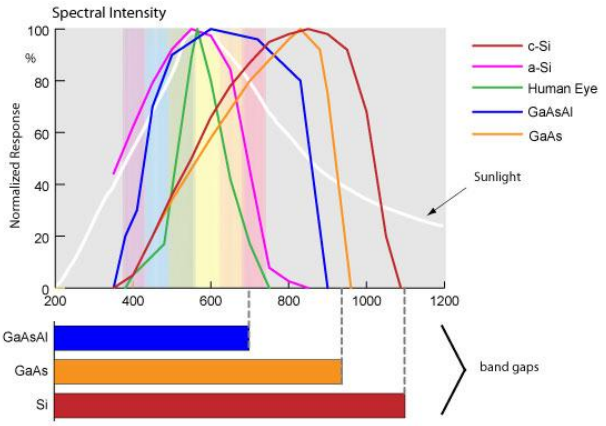

Figure 125 : Solar Spectrum Converted by different types of solar cells

The pure semiconductor has the property of having the valence band completely full and no electrons in the conduction band. In normal conditions this material acts as an insulator. However it is possible to add some impurities in the semiconductor structure in order to artificially modify the arrangement of the electrons. This process is defined as doping and is used to obtain extra electrons (n-type) or holes (p-type) in the element lattice.

The PV cell is based on the creation of a p-n junction which generates a diffusion of electrons and holes through the materials creating an electric field in the interface region. This electric field tends to pull electrons into the n side and holes in the p side. When a photon with energy in excess of the bandgap reaches the junction, an electron is promoted to the conduction band and an electron-hole pair is generated. This happens in both n-type and p-type sides of the junction. As a consequence the electrons from the p side and the holes from the n side move to the junction and are pulled to the other side by the electric field. This mechanism generates an electric current across the junction. The typical structure of a solar cell, including the detail of the different layers is shown in Figure 126 together with the schematic representation of the band diagram.

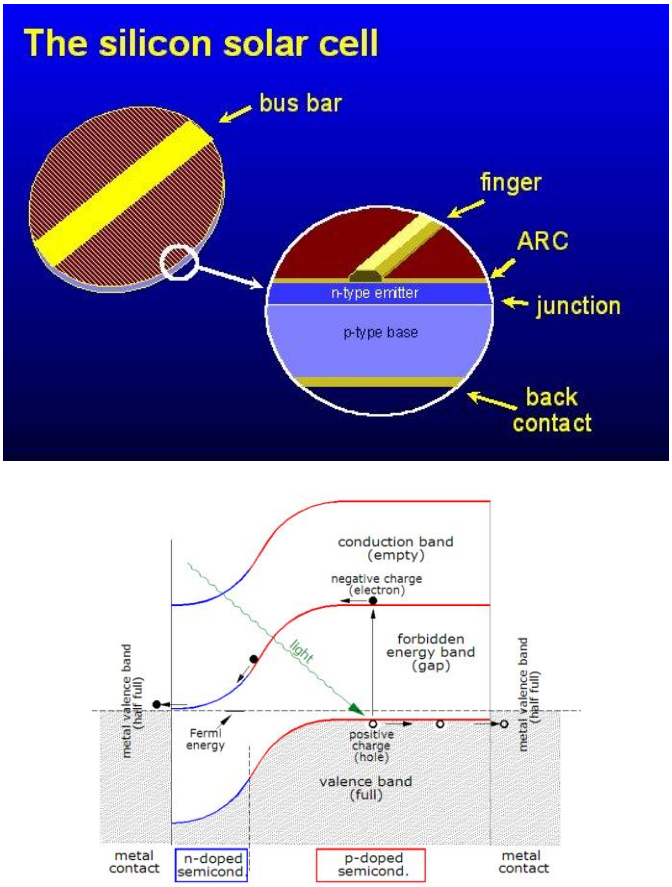

Figure 126 : Photovoltaic Internal Structure [144] and band diagram

The power generated by the cell is calculated as the product between current and voltage produced which are described by the curve in Figure 127. It can be notices that its value becomes zero in open or short circuit conditions.

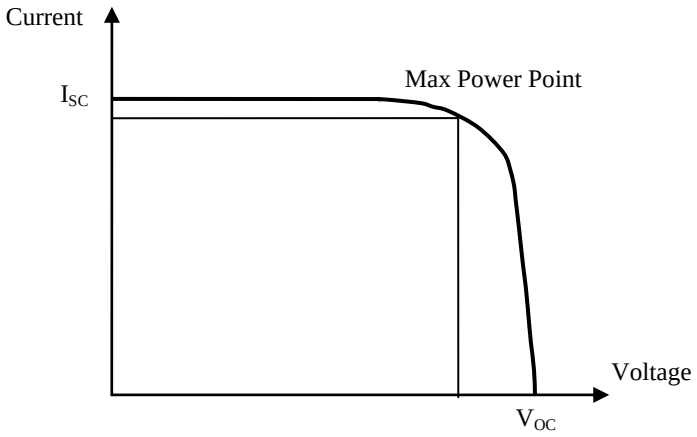

Figure 127 : I-V characteristic of a solar cell with maximum power point

The maximum power can be determined as:

$$P_{\max} = FF \cdot V_{OC} I_{SC} \tag{10.2}$$

where V_{OC} is the open circuit voltage, I_{SC} the short circuit current and FF is defined as fill factor. Another important parameter to be considered when evaluating the performance of a PV cell is the efficiency η defined as the maximum power produced by the cell divided by the power of the incident solar radiation, calculated in standard conditions, i.e.:

- Irradiance at 100 mW/cm^2
- Standard reference AM1.5 spectrum
- Temperature 25˚C

Actually the efficiency of solar cells for space applications is usually evaluated for different standard conditions, related to the ones expected in space, i.e. without the attenuation due to the presence of the atmosphere:

- Irradiance at 135.3 mW/cm^2
- Standard reference AM0 spectrum
- Temperature 28˚C

For a description of the fundamental losses involved in the determination of the cell efficiency, the reader should refer to [111]. Here, two particularly important effects are introduced which concern the influence that the cell temperature and irradiance value have on the I-V curve.

As the cell temperature increases, its effect is to reduce the value of the open circuit voltage V_{OC} to lower values. On the other hand the current and fill factor variations are almost negligible, resulting in an overall reduction of the total power produced. On the contrary an increase in the irradiance collected by the cell corresponds to an increment in the short circuit I_{SC}, while the voltage variation is much smaller. The final result is an increment in the value of the generated power. These two effects are presented in Figure 128.

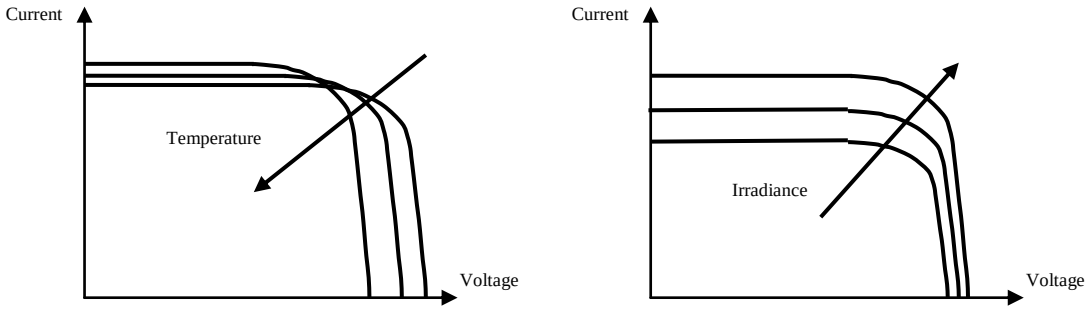

Figure 128 : Temperature and Irradiance Effects on I-V Plot

The application presented in this study involves high altitudes where the atmospheric temperature can be very low as described in section 3.2 and the wind speed can contribute to the convective thermal exchange between atmosphere and solar cell. Moreover the results presented in chapter 2 show that the irradiance can reach values higher than the 1000 W/m^2 considered as standard conditions when evaluating the efficiency of the solar cells. It is therefore expected that the atmospheric conditions in which the system is due to operate will have a beneficial effect on the final performance of the PV cells.

11 APPENDIX B : Airship Materials

A comprehensive review of the materials employed for lighter than air applications is included in [109] and the information presented in this section is mainly derived from this source. Moreover useful information about envelope materials can be found in other publications such as [145], [146] and [147], which refer to the requirements specified by the FAA [74]. The present section will focus on the properties of the materials currently in use, with the purpose of providing a picture as complete as possible of the state of the art and contribute to the concept design phase.

The main desirable material property concern the strength to weight ratio which needs to be maximized in order for the envelope to be able to withstand the mechanical loads without being too heavy. In addition to that, in order to extend the operational life of the system, the material must have a low permeability to helium and a high resistance to environmental degradation which is particularly important as the system needs to survive at high altitude (i.e. low temperature, low pressure, high UV radiation). Other important characteristics include flexibility, resistance to tears, low creep as well as reliability of the joining techniques. However these properties will not be considered in detail in the overview due to the preliminary character of the study presented in this thesis.

Originally the materials employed in the design of LTA vehicles were constituted by natural fibres (mainly cotton) coated with natural rubber to control the gas permeability. These materials had properties that would be inadequate for current applications and therefore the introduction of synthetic fibres and rubbers had a significant impact on the performance of the envelope materials. Initially the natural rubber was replaced with neoprene and the fabrics were made of polyamides (nylon) and polyester (Dacron) as shown in Figure 129.

A further improvement was obtained substituting the neoprene with polyurethane which gave better weatherability and reduced the need for frequent maintenance. As an example, in Table 48, the properties of the neoprene coated fabrics employed for the Goodyear GZ 20 and the ZPG 3W are compared to the characteristics of the polyurethane coated fabric used for the Skyship 500 and 600 series [109]. As the thickness of the material is small compared to the other dimensions, the strength is not usually specified in [Pa] as other traditional materials. In this case the stress is

multiplied by the thickness of the material obtaining the strength in units of force over length of the coupon used during the mechanical tests [kN/50 mm].

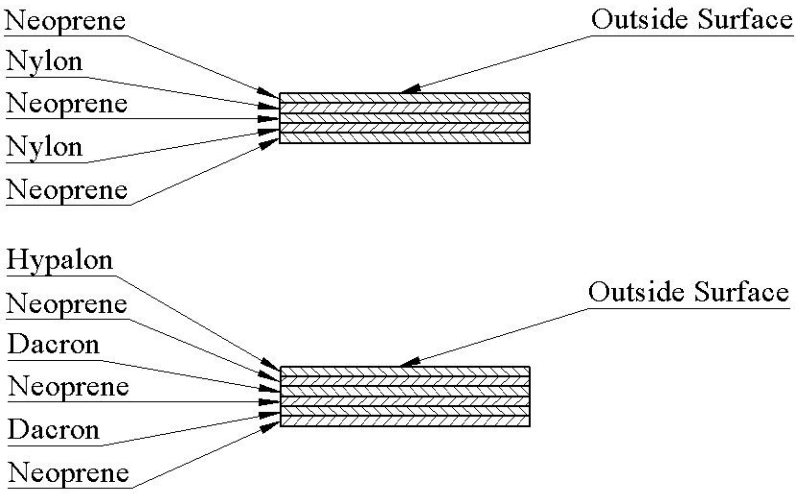

Figure 129 : Coated Fabrics Schematic Representation

Airship	Material	Density	Strength
Goodyear GZ 20	neoprene coated polyester	370 g/ m^2	1.45kN/50 mm
ZPG 3W	neoprene coated polyester	560 g/ m^2	2.8kN/50 mm
Skyship 500-600	polyurethane coated polyester	370-400 g/ m^2	1.85kN/50 mm

Table 48 : Coated Fabrics Properties

State of the art materials are usually laminate materials, which are constituted by multiple layers with different characteristics. The typical structure of a laminate is presented in Figure 130 [109] and it includes an outer protection against weather and environment, a gas retention layer and an inner load bearing component, bonded together with an adhesive.

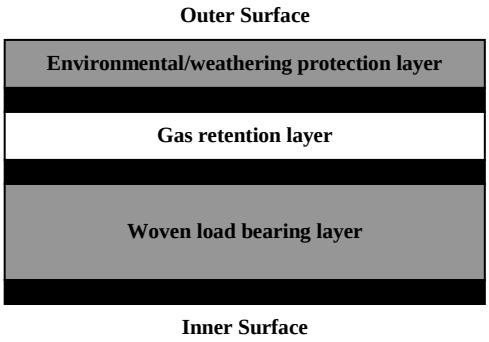

Figure 130 : Laminated Material Schematic Representation

For what concerns the load bearing component, the materials used are woven fabrics made of polyester (e.g. Terylene, Dacron), polyamide (e.g. Nylon) or aramid (e.g. Kevlar). On the other hand the gas retention layer can be constituted by a coating or a film made of different materials capable of minimising the helium losses. In the

majority of the applications, a polyester film (Mylar) is employed, as it has low permeability and good strength and stiffness. Finally the weathering component material is generally constituted by Polyvinylfluoride (PVF) commonly known as Tedlar which allows a very long operational life without maintenance to be necessary. The characteristics of the laminate material used for the US Navy YEZ 2A (Dacron woven fabric laminated with Mylar and Tedlar, using Hytrel as a bonding component) are presented in Figure 131 and Table 49, together with projected figures relative to derivatives of this fabric currently under development.

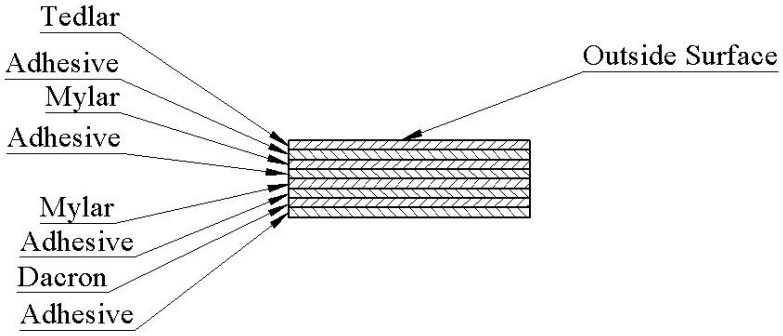

Figure 131 : YEZ 2A Laminate Material

Airship	Material	Density	Strength
YEZ 2A	Dacron, Mylar and Tedlar – Hytrel	440 g/m^2	5.25kN/50 mm
Projected	Dacron, Mylar and Tedlar - Hytrel	1 kg/m^2	14kN/50 mm

Table 49 : Laminated Material Properties

Material engineering research is ongoing and the possibility of developing LTA capable of flying at very high altitudes is highly dependent on the performance of the materials employed (i.e. mainly on the resistance and weight). The success of stratospheric platforms like the ones introduced in section 4 (by Lindstrand Technologies, Lockheed Martin and Rosaero Systems) starts from the development of performing materials. As an example the laminate material developed for Lindstrand's Hale has a mechanical resistance value of around 7.15 kN/50 mm with a density of about 295 g/m^2.

12 APPENDIX C: Steady State Model Convergence

The steady state and dynamic models presented in sections 6-7 are based on a discretisation of the tethered balloon system into a defined number of nodes and segments. The number of nodes/segments is related to the accuracy that needs to be achieved in the calculations. Figure 132 shows that with 500 segments the accuracy obtained is acceptable for the purposes of the present study. Moreover, Figure 133 shows the steady state model results, obtained for different iterations. It can be seen how the steady state model converges to the final solution after 7 iterations.

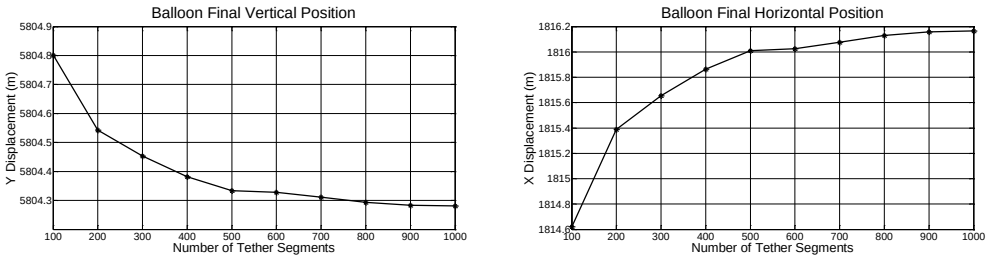

Figure 132 : Convergence of the steady state model for different numbers of tether segments

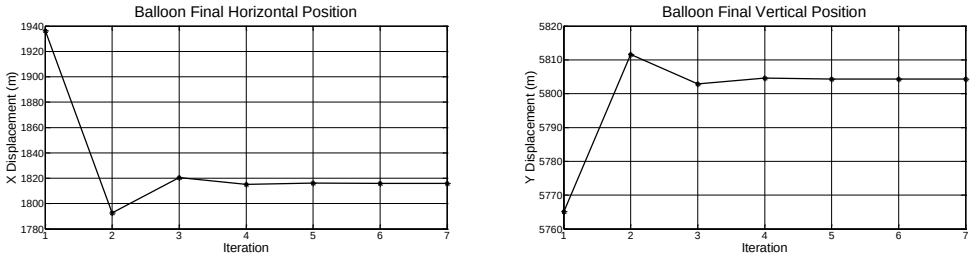

Figure 133 : Convergence of the steady state model after 7 iterations

13 PUBLISHED PAPERS

The content of this thesis has contributed to the following publications.

13.1 Journal Papers

Redi S., Aglietti G.S., Tatnall A.R., Markvart T., 2011. Dynamic Response to Turbulence of Tethered Lighter than Air Platforms. AIAA Journal of Aircraft. 48(2), 540-552.

Redi S., Aglietti G.S., Tatnall A.R., Markvart T., 2010. An Evaluation of a High Altitude Solar Radiation Platform. ASME Journal of Solar Engineering. 132(1), 1-8.

Aglietti G.S., Redi S., Tatnall A.R., Markvart T., 2009. Harnessing High Altitude Solar Power. IEEE Transactions on Energy Conversion. 24, 442-451.

Aglietti G.S., Redi S., Tatnall A.R., Markvart T., 2008. High Altitude Electrical Power Generation. WSEAS Transactions on Environment and Development. 4, 1067-1077.

13.2 Conference papers

Redi S., Aglietti G.S., Tatnall A.R., Markvart T., 2010. Preliminary design of lighter-than-air solar collectors. Proceedings of the 8th International Airship Convention, Bedford, United Kingdom, 29 Sep-3 Oct 2010.

Redi S., Aglietti G.S., Tatnall A.R., Markvart T., 2009. Configuration Study of High Altitude Solar Collectors. Proceedings of the IEEE Electrical Power and Energy Conference, Montreal, Canada, 22-23 Oct 2009.

Redi S., Aglietti G.S., Tatnall A.R., Markvart T., 2009. Collection of Solar Energy at High Altitude. Proceedings of the 24th European Photovoltaic Solar Energy Conference and Exhibition, Hamburg, Germany, 20-25 Sep 2009.

Aglietti, G.S., Redi, S., Tatnall, A.R. and Markvart, T., 2008. Exploitation of High Altitude Solar Energy. Proceedings of the 2nd WSEAS/IASME International Conference on Renewable Energy Sources (RES '08), Corfu, Greece, 26-28 Oct 2008.

13.3 Book chapters

Aglietti, G.S., Redi, S., Tatnall, A.R., Markvart, T. and S.J.I. Walker, 2010. Aerostat for Solar Power Generation. In R.D. Radescu (Ed.), Solar Energy (pp. 399-413). Published by Intech.

14 REFERENCES

[1] EU Energy and Transport in Figures (Statistical Pocketbook 2010) – European

[2] European Wind Energy Association, Wind in power – 2009 European Statistics, February 2010

[3] Oliver Morton., 2006. Solar Energy: A new day dawning? Silicon Valley sunrise. Nature 443, 19-22

[4] UNEP and New Energy Finance, 2009. Global Trends in Sustainable Energy Investment 2009, ISBN 978-92-807-3038

[5] Jaeger-Waldau Arnulf, 2010. PV Status Report 2010. Office for Official Publications of the European Union.

[6] Paula Mints, Manufacturer Shipments, Capacity and Competitive Analysis 2009/2010. Navigant Consulting Photovoltaic Service Program, Palo Alto, CA.

[7] PV News 2010, May 2010, published by The Prometheus Institute, ISSN 0739-4829

[8] PVGIS, 2007. http://re.jrc.ec.europa.eu/pvgis/

[9] Masdar, 2011. http://www.masdar.ae

[10] Africa's deserts' could provide 15% of Europe's electricity, Renewable Energy Focus, Volume 10, Issue 5, September-October 2009, Page 10

[11] Glaser P.E., Maynard O.E., Mackovciak J., Ralph E.L., 1974. Feasibility study of a satellite solar power station. NASA CR-2357.

[12] Glaser P.E., 1992. An overview of the solar power satellite option. IEEE Transactions on Microwave Theory and Techniques. 40, 1230-1238.

[13] National Research Council, 2001. Laying the foundation for space solar power: An assessment of NASA's Space Solar Power Investment Strategy.

[14] W. Seboldt, M. Klimke, M. Leipold, N. Hanowski, European Sail Tower SPS concept, Acta Astronautica, Volume 48, Issues 5-12, March-June 2001, Pages 785-792

[15] Wolfgang Seboldt, Space- and Earth-based solar power for the growing energy needs of future generations, Acta Astronautica, Volume 55, Issues 3-9, New Opportunities for Space. Selected Proceedings of the 54th International Astronautical Federation Congress, August-November 2004, Pages 389-399

[16] Mitsushige Oda, Hiroshi Ueno, Masahiro Mori. Study of the Solar Power Satellite in NASDA

[17] PowerSat 2011, http://www.powersat.com/

[18] Solaren 2011, http://www.solarenspace.com/

[19] Space Energy 2011, http://spaceenergy.com/

[20] Aglietti, G.S., Markvart, T., Tatnall, S.J. and Walker, S.J. (2008) Solar power generation using high altitude platforms feasibility and viability. Progress in Photovoltaics, 16, (4), 349-359

[21] Aglietti, G.S., Markvart, T., Tatnall, A.R. and Walker, S.J. (2008) Aerostat for electrical power generation: concept feasibility. Proceedings of the Institute of Mechanical Engineers, Part G: Journal of Aerospace Engineering, 222, (1), 29-39.

[22] Redi S., Aglietti G.S., Tatnall A.R., Markvart T., 2010. An Evaluation of a High Altitude Solar Radiation Platform. ASME Journal of Solar Engineering. 132(1), 1-8.

[23] Aglietti G.S., Redi S., Tatnall A.R., Markvart T., 2009. Harnessing High Altitude Solar Power. IEEE Transactions on Energy Conversion. 24, 442-451.

[24] Aglietti G.S., Redi S., Tatnall A.R., Markvart T., 2008. High Altitude Electrical Power Generation. WSEAS Transactions on Environment and Development. 4, 1067-1077.

[25] Aglietti, G.S., Redi, S., Tatnall, A.R. and Markvart, T. (2008) Exploitation of high altitude solar energy. Proceedings of the 2nd WSEAS/IASME International Conference on Renewable Energy Sources (RES '08), Corfu, Greece, 26-28 Oct 2008.

[26] Redi S., Aglietti G.S., Tatnall A.R., Markvart T., 2009. Collection of Solar Energy at High Altitude. Proceedings of the 24th European Photovoltaic Solar Energy Conference and Exhibition, Hamburg, Germany, 20-25 Sep 2009.

[27] Redi S., Aglietti G.S., Tatnall A.R., Markvart T., 2009. Configuration Study of High Altitude Solar Collectors. Proceedings of the IEEE Electrical Power and Energy Conference, Montreal, Canada, 22-23 Oct 2009.

[28] Redi S., Aglietti G.S., Tatnall A.R., Markvart T., 2010. Preliminary design of lighter-than-air solar collectors. Proceedings of the 8th International Airship Convention, Bedford, United Kingdom, 29 Sep-3 Oct 2010.

[29] Redi S., Aglietti G.S., Tatnall A.R., Markvart T., 2011. Dynamic Response to Turbulence of Tethered Lighter than Air Platforms. AIAA Journal of Aircraft. 48(2), 540-552.

[30] Khoury G.A. and Mowforth E., 1978. A solar airship – more than a flight of fancy. NewScientist.

[31] Khoury G.A., 1986. The case for a solar powered airship. Proceedings of Airship design and operation – present and future. Royal Aeronautical Society.

[32] Knaupp W., Schafer I., 1993. Solar powered airship-challenge and chance. Photovoltaic Specialists Conference. Conference Record of the Twenty Third IEEE.

[33] Knaupp W., Mundschau E., 2004. Solar electric energy supply at high altitude. Aerospace Science and Technology. 8, 245-254.

[34] Knaupp W., Mundschau E., 2003. Photovoltaic-hydrogen energy systems for stratospheric platforms. Photovoltaic Energy Conversion. 3, 2143-2147.

[35] ASTM, 2000, ‘‘Standard Solar Constant and Air Mass Zero Solar Spectral Irradiance Tables Standard E-490-00,’’ American Society for Testing and Materials West Conshohocken, PA.

[36] Data available at: nssdc.gsfc.nasa.gov/planetary/factsheet/sunfact.html

[37] Bonacina C., Cavallini A., Mattarolo L., 1989. Trasmissione del calore. CLEUP.

[38] Global Warming Art, 2011. http://www.globalwarmingart.com/

[39] Liou K.N. , 2002. An Introduction to Atmospheric Radiation. Second Edition. International Geophysics Series.

[40] Elterman, L., 1964. Parameters for attenuation in the atmospheric windows for fifteen wavelengths. Applied Optics. 3, 745-749.

[41] Elterman, L., 1964. Environment Research Paper No. 46, AFCRL-64-740. AFCR Laboratories, Bedford, Mass.

[42] Elterman, L., 1968. Environment Research Paper No. 285, AFCRL-68-0153. AFCR Laboratories, Bedford, Mass.

[43] Bird, R.E., Hulstrom, R.L., 1981. Review, evaluation and improvement of direct Irradiance Models Trans. ASME Journal Solar Energy Engineering. 103, 182-192.

[44] Gueymard, C.A., 2008. Rest2: High-performance solar radiation model for cloudless sky irradiance, illuminance, and photosynthetically active radiation-validation with a benchmark dataset. Solar Energy. 82, 272-285.

[45] Gueymard, C.A., 1995. SMARTS, A Simple Model of the Atmospheric Radiative Transfer of Sunshine: Algorithms and Performance Assessment. Technical Report No. FSEC-PF-270-95. Cocoa, FL: Florida Solar Energy Center.

[46] Kasten, F., Czeplack, G., 1980 . Solar and Terrestrial Radiation Dependent on the amount and type of cloud. Solar Energy. 24, 177-189.

[47] Badescu, V., 2002. A new kind of cloudy sky model to compute instantaneous values of diffuse and global solar irradiance. Theoretical and Applied Climatology. 72, 127-136.

[48] Ehnberg, J.S.G., Bollen, M.H.J., 2005. Simulation of global solar radiation based on cloud observations. Solar Energy. 78, 157-162.

[49] De Bary E., Muller F., 1963. The vertical distribution of clouds. Journal of Applied Meteorology. 2, 806.

[50] Kondratiev K.Y., Nicolsky G.A., Badinov I.Y., Andreev S.D., 1967. Direct solar radiation up to 30 km and stratification of attenuation components in the stratosphere. Applied Optics. 6, 197.

[51] Berk, A., Bernstein L.S., Robertson, D.C., 1989. MODTRAN: A moderate resolution model for LOWTRAN 7, Report GL-TR-89-0122, Geophysics Laboratory, Air Force Systems Command, United States Air Force, Hanscom, AFB, MA 01731

[52] Mayer B., Kylling A., 2005. Technical note: The libRadtran software package for radiative transfer calculations - description and examples of use. Atmos. Chem. Phys. 5, 1855-1877.

[53] Cloudnet, 2007. http://www.cloud-net.org/

[54] Donovan D., Van Lammeren A., 2001. Cloud effective particle size and water content profile retrievals using combined lidar and radar observations 1. Theory and examples. Journal of Geophysical Research. 106, 27425-27448.

[55] Jesch L.F., 1981. Solar Energy Today, International Solar Energy Society, UK Section.

[56] Brinkworth B.J., 1972. Solar Energy for man, Compton Press.

[57] Young, A.T., 1994. Air mass and refraction. Applied Optics. 33, 1108.

[58] Reda, I., Ashfin A., 2003. Solar Position Algorithm for Solar Radiation Applications. National Renewable Energy Laboratory.

[59] Hahn, C.J., Rossow W.B., Warren S.G., 2001. ISCCP Cloud Properties Associated with Standard Cloud Types Identified in Individual Surface Observations. Journal of Climate. 14, 11-28.

[60] Shettle, E.P., Fenn, R.W., 1979. Models for the aerosols of the lower atmosphere and the effects of humidity variations on their optical properties. Environmental Research Paper, Air Force Geophysics Lab., Hanscom AFB, MA. Optical Physics Div.

[61] Myers, D., Emery K., Gueymard C., 2004. Revising and validating Spectral Irradiance Reference Standards for PV Performance Evaluation. ASME Journal of Solar Energy Engineering. 126, 567-574.

[62] Aeronet, 2009. http://aeronet.gsfc.nasa.gov/

[63] Atmospheric Radiation Measurement Program, 1989. http://www.arm.gov/

[64] National Oceanic and Atmospheric Administration *(*NOAA), 2011. http://www.ozonelayer.noaa.gov/

[65] Jackson, B., 1996. A software power model for a spin-stabilized LEO spacecraft utilizing V/T charge control. Aerospace Applications Conference IEEE. 3. 219-227.

[66] Oke, T.R. 1992. Boundary Layer Climates. Second Edition. Routledge. New York.

[67] Ahrens, C. D. 2006. Meteorology Today. An Introduction to Weather, Climate, and the Environment. Eighth Edition. Thompson, Brooks/Cole. USA.

[68] U.S. Standard Atmosphere, 1976, U.S. Government Printing Office, Washington, D.C., 1976.

[69] Sutherland, W. (1893), "The viscosity of gases and molecular force", Philosophical Magazine, S. 5, 36, pp. 507-531 (1893).

[70] National Environment Research Council, 2011. http://www.nerc.ac.uk

[71] Seguro J. V., Lambert T. W., “Modern estimation of the parameters of the Weibull wind speed distribution for wind energy analysis”, Journal of Wind Engineering and Industrial Aerodynamics, Vol. 85, no. 1, 2000, pp. 75-84

[72] Askey, R. A.; Roy, R., “Gamma function”, Digital Library of Mathematical Functions, 2010, National Institute of Standards and Technology, from http://dlmf.nist.gov/

[73] Huschke, R. E., “Glossary of meteorology”, American Meteorological Society, Boston, 1959.

[74] “Airship Design Criteria”, FAA-P-8110-2 Change 2, Federal Aviation Administration, US Department of Transportation, 1986.

[75] U.S. Military Specification MIL-F-8785C, 5 November 1980.

[76] Nahon, M., Gilardi, G., Lambert, C., "Dynamics/control of a radio telescope receiver supported by a tethered aerostat", Journal of Guidance, Control and Dynamics, Vol. 25, No.6, 2002, pp. 1107-1115.

[77] Etkin, B., "Dynamics of Atmospheric Flight", 1972, Wiley, New York.

[78] Kang, W., Lee, I., "Analysis of tethered aerostat response under atmospheric turbulence considering nonlinear cable dynamics", Journal of Aircraft. Vol. 46, No.1, 2009, pp. 343-347.

[79] Civil Aviation Authority, 2008. http://www.caa.co.uk

[80] Robinson Douglas H., 1973. Giants in the Sky: A History of the Rigid Airship. University of Washington Press, ISBN-13: 978-0295952499.

[81] Harold G. Dick and Douglas H. Robinson, 1992. The Golden Age of the Great Passenger Airships: Graf Zeppelin and Hindenburg. Prentice Hall & IBD; ISBN-13: 978-1560982197.

[82] Capanina, 2000. http://www.capanina.org/

[83] Colozza A. and Dolce J.L., 2005. High-Altitude, Long-Endurance Airships for Coastal Surveillance. NASA Technical Report, NASA/TM-2005-213427.

[84] TCOM, 2009. http://www.tcomlp.com/aerostats.html

[85] Lockheed Martin, 2009. http://www.lockheedmartin.com/

[86] Roasaerosystems, 2009. http://rosaerosystems.pbo.ru/

[87] Badesha S.S., Euler A.J., Schroder L.D., 1996. Very high altitude tethered balloon parametric sensitivity study. Aerospace Sciences Meeting and Exhibit, 34th, Reno, NV, Jan. 15-18.

[88] Badesha S.S, 2002. SPARCL: A high-altitude tethered balloon-based optical space-to ground communication system. Proceedings of the SPIE - The International Society for Optical Engineering, 4821.

[89] Bely P. and Ashford R.L., 1995. High-altitude aerostats as astronomical platforms. Proceedings of SPIE - The International Society for Optical Engineering. 2478, 101-116.

[90] LOTTE, 2009. http://www.isd.uni-stuttgart.de/lotte/infodownload/engl_v02.pdf.

[91] Flying with Nephelios over the English Channel. Thomas Raphael.

[92] ESA Press Release, "Airships to complement scientific and Technological Satellite Systems", 17 March 2000.

[93] Gurfil P., and Cory J., 2007. A Lighter-than-Air System with an Embedded Photovoltaic Array for Electric Power Generation. Submitted to the 22nd European Photovoltaic and Solar Energy Conference, Milano, Italy.

[94] Cool Earth Solar, 2009. http://www.coolearthsolar.com/technology

[95] Leinonen A., 2008. Solarial, Mobile Power Generation for Disaster Relief. Industrial Design Thesis, Humber College.

[96] Wubbo J. Ockels, Laddermill, a novel concept to exploit the energy in the airspace, Aircraft Design, Volume 4, Issues 2-3, June-September 2001, Pages 81-97, ISSN 1369-8869, DOI: 10.1016/S1369-8869(01)00002-7.

[97] Power kites for wind energy generation: fast predictive control of tethered airfoils IEEE Control Systems Magazine, December 2007

[98] Roberts, B.W.; Shepard, D.H.; Caldeira, K.; Cannon, M.E.; Eccles, D.G.; Grenier, A.J.; Freidin, J.F.; , "Harnessing High-Altitude Wind Power," Energy Conversion, IEEE Transactions on , vol.22, no.1, pp.136-144, March 2007

[99] Kitegen, 2011. http://kitegen.com/

[100] Sky Windpower, 2011. http://www.skywindpower.com

[101] Selsam, Douglas Spriggs. Serpentine wind turbine. U.S. Patent 6616402, http://www.freepatentsonline.com/6616402.html

[102] Magenn, 2009. http://www.magenn.com/

[103] Altaeros, 2011. http://www.altaerosenergies.com/

[104] 21st Century Airship, 2009. http://www.21stcenturyairships.com/HighAlt

[105] Dorrington G:E:, 2005. Development of an airship for tropical rain forest canopy exploration. The Aeronautical Journal of the Royal Aeronautical Society.

[106] CargoLifter CL75 AirCrane, 2002. http://www.cargolifter.com

[107] Aerophile, 2008. http://www.aerophile.com/

[108] Miller J. and Nahon M., 2007. The Analysis and Design of Robust Helium Aerostats. AIAA Journal of Aircraft. 44, 1447-1458.

[109] Khoury G.A., Gillet J.D., 2004. Airship Technology. Cambridge Aerospace Series, Edited by Gabriel A. Khoury, J.David Gillett, ISBN-10: 0521607531.

[110] Lindstrand Technologies, 2009. http://www.lindstrandtech.com/

[111]T. Markvart, Solar Electricity (2nd edition), Wiley, Chichester, 2000.

[112] Green M.A., Emery K., Hishikawa Y., Warta W., 2008. Solar cell efficiency tables (Version 32). Progress in Photovoltaics: Research and Applications. 16, 435-440.

[113] M. Raja Reddy, Space solar cells--tradeoff analysis, Solar Energy Materials and Solar Cells, Volume 77, Issue 2, 15 May 2003, Pages 175-208

[114] Dhere N.G., Ghongadi S.R., Pandit M.B., Jahagirdar A.H., Scheiman D., 2002. CIGS2 thin film Solar cells on flexible foils for space power. Progress in Photovoltaics: Research and Applications. 10, 407-416.

[115] Paschen F., 1889. Ueber die zum Funkenübergang in Luft, Wasserstoff und Kohlensäure bei verschiedenen Drucken erforderliche Potentialdifferenz. Annalen der Physik. 273, 69-75.

[116] D.F. Warne, 2000. Newnes Electrical Engineer's Handbook, Newnes.

[117] ABB Resibloc, 2009. http://www.abb.com/

[118] Badesha S.S. and Bunn J.C., 2002. Dynamic simulation of high altitude tethered balloons systems subject to thunderstorm windfield. AIAA paper 2002-4614

[119] Aglietti, G.S., "Dynamic response of a high altitude tethered balloon system", Journal of Aircraft. Vol.46, No.6, 2009, pp. 2032-2040.

[120] Hoerner S.F., 1965. Fluid Dynamic Drag. Albuquerque.

[121] Solarbuzz, 2012. http://www.solarbuzz.com/

[122] Schlichting H., 1979. Boundary Layer Theory, 7th Edition, McGRaw-Hill, New York.

[123] Achenbach E., 1972. Experiments on the flow past spheres at very high Reynolds numbers. Journal of Fluid Mechanics. 54, 565.

[124] Maxworthy T., 1969. Experiments on the flow around a sphere at high Reynolds numbers. J. Appl. Mech. Trans. ASME. 36, 598.

[125] Williamson, C.H.K., Govardhan, R., "Vortex induced vibrations", Annual Review of Fluid Mechanics, Vol.36, 2004, pp. 413-455.

[126] Govardhan R., Williamson C. H. K., 1997. Vortex-induced motions of a tethered sphere. Journal of Wind Engineering and Industrial Aerodynamics. 69-71, 375-385.

[127] DeLaurier, J.D., "A stability analysis for tethered aerodynamically shaped balloons", Journal of Aircraft, Vol. 9, No. 9, 1972, pp. 646-651

[128] Jones, S.P., Krausman, J.A., "Nonlinear Dynamic Simulation of a Tethered Aerostat", Journal of Aircraft, Vol.19, No.8, 1982, pp.679-686

[129] Lambert, C., Nahon, M., "Stability Analysis of a Tethered Aerostat", Journal of Aircraft, Vol. 44, No.4, 2003, pp. 705-715.

[130] Coulombe-Pontbriand P., Nahon, M., "Experimental testing and modelling of a tethered spherical aerostat in an outdoor environment", Journal of wind engineering and industrial aerodynamics, Vol.97, No.5-6, 2009, pp. 208-218.

[131] Dorrington, G.E., "Use of helium-filled dirigibles for scientific exploration of rain forest canopy", 7th international airship convention, Friedrichshafen, 9-11 October 2008.

[132] Jauvtis N., Govardhan R., Williamson C. H. K., "Multiple Modes of Vortex Induced Vibration of a Sphere", Journal of Fluids and Structures, Vol.15, April 2001, pp.555-563.

[133] Naudascher E., Rockwell D., Flow Induced Vibrations: An Engineering Guide, 1993, Balkema.

[134] Victor W. Page, 1927. Modern Aircraft Basic Principles, Operation, Application.

[135] The Airship Association, 2011. http://www.airship-association.org

[136] Deutsches Bundesarchiv (German Federal Archive), Bild 102-05738.

[137] Young W.C., Budynas R.G., 2002. Roark's Formulas for Stress and Strain. Mc-Graw Hill International Education Series.

[138] Hexcel, 2011. http://www.hexcel.com.

[139] M. Raja Reddy, Space solar cells-tradeoff analysis, Solar Energy Materials and Solar Cells, Volume 77, Issue 2, 15 May 2003, Pages 175-208

[140] Aglietti, G.S., Wicks, A. and Barrington-Brown, A.J., 1999. SIL SGS-2.4 S-band ground station. Journal of Aerospace Engineering, 213, (4), 265-272.

[141] Leeson, 2011. http://www.leeson.com/

[142] SSD Drives, 2011. http://www.ssddrives.com/

[143] Data available at: http://adg.stanford.edu/aa241/structures/weightstatements.html

[144] University of Southampton, Solar Energy, 2011. http://www.soton.ac.uk/~solar/

[145] Wanggu Kang, Youngwook Suh, Kyeongsik Woo, In Lee, Mechanical property characterization of film-fabric laminate for stratospheric airship envelope, Composite Structures, Volume 75, Issues 1-4, Thirteenth International Conference on Composite Structures - ICCS/13, September 2006, Pages 151-155

[146] Keith McDaniels, RJ Downs, Heiner Meldner, Cameron Beach, Chris Adams, 2009. High Strength-to-Weight Ratio Non-Woven Technical Fabrics for Aerospace Applications. Cubic Tech Corp.

[147] Miller, Tim; Mandel, Mathias., 2002. Airship Envelopes: Requirements, Materials and Test Methods. Dover: ILCDover